Preparation and analysis of transition metal-doped In$_2$S$_3$ for intermediate band solar cell application

Dissertation

zur Erlangung des Doktorgrades der Naturwissenschaften
(Dr. rer. nat.)

der

Naturwissenschaftlichen Fakultät II
Chemie, Physik und Mathematik

der Martin-Luther-Universität
Halle-Wittenberg

vorgelegt

von Herrn Leonard Alwin Markus Wägele
geb. am 01.06.1988 in Oldenburg

GutachterInnen:

Prof. Dr. Roland Scheer

Prof. Dr. Kathrin Dörr

Prof. Dr. Peter Wellmann

Verteidigt am:

15.11.2022

Angaben zur Person und zum Bildungsweg

Angaben zur Person
Name: Leonard Wägele

Bildungsweg

Nov. 2014 - Nov. 2022   **Promotionsstudium Physik**
Martin-Luther-Universität Halle-Wittenberg
Thema: *Preparation and analysis of transition metal-doped In_2S_3*
for intermediate band solar cell application

Okt. 2012 - Okt. 2014   **Masterstudium Physik**
Martin-Luther-Universität Halle-Wittenberg
Abschluss: Master of Science (M. Sc.)
Thema: *Real-time analysis of thin film chalcogenide growth*
for photovoltaics using in-situ X-ray diffraction

Okt. 2008 - Okt. 2012   **Bachelorsstudium Physik**
Rheinische Friedrich-Wilhelms-Universität Bonn
Abschluss: Bachelor of Science (B. Sc.)
Thema: *Crosstalk studies of unirradiated diamond, planar- and*
3D-silicon pixel detectors with the ATLAS FE-I4 pixel readout chip

Jun. 2007   **Allgemeine Hochschulreife**
Konrad-Adenauer-Gymnasium Bonn

Publikationen

- Ghorbani, E., Schiller M., Falk, H. H., Wägele, L. A., Eckner, S., d'Acapito, F., Scheer, R., Albe, K. and Schnohr, C. S. (n.d.), *Elucidating the local structure of V substitutes in In_2S_3 as potential intermediate band material by X-ray absorption spectroscopy and first principles calculations.* Submitted.

- Stange, H., Brunken, S., Greiner, D., Heinemann, M. D., Yani, D. A. B., Wägele, L. A., Li, C., Sanli, E. S., Kahnt, M., Schmidt, S. S., Bäcker, J.-P., Kaufmann, C. A., Klaus, M., Scheer, R., Genzel, C. and Mainz R. (2019), *Stacking fault reduction during annealing in Cu-poor $CuInSe_2$ thin film solar cell absorbers analyzed by in situ XRD and grain growth modeling.* Journal of Applied Physics 125, 035303.
  DOI: 10.1063/1.5052245

- Jawinski, T., Wägele, L. A., Scheer, R., Grundmann, M. and von Wenckstern, H. (2018), *Properties of In_2S_3-Based pin-Heterojunctions.* Phys. Status Solidi A, 215: 1700827.
  DOI: 10.1002/pssa.201700827

- Wägele, L. A., Rata, D., Gurieva, G. and Scheer, R. (2017), *Structural analysis of co-evaporated In_2S_3 and In_2S_3:V for solar cell absorber applications.* Phys. Status Solidi C, 14: 1600204.
  DOI: 10.1002/pssc.201600204

- Zahedi-Azad, S., Jarzembowski, E., Hartnauer, S., Wägele, L., Greiner, D. and Scheer, R. (2016), *Monitoring the phase evolution of $Cu(In,Ga)Se_2$ by different Se flux via in-situ XRD.* Phys. Status Solidi A, 213: 2169-2175.
  DOI: 10.1002/pssa.201532991

- Pistor, P., Zahedi-Azad, S., Hartnauer, S., Wägele, L. A., Jarzembowski, E. and Scheer, R. (2015), *Real time observation of phase formations by XRD during Ga-rich or In-rich $Cu(In, Ga)Se_2$ growth by co-evaporation.* Phys. Status Solidi A, 212: 1897-1904.
  DOI: 10.1002/pssa.201431949

- Hartnauer, S., Wägele, L. A., Jarzembowski, E., Scheer, R. (2015), *In-situ XRD study of alloyed $Cu_2ZnSnSe_4$–$CuInSe_2$ thin films for solar cells.* Thin Solid Films, Volume 582, Pages 272-275, ISSN 0040-6090.
DOI: 10.1016/j.tsf.2014.11.061

- Hartnauer, S., Wägele, L. A., Syrowatka, F., Kaune, G. and Scheer, R. (2015), *Co-evaporation process study of $Cu_2ZnSnSe_4$ thin films by in situ light scattering and in situ X-ray diffraction.* Phys. Status Solidi A, 212: 356-363.
DOI: 10.1002/pssa.201431497

- Bauer, J., Wägele, L. A., Gase K., and Breitenstein, O. (2014), *Pseudo Shunts Interfering Lock-In Thermography Investigations of Solar Cells: Characterization and Prevention.* IEEE Journal of Photovoltaics, vol. 4, no. 6, pp. 1429-1432.
DOI: 10.1109/JPHOTOV.2014.2347800

Contents

Chapter 1

Introduction

1.1 Motivation

The human-induced climate change is one of the largest catastrophes that mankind will have to deal with in the foreseeable future. One of the key solutions to change the human impact on the global climate is the switch to renewable energy sources and the reduction of the overall energy consumption. One of the cheapest energy sources today is the sun, as it is available everywhere on the planet and can be harvested with relatively low-tech solutions. Despite the success of existing photovoltaic technologies, the need for high efficient solar cells rises to satisfy the ever-growing need for energy. Especially in densely populated areas the space for energy sources is limited so that solar cells with higher efficiencies can become more cost-effective.

The efficiency of the standard first generation solar cell, like the single- or polycrystalline silicon solar cells, is limited by the band gap of the used material. All photons with energies below the band gap of the absorber material cannot be converted to electrical energy, while photons with energies above the band gap can be converted only partially into electrical energy. The Shockley–Queisser limit (Shockley and Queisser 1961) gives us the theoretical maximum energy conversion efficiency such a photovoltaic device can have: $33.7\,\%$ under sunlight spectrum on the surface of the earth (AM 1.5) (Rühle 2016). While there are different ways to overcome this limit by e.g. light concentration, multiple p-n-junctions or photon upconversion, we will focus on the technology used in this thesis: The intermediate band solar cell (IBSC).

1

1.2   Intermediate band solar cell

As the name suggests, this photovoltaic technology utilizes additional energy bands inside the band gap of the absorbing semiconductor to effectively absorb photons of multiple energies. The basic concept uses one band inside the band gap, the intermediate band (IB), which allows the device to absorb three different photon energies without loosing their energy during the conversion. There are currently four known ways to implement such an intermediate band (Okada et al. 2015; Ramiro et al. 2020): Through quantum dots (A. Luque et al. 2004; Marti et al. 2000), highly mismatched alloys (Lin et al. 2009; Yu et al. 2003), organic molecules (Ekins-Daukes et al. 2008; Simpson et al. 2015) or deep level impurity bands.

The latter approach uses a host semiconductor with a high energy band gap which is hyperdoped with impurities that create deep-level energy states within the band gap. The density of these impurities have to exceed the necessary threshold for a Mott transition to occur, overlapping the single impurity energy states into a material spanning energy band. The necessary impurity concentration depends on the host material, as well as the hyperdoped impurity element. (Antonio Luque et al. 2001; Marsen et al. 2012)

At the current state of research none of these four techniques have resulted in solar cells with any efficiency gain over the respective single-junction devices and their potential is far from been reached (Ramiro et al. 2020).

1.3 In_2S_3:TM as an IB material

In this work we grow In_2S_3:TM (TM = V, Ti, Nb) impurity-band absorbers, study the structural and optoelectronic effects of hyperdoping on the host material as well as show the existence and basic properties of the intermediate band. The chosen host material is indium sulfide (In_2S_3) which was suggested by Palacios et al. (2008). In_2S_3 is known to have a band gap around $2\,eV$ (Barreau, Mokrani, et al. 2009; Ghorbani and Albe 2018) and is widely researched as a less-toxic alternative for the buffer layer in second generation thin-film photovoltaic devices (Abou-Ras et al. 2005; Naghavi et al. 2010). We incorporate the transition metals (TMs) vanadium (V), titanium (Ti) and niobium (Nb) as impurities, as they have already shown promise for the formation of

intermediate bands in In_2S_3 (Ho 2011; Lucena, Conesa, et al. 2014; McCarthy, Weimer, Haasch, et al. 2016; Tapia et al. 2016). The literature review in section 2.4.2 illustrates that the existence of an intermediate band in transition metal-doped In_2S_3, or at least energy states inside the band gap, is not only predicted, but also confirmed. But there are missing key pieces to fully understand the origin of the measured doping-induced inter-band states. The β-In_2S_3 structure is very complex which makes it a difficult candidate for theoretical calculations. None of the publications show a complete picture of the effects of hyperdoping on In_2S_3; especially the structural changes are neglected. Despite the low predicted maximum effeciency for In_2S_3:V of $20.8\,\%$ (Strandberg and Aguilera 2012), In_2S_3:TM (M=V, Ti, Nb) with its high band gap and multiple possible impurities is a good material to research impurity band solar cells in general.

1.4 Goals

This thesis aims to use physical vapor deposition (PVD) from the elements to grow high quality polycrystalline thin-film In_2S_3 and hyperdope it with vanadium, titanium and niobium. The systematic research of the effects of hyperdoping on the host In_2S_3 lattice are the main focus of the material analysis.

At the end of this work, an effective PVD process should be found that can reliably produce In_2S_3:TM thin film absorbers. The structural changes of the host material from hyperdoping and the positioning of the transition metal atoms within the host In_2S_3 material should be better understood. Last but not least, the intermediate states created by hyperdoping should be detected and compared to the other preparation methods published until now.

Chapter 2

Fundamentals

2.1 Crystals

2.1.1 Crystal growth

A material can be called a crystal, if its atoms exhibit a long range order in all three dimensions. Certain conditions apply for atoms to arrange themselves into crystals which vary strongly between materials. For semiconductors crystal growth is often done from a melt or gas of single elements or molecules needed to form the material. If the crystal is grown from gas, a substrate is used as a basis for the crystal to grow on. For semiconductor devices the substrate is mostly chosen for its electrical or optical properties, but can also be used to change the structure of the crystals growing on top. In the following we will only look at the crystal formation from evaporated material on a substrate.

Crystal growth always starts with nucleation, which describes the time for the first crystal to grow. A nucleus is the initial crystal seed that determines the structure and orientation of the crystal. After its formation, the incoming atoms or molecules can either grow the existing nuclei, or form new nuclei. The substrate temperature determines the mobility of the adsorbed molecules, while the gas saturation above the substrate determines the amount of available molecules and the pressure they exert on the surface. These two parameters determine the crystal growth rate and the balance between growing existing crystals and forming new nuclei. At low temperatures the mobility of the molecules is low, more nuclei form and the crystal growth

5

rate is low. If the temperature is too high, the molecules start to desorb before they can be incorporated into a crystal. If the temperature is in the right range only the molecule transportation limits the crystal growth. The vapor pressure or saturation above the substrate also dictates the growth rate, as it determines the amount of available molecules. But a too high saturation causes the molecules to form new nuclei with each other before they can settle on existing crystals, decreasing the crystal size.

The structure that crystals form is also determined by the temperature. A higher temperature increases the thermal energy and therefore vibrations of the atoms, which can cause the ordering to change. The higher thermal energy forces the atoms to rearrange into a different structure, with a higher symmetry. The different crystal structures a material can form are called crystal phases. The stoichiometry, or proportions between the elements, can also determine the phase of a crystal. It is important in which phase a crystal is, as the structural differences can have a large impact on the optical and electrical properties of the material. (Kittel 2006)

2.1.2 Crystal types

The unit cell of a crystal lattice describes (most of the time) the smallest possible part a lattice that can be used to recreate the complete crystal by translation. The unit cell is defined by the three lattice vectors that span the unit cell in three dimensions. There are 14 different base lattices, called Bravais lattices, which can be used to describe any crystal. On these lattices the atoms are placed to construct the real crystal. Two of the Bravais lattices are needed for this thesis: The face centered cubic lattice, where all sides and angles are the same, with additional lattice bases on the faces of the cube, and the body centered tetragonal lattice, where the lattice is elongated along one axis with an additional lattice base in the center of the lattice.

One of the main techniques to get information about crystal structures is through scattering. The long range order of the crystals is utilized by scattering e.g. photons off the lattice planes. Interference between the scattered photons results in detectable patterns, that contain information about the structure of the crystals. Since it is an indirect measurement of the lattice, this pattern is not part of the real space, but of the so called the reciprocal space. The reciprocal lattice is the Fourier transform of the real or direct lattice. All parallel planes in the direct lattice result in one point or reflex

in the reciprocal lattice. The position and shape of these reflexes contain information about the lattice structure, but also about preferred growth directions (texture), strain on the crystals, microstrain within the crystals and the crystal size.

The Miller indices (h, k and l) are a way to easily distinguish lattice planes. They are very useful as they define a point in reciprocal space (the measurable reflex), but also have meaning in real space: They define the intercepts of the lattice plane with the lattice vectors of the unit cell. Given the lattice vectors of a crystal the Miller indices hkl can be used to calculate the distance between the parallel planes defined by the Miller indices. On the other hand, measuring the lattice plane distance via the interference pattern following Bragg's law, it is possible to calculate the lattice vectors, if the Miller indices are known. As already stated above there are only a limited number of basic lattice types which allows the simplification of the lattice vectors. Instead, only lattice parameters (lattice constants) together with angles between the vectors are used. For example in a cubic lattice the angles between the lattice vectors are all 90° and their length is the same for all three directions, so only one lattice parameter is needed to describe the crystal's complete unit cell. (Kittel 2006)

2.1.3 Secondary phases

During the growth of crystals with two or more elements it is possible that the incoming molecules form different stoichiometries than the main material. These are called secondary phases and can form, if for example the proportions between the supplied elements are incorrect or the secondary phase is energetically favorable.

2.2 Semiconductor physics

2.2.1 Energy bands

A crystal contains electronic energy bands that consist of many energy levels spanning the whole crystal. Electrons stay on these energy levels, but are relatively free to move as long as there are free positions. A band can either be filled, partially filled or empty, depending on the number of electrons that fill the energy levels. Because the energy levels in a band are so close together, electrons can easily switch energy levels within

a band and move around in a way, which would be impossible in separated atom. The bands form due to the long range order of the atoms in a crystal. The electron wave functions of the atoms overlap with each other which creates delocalized energy bands that electrons (previously localized around one atom) can use to move through the whole material. Atoms have multiple electron shells that provide a fixed amount of electrons per atom and overlap to form multiple energy bands. The electrons that were previously localized around one atom now fill the bands from low (nearest to atom) to high (farthest from atom) energy. (Kittel 2006)

2.2.2 Electron transition types

The energy position of energy states in a semiconductor is dependent on the crystal momentum k of the electrons. This dependency is described by the dispersion relation $E(k)$ which can have multiple extrema. The conduction band and valence band follow different $E(k)$ which can place the conduction band minimum (CBM) at a different k vector than the valence band maximum (VBM). The Fermi-Dirac distribution for the electron position determined by the thermal energy of the system states that lower energy positions are more likely to be occupied by electrons. As such, most electrons will be found at the CBM, and most holes (missing electrons) at the VBM.
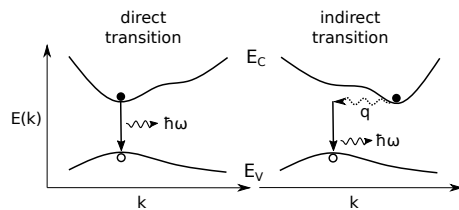
Figure 2.1: *Schematic diagram of direct and indirect radiative transitions in the dispersion relation $E(k)$ resulting in a photon with energy $\hbar\omega$. The indirect transition needs a phonon q for momentum conservation.*

If the CBM and VBM are at the same k vector, the electrons can directly switch between the two by absorbing or emitting photons. This is then called a direct semiconductor that allows for direct electron transitions. If the CBM and VBM are at different momenta, the electrons cannot directly switch between the bands due to the required momentum conservation. In this case the electrons need additional phonons (lattice vibrations) with the right momentum for them to be able to transition to the other band. Depending on the temperature, this process is much less likely than a direct transition and reduces the absorption in the energy range of the indirect transition. Figure 2.1 shows

differences between the direct and indirect radiative transitions.

Defects can add additional transitions that are explained in the next section. (Kittel 2006)

2.2.3   Defects and recombination

A real crystal often has disturbances to the long range order called defect. There are different defects that can influence a material in different ways. Point defects like impurities, vacancies or an element at the wrong position (interstitial or antisite defects) have an effect on the electrical and optical properties of a material. Every element brings about different electron energy states and number of electrons, that affect the available energy positions and occupations. Isolated point defects are often localized. The electrons then cannot move freely away from the defect, without either giving up energy or gaining energy. A high enough defect density of e.g. an introduced impurity that acts as a shallow (near a band) defect can increase the amount of electrons or holes available for conduction (called doping). Deep defects on the other hand form energy states in between the valence and conduction band that can act as electron traps that hinder conduction and induce non-radiative recombination. In equilibrium, the energy position of electrons is given by the above-mentioned Fermi-Dirac probability distribution determined by the thermal energy of the system. When an electron in the conduction band finds a suitable hole in the lower energetic valence band with the same momentum it will, dependent on the temperature, most likely fill the hole (recombine). The energy conservation requires that the excess energy is either released as a photon (radiative recombination) or given to another electron (Auger recombination). Another recombination path opens, if deep defects are available in the band gap. Electrons can use these defects to recombine non-radiatively by emitting phonons instead of photons. As found by Hall (1951) and Shockley and Read (1952) this works because localized deep defects have different dispersion relations than the bands. Electrons can therefore switch to these defects while still conserving the momentum. Additional occupation dependency of the defects' dispersion relation and energy position allow the recombination via the defects. Especially in indirect semiconductors this is much more probable than the radiative recombination where the momentum conservation is difficult to satisfy. If the defect density increases, the non-radiative recombination

increases, reducing the life-time of free charge carriers. A high life-time is crucial for the separation of charge carriers and therefore generation of a current in a solar cell. (Kittel 2006)

2.3 Deep-level impurity band

An intermediate band has to have certain properties to maximize the efficiency increase of the IBSC (Antonio Luque et al. 1997; Martí et al. 2013).

Its energy position should be near one third of the band gap. From theoretical calculations it follows that under black-body radiation the efficiency is at a maximum for the energy positions shown in table 2.1. These values are slightly different under AM 1.5 spectrum, but the general trend of splitting the band gap E_G with the IB into roughly $E_L \approx 0.4 \cdot E_G$ and $E_H \approx 0.6 \cdot E_G$ is the same (Bremner et al. 2008).

Table 2.1: *Calculated optimal highest IB to CB or VB distance E_H, band gap E_G for unconcentrated and maximally concentrated black-body radiation (Ramiro et al. 2020).*

Concentration	E_H	E_G
no	1.53 eV	2.40 eV
yes	1.27 eV	1.96 eV

The absorption coefficients for the three possible transitions E_G, E_L and E_H should not overlap. If they do, some photons can use multiple absorption channels, exciting electrons e.g. far above the conduction band minimum and thereby causing thermalization losses. (Martí et al. 2013) The IB should be half filled, so that transitions into and out of the IB are equally possible. Photofilling an empty IB might be possible with concentrated light in some cases, but it will probably be less efficient, as the photofilled electrons can drain out of the IB via non-radiative recombination. (Strandberg and Reenaas 2009) The IB transitions should also have similar absorption cross-sections. Otherwise, the IB will be filled or emptied over time, limiting the effectiveness of the excitation from the VB into the CB.

Figure 2.2 displays the band diagram of an IB absorber. In our case the IB is introduced by hyperdoping the host material with impurities. The formation of energy bands from localized defect states has been first described by Anderson (1958) and
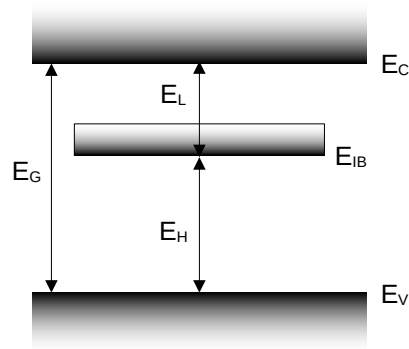
Figure 2.2: *Band diagram of an IB absorber material. Three transitions are possible for the electrons: VB-CB, VB-IB and IB-CB.*

Mott (1949, 1968) on dopants. By increasing the impurity density and placing them in an ordered host lattice, the electrons and the defects' energy states start to interact with one another. At a certain impurity density the wavefuntions of the electrons start to overlap, similar as in the formation of the bands in a semiconductor. The dopants form a super lattice within the host lattice with its own delocalized energy bands, allowing for electrons to move freely. This Metal-Insulator transition is also called a Mott transition. Ghorbani, Barragan-Yani, et al. (2020) calculated the needed impurity concentrations for the delocalization of the defects for In_2S_3:Ti and In_2S_3:Nb to $\geq 5\,\text{at.\%}$ and $\geq 2.5\,\text{at.\%}$, respectively. Therefore, two factors have to be considered: The ordering of the impurities and the impurity concentration. Since localized deep defects can drastically reduce the efficiency of an absorber, the delocalization via the Mott transition and the resulting recovery of the free charge carrier lifetimes is crucial in a deep-level impurity band material.

2.4   Indium sulfide

2.4.1   Indium sulfide properties

Structural properties

The structure of In_2S_3 is based on a cubic spinel. It contains an anion (X) face centered cubic (fcc) lattice, with usually two elements of different valence as the cations (A, B)

with the form AB_2X_4. While divalent ions (A) are situated on tetrahedral positions (Th), the octahedral positions (Oh) are filled with the trivalent (B) atoms. Indium is a trivalent element so that common spinels are MIn_2S_4 with M being a divalent element like Mn, Co or Mg. In the In_2S_3 structure no divalent atoms are available, so the indium atoms have to fit in the sulfur tetrahedra that only need two electrons of the three available. As a result, two indium atoms have enough electrons for three tetrahedral positions, creating an intrinsic indium vacancy v_{In} (vacancies are denoted with a 'v' to distinguish them from vanadium 'V'). Using a $\square$ to symbolize the empty position the formula of this structure can be written as $[In_{2/3}\square_{1/3}]^{Th}[In]_2^{Oh}S_4$, which falls back to In_2S_3. Because of the intrinsic defects, this crystal structure is also called a defect spinel. The vacancies in the In_2S_3 structure can be ordered or disordered, depending on the available sulfur and the temperature of the material. At room temperature the defect spinel In_2S_3 is completely ordered in a tetragonal super-structure with the v_{In} on a spiral along the structure's c-axis. This structure variant is called the β-phase of the material or simply β-In_2S_3. It has the space group I41/amd (141) with lattice constants of $a = 7.6231\,\text{Å}$ and $c = 32.358\,\text{Å}$ (Pistor et al. 2016). For higher temperatures of above $\sim 440\,°\text{C}$ (Pistor et al. 2016), or lower sulfur content of below 59.5 to $59.0\,\text{at.\%}$ (Goedecke et al. 1985), the indium atoms start to move to random positions on the tetrahedral sites. This disordering destroys the tetragonal super-structure, leaving a cubic defect spinel. This is the so called α-phase or α-In_2S_3. It has the space group Fd-3m (227) with a lattice constant of $a = 10.8315\,\text{Å}$ at $475\,°\text{C}$ (Pistor et al. 2016). Because of the similarity between the α- and β-phase, it is difficult to distinguish them. This fact is very often overlooked in the literature, be it regarding XRD or Raman measurements. For even higher temperatures of above $\sim$810 °C the In atoms are only present on octahedral sites, changing the complete structure into a hexagonal one. This is the γ-phase or γ-In_2S_3 that is not stable at room temperature. It crystallizes in the P-3m1 (164) space group with lattice constants of $a = 3.8656\,\text{Å}$ and $c = 9.1569\,\text{Å}$ at $825\,°\text{C}$. (Pistor et al. 2016) X-ray diffraction at lower temperatures ($80\,\text{K}$) conducted by Wyżga et al. (2020) did not reveal new phase transitions, but the effect of overlap or twinning of XRD reflexes was reduced. In this paper they also show more accurate phase transtion measurements and determined that the β-α transition is a 1st order transition occuring at about $700\,\text{K}$ ($427\,°\text{C}$).

Intrinsic defects

Rehwald et al. (1965) did a thorough analysis of the electrical properties of In_2S_3 grown with chemical transport reaction with varying sulfur concentrations. They conclude from resistivity, Hall, thermoelectric power and optical absorption measurements that In_i and In_{v_S} act as donors and v_{In} as a compensating acceptors. Pai et al. (2005) used spray pyrolysis to prepare In_2S_3 that contained chlorine and had oxygen on the surface. They estimated their band gap to be about $2.6\,eV$ and varied the stoichiometry of the material. Using thermally stimulated current measurements they found the activation energies of four defects and assigned likely defects depending on the stoichiometry: v_{In} (S-rich $0.1\,eV$), chlorine ($0.26\,eV$), v_S (In-rich $0.43\,eV$) and O_S (O-rich $0.82\,eV$). Jayakrishnan et al. (2005) prepared oxygen-contaning In_2S_3 via chemical spray pyrolysis with a high band gap of $2.76\,eV$. They noticed two visible photoluminescence bands occuring for differently prepared samples. For the In-rich sample they found a transition at $1.88\,eV$ assumed to be a transition from In_i to O_{v_S}. For the S-rich sample they found a transition at $2.19\,eV$ assumed to be a transition from v_S to v_{In}. Ho (2011, 2012) used chemical vapor transport to grow In_2S_3 single crystals with a band gap of $2.075\,eV$. One shallow defect at about $1.906\,eV$ assigned to v_S and two deep intrinsic defect transitions were found at $1.518\,eV$ and $1.572\,eV$ and assigned to v_S and $v_{S'}$ to v_{In} transitions. Extensive theoretical calculations using hybrid-functional DFT were done by Ghorbani and Albe (2018). The main results are that under In-rich conditions donor type defects, mainly In_i ($1.72\,eV$ above the VBM) and if the Fermi level is close to the CBM v_S ($1.58\,eV$), $v_{S'}$ ($1.86\,eV$, $2.07\,eV$), $v_{S''}$ ($1.27\,eV$) and In_S ($2.02\,eV$) can form. In the S-rich case, the acceptor-like deep defects v_{In} ($0.64\,eV$) and S_{In} ($1.23\,eV$) are most likely to occur.

Optical properties

Barreau (2009) have published a review of In_2S_3 films in the photovoltaic field and show that the reported band gap varies greatly with different growth techniques. CBD grown samples can reach up to $3.7\,eV$, while PVD grown samples have the lowest band gaps at around 2.0 to $2.3\,eV$. The main reasons are the strong dependence of the band gap from the In_2S_3 stoichiometry and impurities, which are incorporated during growth. Barreau, Bernède, Deudon, et al. (2002) and Barreau, Bernède, and Marsillac

(2002) grew pure and Na-doped thin In_2S_3 films by annealing stacked indium, sulfur and sodium layers. They find a direct allowed band gap of $2.1\,eV$ for pure In_2S_3, which increases to $2.95\,eV$ with a sodium concentration of above $6\,at.\%$. Barreau, Marsillac, Bernède, Ben Nasrallah, et al. (2001) also investigated the incorporation of 5 to $10\,\%$ oxygen into In_2S_3 and noticed a strong increase of the band gap to $2.8\,eV$. In a newer publication Barreau, Mokrani, et al. (2009) grew pure In_2S_3 $500\,nm$ thin films via co-evaporation, which is closest to our growth method. Their films show an indirect transition at $2.01\,eV$. A very detailed theoretical look on the band structure and absorption of β-In_2S_3 was done by Zhao et al. (2013) using DFT. They found that the $1.977\,eV$ band gap is indirect in nature. The conduction band minimum (CBM) is located at the Γ-point, while the valence band maximum (VBM) is at the N-point. The energy difference of the VBM to the direct transition at the Γ-point is only $0.089\,eV$, which leads to the first direct transition to occur at $2.066\,eV$ and makes it difficult to separate the indirect and direct transitions. Because of the tetragonal structure of β-In_2S_3, the absorption is anisotropic. While the a and b axes have the same absorption, the c axis has a different absorption spectrum. It is calculated, that the a/b axis absorption has maxima at $2.2\,eV$, $3.0\,eV$ and the c-axis has a peak at $2.8\,eV$. Ghorbani and Albe (2018) used a hybrid functional DFT approach which is expected to result accurate band energies. They find a $2.11\,eV$ band gap.

Electrical properties

In_2S_3 is an intrinsically n-doped semiconductor which properties strongly depend on the preparation process. Especially the presence of impurities (Barreau, Bernède, and Marsillac 2002; Mathew et al. 2006) and excess of In or S during the process (Ghorbani and Albe 2018; Jayakrishnan et al. 2005; Rehwald et al. 1965) change the presence of defects and therefore also electrical properties. Rehwald et al. (1965) already systematically measured the strong dependency of the conductivity on the sulfur content of In_2S_3 grown via chemical transition reaction. Resistivities between 0.13 and $2000\,\Omega\,cm^{-1}$ and free charge carrier densities between $1\times10^{18}\,cm^{-3}$ and $2.4\times10^{13}\,cm^{-3}$ were measured. They attributed this to the In_i and In_{v_S} acting as donors and v_{In} as a compensating acceptors. In stoichiometric samples the In_i and v_{In} might compensate each other, leading to low free charge carriers densities. Later works have even reached

resistivities as high as $1 \times 10^{-7}\,\Omega\,\mathrm{cm}^{-1}$ (Asikainen et al. 1994). Barreau, Bernède, and Marsillac (2002) noticed an increased conductivity by doping In_2S_3 with Na, Mathew et al. (2006) by doping with Ag. Ho (2012) showed that doping In_2S_3 with $0.2\,\mathrm{at.\%}$ Nb increases the resistivity from about 1×10^5 to $1 \times 10^7\,\Omega\,\mathrm{cm}^{-1}$. He attributed this to the introduced deep defects that trap free charge carriers.

2.4.2 Intermediate band indium sulfide

The use of In_2S_3 for IBSCs was originally proposed by Palacios et al. (2008) backed by density-functional calculations. These first calculations were conducted on $MgIn_2S_4$, as the β-In_2S_3-phase has a very large unit cell and is difficult to calculate. For vanadium-doped In_2S_3 (In_2S_3:V) they predicted the VB-IB transition to start at about $0.7\,\mathrm{eV}$. The first realization was done by Lucena, Aguilera, et al. (2008) and Lucena, Conesa, et al. (2014) with polycrystalline powder grown via solvothermal reactions. They hyperdoped with roughly $3.4\,\mathrm{at.\%}$ V. They found additional sub-bandgap transitions in absorption measurements indicating intermediate states at about $1.65\,\mathrm{eV}$ above the VB. Ho (2011) published results on In_2S_3:Nb prepared with chemical vapor transport and up to $0.2\,\mathrm{at.\%}$ Nb with intermediate states found in temperature-dependent thermoreflectance measurements at about $1.52\,\mathrm{eV}$ above the VB. Strandberg and Aguilera (2012) have calculated the maximum efficiency that is to be expected for an In_2S_3:V IBSC in 2012 and also given the optimal thickness of the absorber layer. For a hyperdoping concentration of $5\,\mathrm{at.\%}$ with an illumination of 1 sun they calculated a maximum efficiency of $20.8\,\%$ for a layer thickness of $1\,\mathrm{\mu m}$. This efficiency is lower than the detailed balance limit for a single band gap solar cell with the same bad gap. Chen et al. (2013) grew iron doped In_2S_3 samples via solid state reactions. The band gap of the pure In_2S_3 powder was at $1.85\,\mathrm{eV}$. When incorporated with iron, a clear increase of the absorption below the band gap was detected. The absorption showed a distinct second maximum at around $1\,\mathrm{eV}$. McCarthy, Weimer, Haasch, et al. (2016) have worked on thin film In_2S_3:V deposited by atomic layer deposition with up to $9\,\mathrm{at.\%}$ V and showed their results in 2016. Their absorption measurements displayed only one additional transition at $\sim 0.8\,\mathrm{eV}$ above the VB, indicating a mostly filled IB. Tapia et al. (2016) showed extensive analysis of In_2S_3:V thin films on fluorine-doped tin oxide with up to $3.4\,\%$ V content prepared using ion layer gas reaction (Spray ILGAR).

They notice a decrease of the carrier lifetimes and diffusion lengths when doping with V which they attribute to in-gap V states increasing the non-radiative recombination and trapping of free charge carriers. Together with the workgroup of Marius Grundmann at the university of Leipzig we presented a pin-diode solar cell concept based on our In_2S_3:V samples. The back contact is ZnO:Al and two p-TCOs were tested as window layers: $ZnCo_2O_4$ and NiO. Of the two, $ZnCo_2O_4$ showed better rectification. Under illumination the solar cells displayed an open-circuit voltage of up to $300\,mV$ and a short-circuit current density of up to $0.29\,mA\,cm^{-2}$. While even the V-doped samples showed photovoltaic behavior, more optimizations have to be done to get any decent efficiency. (Jawinski et al. 2018) The newest theoretical calculations on β-In_2S_3 were conducted by Ghorbani et al. regarding intrinsic defects as well as incorporation of V, Ti and Nb impurities in octahedral positions using hybrid density functional calculations. The latter calculations were inspired by private communications about our experimental work on these three materials. For vanadium they found that the neutral V^0 on the octahedral positions do not form an IB at all. V^{-1} can form occupied states in n-doped In_2S_3 at $1.83\,eV$ above the VB. The results also indicate that there are minimal impurity concentrations needed for IBs to form: $\geq 5\,at.\%$ for Ti and $\geq 2.5\,at.\%$ for Nb. For In_2S_3:Ti the incorporation into one of the octahedral positions (In^{16h}) can form occupied states at $0.14\,eV$ above the VB. For In_2S_3:Nb both octahedral positions result in occupied intermediate states $0.45\,eV$ and $0.62\,eV$ above the VB. By hyperdoping α-In_2S_3 with $1.9\,at.\%$ octahedral V, an empty IB at about $1.82\,eV$ can be expected. At higher concentrations and V in tetrahedral coordination the band gap of α-In_2S_3 is reduced instead. (Ghorbani and Albe 2018; Ghorbani, Barragan-Yani, et al. 2020; Ghorbani, Erhart, et al. 2019; Ghorbani, Schiller, et al. n.d.)

Chapter 3

Preparation of transition metal-doped In$_2$S$_3$

Physical vapor deposition is one of the best ways to grow thin and pure semiconductor films (Barreau 2009). This chapter describes how we use this method to grow In$_2$S$_3$:TM thin films.

3.1 Physical vapor deposition

In physical vapor deposition (PVD) the elements needed for the film are evaporated or sputtered onto a heated substrate inside a vacuum. This allows fine control over the composition and growth conditions of the resulting layers. Since the growth happens in a vacuum only with the needed elements very pure layers of the wanted material can be grown. Co-evaporation from the elements is a special case where all required elements are evaporated from separated sources at the same time, with the reaction to the desired material happening during growth at the substrate. The stoichiometry and crystallite sizes of the final film are determined by the provided vapor pressure of each element and the temperature at the substrate (see section 2.1.1).

3.2 Sample preparation

All samples are grown in a custom co-evaporation chamber which has been built for
the growth of In_2S_3:TM (see figure 3.1). The high vacuum is achieved with a turbo-
molecular pump *STP-301C* from *Edwards* combined with a pre-pump e.g. a *XDS5* from
Edwards. A *Edwards WRG-S* gauge is used to measure the pressure which is around
$6 \cdot 10^{-6}$ mbar after pumping overnight and $6 \cdot 10^{-5}$ mbar during a process.
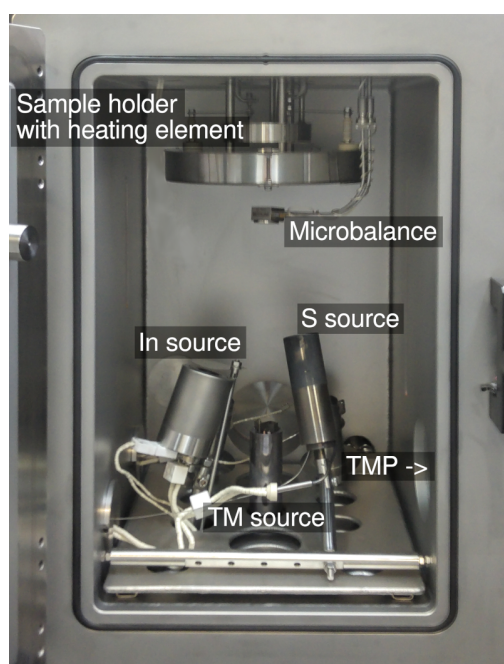

Figure 3.1: *Evaporation chamber for*
In_2S_3:TM preparation.

The chamber was originally designed
to be used in an in-situ X-ray diffraction
setup, where the X-rays enter and exit
through Kapton-covered slits in the side
of the chamber. Since in-situ XRD was
not used for the samples shown here, two
stainless steel covers replace the Kapton
to reach a better vacuum. To enable in-
situ XRD experiments the sample holder
is attached to the translator *HLSM100-25-
SS* from *UHV Design* for height calibra-
tion of the XRD geometry. This means
that the sample holder cannot be rotated,
as is usually done to increase the homo-
geneity of the evaporated samples. The
translator resides on the top of the cham-
ber with the sample holder in the upper
part of the chamber. The sources are fed through the bottom of the vacuum chamber
allowing the samples to be grown upside down. This is needed for the operation of the
thermal evaporation sources and additionally avoids contamination of the samples by
falling debris. The sample holder can be heated via a large graphite heating element
sitting just above it. Two thermocouples are used to monitor the temperatures of the
heater and the substrate.

The sample holder can hold five samples at the same time which can then be used
for different experiments. Nearly all samples shown here were placed in the middle
of the sample holder, where the maximum thickness and homogeneity is possible. IR

(1550 nm) and red (650 nm) laser-light scattering (LLS) is utilized to monitor the sample's thickness on the substrates. The two lasers are aimed at the center sample and the diffuse reflection is detected by two detectors. The laser light enters and exits the chamber through glass windows at the bottom of the chamber. A quartz crystal microbalance *XTC/3* from *Inficon* is fed through the top of the chamber and connected via a measurement card to the preparation PC. It can be bent to the approximate position of the samples and measure the elemental flux of the sources.

There are three sources in the chamber, which are angled toward the middle of the sample holder: Two thermal evaporation sources for In and S and an electron beam evaporated source. 6N (99.9999 %) indium from *Alfa Aesar* is evaporated from a *RADAK II* furnace from *LUXEL* with a custom shutter and feed through. Standard In-flux rates for a growth rate of about $40\,\text{nm}\,\text{min}^{-1}$ are around 4 to $5\,\text{Å}\,\text{s}^{-1}$ obtained at a source temperature of $920\,°\text{C}$. 5N (99.999 %) sulfur from *Evochem* is evaporated from a custom thermal evaporation source without a shutter. The S-flux is less controlled, as the non-cooled source is additionally radiatively heated by the substrate heater. The temperature of the S-source is between 130 and $140\,°\text{C}$, which results in a flux of around $290\,\text{Å}\,\text{s}^{-1}$. This high flux creates a sulfur atmosphere in the chamber allowing for sulfur rich growth conditions for stoichiometric In$_2$S$_3$. The transition metals (3N+ V (99.9 %), 3N5 Nb (99.95 %), 4N5 Ti (99.995 %)) from *HMW Hauner* are evaporated as rods from a customized *e-flux Mini E-Beam Evaporator* from *tectra*. This electron beam source was improved to work better in the sulfur atmosphere by swapping all copper containing parts with aluminum. An additional shielding of the upper part of the E-beam improved the stability of the evaporation by reducing the amount of sulfur between filament and transition metal rod. Nevertheless, the evaporation is not always stable and depends strongly on the evaporated material. At higher voltages and currents needed for higher fluxes the risk of glow-discharges increases, limiting the maximum evaporation rate. While V was easiest to evaporate, it was more difficult to get higher fluxes with Ti and Nb. The reason was mainly the higher temperature needed for evaporation to start and the lower vapor pressure leading to a meltdown of the rods before a higher flux can be reached. To counter the low fluxes the growth rate had to be reduced to incorporate higher concentrations of the transition metals. The e-beam fluxes are varied to obtain the desired doping concentrations. Maximum stable rates were achieved with different acceleration voltages and beam currents: V with $1\,\text{kV}$

and $\sim$35 mA ($\sim$0.4 Å s^{-1}), Ti with 1 kV and $\sim$25 mA ($\sim$0.25 Å s^{-1}), Nb with 1.2 kV and $\sim$85 mA ($\sim$0.05 Å s^{-1}). The preparation process is controlled and monitored via a custom *LabView* program that is connected to the LLS-system and the *Eurotherm* PID controllers for the sulfur and indium sources.

Two sample sizes were used during the experiments, which should not impact the experiments' results. The 1 μm samples are grown on $10 \times 10 \times 0.7$ mm^3 Borofloat glass from *Schott*. The smaller size was originally chosen for the EXAFS experiment and allowed four equivalent samples to be grown in the middle of the sample holder. Samples used for XPS and UPS which are grown on $25 \times 25 \times 2$ mm^3 molybdenum coated float glass from *Guardian*, including a sodium diffusion barrier. The 60 nm thick samples for the absorption measurements are grown on $25 \times 25 \times 0.7$ mm^3 Borofloat glass. The Borofloat glass was chosen, because it is Na-poor and chemically and mechanically more stable than standard glass. Na-incorporation is known to change the properties of In$_2$S$_3$ (Barreau, Bernède, Deudon, et al. 2002; Barreau, Bernède, and Marsillac 2002), so any Na-diffusion was to be avoided. Additionally, the thin glass increases thermal conductivity and reduces light absorption and interference so the samples were suitable for a wide range of experiments. The glass was cleaned in an ultra-sonic bath with Rotisol and rinsed with bidistilled water. The substrate for photoluminescence measurements were additionally roughened by laser ablation to reduce interference effects. The Mo substrates for XPS and UPS were cleaned in a 10 % KOH solution and rinsed with bidistilled water. The samples for EXAFS were scraped off the glass using a piece of a silicon wafer to avoid detectable contaminations. Then they were mixed with high purity graphite powder and pressed into pellets with 8 mm diameter suitable for EXAFS measurements in fluorescence mode.

3.3   Sample lists

The sample names use the following schema: Abbreviated material name, floating point value for the doping concentration, single integer for the numbering of multiple similar samples, three digit integer value for the temperature. A 60 indicates 60 nm samples, no temperature indicates the standard 500 °C, no floating point value indicates no additional hyperdoping. For example **InS-1** is an undoped $\sim$1 μm thick In$_2$S$_3$ sample grown at 500 °C, **InSV-1.1-300** is a $\sim$1 μm thick In$_2$S$_3$:V sample with

~1.1 at.% V grown at 300 °C and **InSNb-60-0.2** is a ~60 nm thick In$_2$S$_3$:Nb sample with ~0.2 at.% Nb grown at 300 °C.

Table 3.1: *List of sample runs with $\sim 1\,\mu m$ thickness. The thickness was measured with a profilometer or estimated from laser light scattering (with leading $\sim$), the concentrations were measured using EDX with the SUPRA, except: * EDX measured with the Nova, $^{\diamond}$ measured with XPS, $^{\circ}$ estimated from process parameters. The measurements are valid for the sample in the center of the substrate holder.*

sample	$T_{substrate}$ (°C)	thickness (μm)	growth rate ($nm\,min^{-1}$)	e-beam (kV)	(mA)	concentration (at.%)
InS-1	500	1.0(1)	37.1	-	-	-
InS-2	500	1.1(1)	27.4	-	-	-
InS-3	500	$\sim$1.0	$\sim$27.2	-	-	-
InSV-0.1	500	1.0(1)	29.0	1	28	0.1(4)
InSV-0.5	500	1.1(1)	39.6	1.5	22	0.5(4)
InSV-0.5-2	500	$\sim$1.0	$\sim$27.7	1	32	0.5(4)
InSV-0.8	500	1.0(1)	19.1	1	32	0.8(4)
InSV-0.8-550	550	1.2(1)	32.2	1	32	0.8(4)
InSV-0.9	500	1.2(1)	40.6	1	32	0.9(4)
InSV-0.9-400	400	1.1(1)	44.7	1	32	0.9(4)
InSV-1.1-300	300	1.1(1)	40.7	1	32	1.1(4)
InSV-1.9	500	1.1(1)	38.0	1	34	1.9(4)
InSV-3.3	500	0.9(1)	33.5	1.5	25	3.3(4)
InSV-3.9	500	$\sim$0.7	$\sim$5	1	32	3.9(4)
InSV-5.3	500	1.0(1)	11.6	1	35	5.3(4)
InSV-5.7-400	400	1.1(1)	13.5	1	35	5.7(4)*
InSV-5.9-300	300	1.2(1)	12.7	1	35	5.9(4)*
InSTi-0.3	500	1.1(1)	21.8	1	26	0.3(4)
InSTi-0.5	500	1.1(1)	33.4	1	26	0.5(4)
InSTi-0.9	500	1.1(1)	18.4	1	23	0.9(4)
InSTi-0.9-400	400	1.1(1)	29.4	1	23	0.9(4)*
InSTi-0.8-300	300	1.2(1)	27.7	1	23	0.8(4)*
InSTi-2.1	500	1.1(1)	5.9	1	24	2.1(4)
InSTi-4.2-400	400	1.2(1)	7.1	1	23	4.2(4)
InSNb-0.2	500	1.1(1)	34.0	1.2	85	0.2(6)$^{\circ}$
InSNb-0.5	500	1.1(1)	13.7	1.2	85	0.5(6)
InSNb-1.1	500	1.0(1)	5.8	1.2	85	1.1(6)$^{\diamond}$
InSNb-1.5	500	1.1(1)	5.5	1.2	85	1.5(6)*
InSNb-1.6-400	400	1.1(1)	4.9	1.2	85	1.6(6)*
InSNb-1.4-300	300	1.1(1)	4.6	1.2	85	1.4(6)*
InSNb-2.9	500	0.2(1)	1.6	1.2	85	2.9(6)

Table 3.2: *List of sample runs with* 60 nm *thickness. The thickness was measured with XRR, the concentrations with RBS. Some concentrations were too low to be measured and are estimated from process parameters and marked with a* *. *The measurements are valid for the sample in the center of the substrate holder.*

sample	T$_{substrate}$ (°C)	thickness (nm)	growth rate (nm min^{-1})	e-beam (kV)	(mA)	concentration (at.%)
InS-60-1	500	61(1)	13.4	-	-	-
InS-60-2	500	60(3)	9.6	-	-	-
InSV-60-0.2	500	67(3)	10.3	1	22	0.2(2)*
InSV-60-0.5	500	63(3)	10.7	1	26	0.5(2)
InSV-60-1.2	500	60(1)	9.7	1	30	1.2(2)
InSV-60-3.0	500	58(2)	11.7	1	34	3.0(2)
InSTi-60-0.2	500	61(1)	9.3	1	21	0.2(2)*
InSTi-60-1.0	500	61(1)	8.8	1	26	1.0(2)
InSTi-60-1.8	500	62(1)	2.7	1	24	1.8(2)
InSTi-60-2.5	500	62(1)	2.2	1	25	2.5(5)
InSNb-60-0.2	500	47(1)	29.5	1.2	85	0.2(2)*
InSNb-60-1.1	500	54(1)	4.5	1.2	85	1.1(2)
InSNb-60-1.9	500	61(1)	2.6	1.2	85	1.9(2)
InSNb-60-2.3	500	61(2)	1.9	1.2	85	2.3(2)

Chapter 4

Analysis methods

This chapter details the various analysis methods used throughout this thesis. Each method is introduced with a description, the experimental details and how the analysis was conducted.

4.1 Scanning electron microscopy

Method fundamentals

Scanning electron microscopy (SEM) is one of the core methods to gather topographical and morphological data on grown samples. SEM offers the ability to image the surface, and with some preparation the cross-section, of a sample with a resolution of nanometers. This is useful to determine the surface size and shape of grown crystals.

To get an image resolution below the wavelength of visible light, electrons are used instead of photons. The electron beam is produced by an electron gun, accelerated, focused and directed by a combination of charged apertures and electromagnets. On the sample, the electrons can elastically scatter back, or excite atoms which release secondary electrons. The back scattered (BSE) and secondary electrons (SE) are separately detected by two detectors, amplified and combined with the parameters of the primary beam to form topological images of the sample.

The SE image depends on the depth where the electrons are excited. If the beam enters the sample perpendicularly, the penetration depth is at its maximum and few secondary electrons escape the sample. If the beam hits at an angle, or even an edge,

the distance to the surface is smaller and a lot more secondary electrons can escape the sample. This detection method is therefore well suited to display the topography and morphology with a high resolution.

The BSE image depends on the element atomic number of the material that is hit. Elastic scattering from heavy atoms is higher than from light atoms, which results in an elemental contrast. This method is useful to determine unwanted contamination of the sample or segregation of the elements.

Experimental setup

The main SEM used during the experiments is a *SUPRA 40VP* from *Zeiss* from the Optics Group of Prof. Dr. Georg Woltersdorf. The SE and BSE images are taken at $5\,\mathrm{kV}$ with magnifications ranging from 100x to 20000x. A second SEM/EDX setup was used during the maintenance of the *SUPRA 40VP*. It is a *Nova NanoLab 200* from *FEI* which is additionally equipped with a focused ion beam (FIB). This setup belongs to the Semiconductor Group of Prof. Dr. Marius Grundmann at the University of Leipzig and was operated by Jörg Lenzner. This system was also used for imaging cross-sections of samples utilizing the integrated FIB to cut into the sample. Unfortunately the contrast of the images was too low to be useable. Instead, samples were manually broken along a scratch created with a diamond cutter on the backside of the samples. This created rougher edges with better contrast in the SEM.

Since two different systems are used, they are distinguished as *SUPRA* and *Nova*.

Analysis method

The surface SE images of samples are analyzed with the measurement tool in *ImageJ* to get information about the crystallite sizes. A representative region of a sample at a magnification of about 20000x is chosen. Then the diameter (size) of a statistically large enough number of crystallites is measured manually. Some samples were imaged with both the *SUPRA* and the *Nova* to compare and validate the resulting statistics.

4.2   Energy dispersive X-ray spectroscopy

Method fundamentals

Energy dispersive x-ray spectroscopy (EDS) can measure the stoichiometrical composition of samples with a detection limit of below $1\,\text{at.\%}$.

In EDS the characteristic X-rays emitted by the excited atoms are accumulated in dependence of their energy by using a detector. This results in an X-ray spectrum that characterizes the atomic components of the material. The sample should be flat, uncoated and homogeneous at the measured area, to avoid an increase in uncertainty. One major advantage of EDX is the possibility to measure without a standard. A standardless analysis can be done knowing the electron beam energy and the composition of the material. The pure element EDX intensity for all elements in the material is calculated and compared to the measured spectrum. This allows the calculation of the concentration of the single elements which are normalized to a total of $100\,\%$.

Experimental setup

The EDS system used with the *SUPRA* consists of detector, processor *NumeriX* and software *IDFix* from *SAMx*. *IDFix* includes quantitative analysis procedures to automatically fit Gaussian distributions to the data, while considering the background. Together with the option to use ZAF, PAP or XPP correction to account for the atomic number, self-absorption and secondary fluorescence, this system allows the standardless determination of the stoichiometry of the samples with a detection limit of about $0.5\,\text{at.\%}$. To minimize effects from the rough surface and other inhomogeneities, the EDX measurement is done while sweeping the electron beam at a 100x magnification. This results in an average concentration over an area of roughly $3.5\,\text{mm}^2$. An acceleration voltage of $15\,\text{kV}$ was chosen to balance the unwanted penetration into the substrate with the needed energy to excite the atoms.

The EDS analysis on the *Nova* SEM is done with the *Nova 200 132-10* detector, the *EDAX-TSL Pegasus 4000 System* and the *EDAX Genesis version 6.02* software. The measured area at 100x magnification is in this case around $1.5\,\text{mm}^2$ with an acceleration voltage of $15\,\text{kV}$.

Analysis method

The analysis of the EDS on the *SUPRA* system is performed with *IDFix* by manually adjusting the background parameters and then quantifying the composition using the standardless ZAF quantification. On the *Nova* system the analysis is done with *EDAX Genesis* using standardless ZAF quantification. In all cases the relative amount of indium, sulfur and vanadium or titanium is extracted. The analysis of niobium-doped samples is problematic, because the energies of the K_α lines (16.521 and $16.615\,\text{keV}$) are so large that the $30\,\text{kV}$ necessary for suitable excitation results in a deep penetration into the substrate. The L_α lines on the other hand are with 2.163 and $2.166\,\text{keV}$ very near to the sulfur K_α lines (around $2.307\,\text{keV}$) which makes a separation of the two lines very difficult. (Deslattes et al. 2005)

The large number of possible errors related to the SEM, the EDS and the data analysis make a complete error analysis challenging. Nevertheless, from the fitting error, multiple measurements on the same system, as well as comparison with preparation parameters, other EDS system and other techniques like RBS, or XPS, the error can be estimated. Both EDS systems resulted in similar sample compositions, so we assume that none of the two systems introduce a large systematic error. This leaves the largest uncertainty to come from the data processing where the standardless approach results in a large error. Considering all of the above, an upper estimate of the error of the atomic concentration is around an absolute $0.4\,\text{at.\%}$. This absolute value is important for the lower doping concentrations, where the EDS spectrum fitting error alone can reach above $50\,\%$.

Exceptions are the EDX measurements of niobium. The overlap of the S K_α and Nb L_α lines forces the use of an acceleration voltage of $30\,\text{kV}$ to measure the Nb K_α line. As a result the electron beam penetrates deep into the substrate of the sample increasing the uncertainty of the measured atomic concentration. The upper estimate of the error is therefore increased to $0.6\,\text{at.\%}$.

The validity of the concentration measurements and error estimates is shown in section A.1 of the appendix.

The fit error for In and S given by *IDFix* is around $4\,\%$ relative which is much larger than needed for distinguishing the α- from the β-phase. The fit error from *EDAX Genesis* is much better at below $0.05\,\%$. A comparison between measurements

from both EDX systems and the crystal phases measured with XRD shows that the real uncertainty will probably be in the range of 0.5 to $1\,\%$. A reasonable upper estimate of relative $1\,\%$ can therefore be made for the measurement uncertainty of the In and S atomic concentrations.

As before the uncertainty in the measurements of Nb-doped samples increases due to the penetration into the substrate and the overlap of the S K_α and Nb L_α lines. An upper estimate of a relative $2\,\%$ uncertainty in the In and S atomic concentrations accounts for both effects.

4.3   X-ray diffraction

Method fundamentals

X-ray diffraction (XRD) can be employed to measure structural properties of the grown crystal layers. By scattering an X-ray beam off the sample, it comes to interference between the photons scattered by different lattice planes. For a certain photon wavelength λ, incident angle θ and lattice distance d all photons are scattered towards off the lattice plane with the same angle θ. This process is described by the Bragg equation 4.1:

$$n\lambda = 2d\sin\left(\theta\right) \tag{4.1}$$

By measuring the angle θ at which the X-rays with known wavelength are scattered the distance between two lattice planes can be measured.

As described in section 2.1.2 there are only a finite number of possible lattices and each lattice has a defined set of possible Miller index values. One measured reflex at a certain angle belongs to one or multiple lattice planes that have the same distance d. For an orthogonal crystal lattice this lattice plane distance d therefore depends on the chosen lattice plane (XRD peak, or reflex) described by the millier indices h, k and l and the lattice constants a, b and c describing the unit cell:

$$\frac{1}{d^2} = \frac{h^2}{a^2} + \frac{k^2}{b^2} + \frac{l^2}{c^2} \tag{4.2}$$

By combining equations 4.1 and 4.2 together with multiple reflexes it is possible to calculate the lattice parameters. The width of the XRD reflexes depend on the number

of parallel crystal planes (crystallite size), the order inside the crystals (microstrain) and also the measurement system itself (instrument broadening). In a single crystal all crystal planes are oriented the same way, everywhere inside the measured area. As such, there is only a detectable reflex if the exact angles needed to satisfy the Bragg equation in all three dimensions is hit. In reciprocal space the reflexes are points. In a polycrystalline material, the crystals in the sample are mostly oriented randomly so that at a certain angle, there are always a few crystallites that can satisfy the Bragg equation. In reciprocal space a powder creates spheres or shells, while a polycrystalline material, depending on the randomness of the oriented crystals, create shells with varying intensities and even holes.

There are different scan methods that measure different parts of the reciprocal space. In this case the Bragg-Brentano geometry is used, which uses a fixed sample, moving the X-ray source and detector towards each other. Incident angle ω and scattered angle θ are equal, with the angle between incident and scattered beam 2θ so that this method is also called θ-2θ. This measurement is often employed for powder and polycrystalline samples, where in reciprocal space one line scan covers most of the lattice planes. A favored growth direction (texture) can change the measured intensities of reflexes. Some planes might not grow in a direction that is measurable with θ-2θ measurements, unless the sample is tilted. This always has to be kept in mind when comparing samples with one another.

Experimental setup

The main diffractometer used for the analysis is the *PANalytical Empyrean* belonging to the Polymer Physics Group of Prof. Dr. Thomas Thurn-Albrecht. The CuK$_\alpha$ source is an *Empyrean Cu LFF HR* driven at $40\,\mathrm{kV}$ and $40\,\mathrm{mA}$ and positioned together with a *PIXcel-3D* area detector at a goniometer radius of $240\,\mathrm{mm}$. The sample stage is a Chi-Phi-Z stage which gives the maximum amount of freedom for the geometric calibration. A programmable divergence and anti-scatter slit combination is utilized to keep the irradiated and detected area the same for all angles. Two $20\,\mathrm{\mu m}$ nickel filters in the beam path minimize additional peaks from the aging Cu source as well as the Bremsstrahlung. Two $0.04\,\mathrm{rad}$ Soller slits reduce the sideways divergence of the X-rays. Once a day, the sample position calibration is performed with a paral-

lel beam setup. After this a dial indicator with a precision of $2\,\mu m$ is used to retain the height calibration after swapping samples. The samples are measured from $10°$ to $80°$ with a step size of $0.0066°$ and a counting time of $118\,s$ in Bragg-Brentano (θ-2θ) geometry. The sample stage is fix, while source and detector are moved, measuring all crystal planes parallel to the surface of the sample. Diffractograms from a second diffractometer (*Bruker D8 Discover*) operated by Dr. Diana Rata from the Functional Oxydic Boundaries Group of Prof. Dr. Kathrin Dörr were used verify the results from the *PANalytical Empyrean* and evaluate systematic errors.

Some peaks in the θ-2θ-scans (see figure 5.27) were identified as measurement artifacts, repeating for every strong reflex. They come from the degrading Cu-source installed in the diffractometer. These additional reflexes are peaks in the X-ray spectrum which are diffracted together with the bremsstrahlung and the Cu-characteristic peaks and are therefore easy to identify. To reduce their intensity together with the CuK$_\beta$ peak a second Ni-filter was used during the measurement which still could not completely eliminate these peaks. Figure 4.1 compares two samples that were measured with one and two nickel filters. All reflexes created by diffraction in the sample should have a similar signal-to-noise ratio. The peaks that nearly vanish are the ones present in the X-ray spectrum of the Cu-source and have been discarded for the analysis.
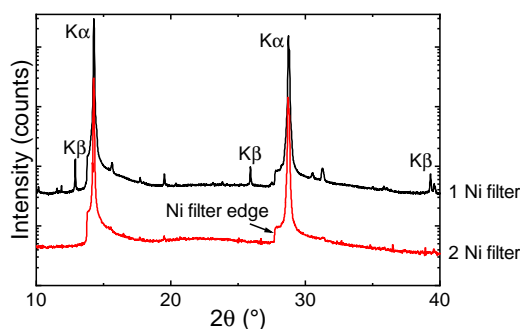
Figure 4.1: *Diffractograms of two comparable In$_2$S$_3$ samples measured with 1 and 2 Ni-filters. All peaks with reduced signal-to-noise ratio come from the X-ray source spectrum and not the sample.*

Analysis method

The diffractograms are visualized in *OriginPro* and smoothed with a Savitzky-Golay filter with a 20 point window and a polynomial of the 5th order. This reduces spikes and noise without degrading the peak shapes. The peak profile fitting of the diffractograms is done with *PDXL2* from *Rigaku* by fitting all peaks simultaneously after manually adjusting the automatically fitted background. Pearson profiles are chosen for highly crystalline samples with a dominating Lorentz shape, while pseudo-Voigt profiles were used for lower crystalline samples with a larger Gaussian component. Some samples have a slight peak asymmetry so that split peak shapes have to be used for the best fit. The *PDF-4+* database was utilized to check for secondary phases, polymorphy and to index the diffraction peaks. With *OriginPro*, *Mathematica* and *Python* the resulting peak parameters are further analyzed by calculating texture coefficients, lattice constants and microstrain.

The texture coefficient t is calculated using the Harris method (Harris 1952) described by the formula:

$$t = \frac{I_{hkl}/I_{hkl}^{\text{powder}}}{\frac{1}{N}\sum_{i,j,k} I_{ijk}/I_{ijk}^{\text{powder}}} \tag{4.3}$$

with the integrated intensity of the measured reflex I_{hkl}, the integrated intensity of the same reflex in a powder sample I_{hkl}^{powder} and the number of reflexes of the reference N. In this case $N = 24$ between 10° and 80° for the cubic reflexes (α-In$_2$S$_3$). The lattice plane distance d is calculated by using the Bragg equation 4.1

$$d = \frac{\lambda}{2\sin(\theta)} \tag{4.4}$$

with the diffraction angle θ and the known wavelength λ of the X-rays. For a cubic lattice the dependence of the lattice plane distance d on the Miller indices hkl in equation 4.2 can be simplified. With $a_{cub} = b = c$ it follows

$$\frac{1}{d^2} = \frac{h^2 + k^2 + l^2}{a_{cub}^2} \tag{4.5}$$

$$a_{cub} = d\sqrt{h^2 + k^2 + l^2} \tag{4.6}$$

The lattice constants of the tetragonal lattice are more complicated to calculate,

since there are two: a_{tet} and c_{tet}. From 4.2 with $a_{tet} = b$ follows:

$$\frac{1}{d^2} = \frac{h^2 + k^2}{a_{tet}^2} + \frac{l^2}{c_{tet}^2}$$ (4.7)

As a result we have two unknown variables and need to combine the data of two diffraction peaks. The following equations are derived from an equation system using equation 4.7 for two peaks:

$$a_{tet} = \pm i \frac{d_1 d_2 \sqrt{(h_2^2 + k_2^2)l_1^2 - (h_1^2 + k_1^2)l_2^2}}{\sqrt{d_2^2 l_2^2 - d_1^2 l_1^2}}$$ (4.8)

$$c_{tet} = \pm i \frac{d_1 d_2 \sqrt{(h_2^2 + k_2^2)l_1^2 - (h_1^2 + k_1^2)l_2^2}}{\sqrt{d_1^2(h_1^2 + k_1^2) - d_2^2(h_2^2 + k_2^2)}}$$ (4.9)

with the Miller indices h, k and l of the two peaks, the lattice plane distances d of the two peaks calculated using equation 4.4. The real positive solutions are the correct lattice constant values. This calculation does not work for certain hkl combinations, where $(h_2^2 + k_2^2)l_1^2$ equals $(h_1^2 + k_1^2)l_2^2$. To analyze the strain inside crystallites the modified Scherrer formula (Balzar et al. 1996; Fermin et al. 2019) can be used:

$$\beta = \frac{K\lambda}{L\cos\theta} + 4\varepsilon\tan\theta + \beta_{inst}(\theta)$$ (4.10)

This equation includes the original Scherrer formula with the grain shape constant K, the X-ray wavelength λ, the average grain or crystallite size L and the Bragg angle θ. $\beta_{inst}(\theta)$ describes the angle dependent instrument broadening. The additional part with the microstrain ε includes any defects introduced into a crystallite or grain, which increase the full width at half maximum (FWHM) of a reflex. The definition for microstrain is the change of the lattice plane distance in a crystal grain given in percent:

$$\varepsilon = \frac{d' - d}{d}$$ (4.11)

where d and d' are the lattice plane distances before and after the deformation of the crystal due to lattice defects. The advantage of this formula is that the broadening due to small grain size is separated from potential strains inside a grain and allows the calculation of said strains. By plotting the FWHM against the Bragg angle θ for

multiple reflexes, a fit to equation 4.10 can be used to obtain crystallite size L and microstrain ε. This method is best for comparing samples, as the absolute calculated microstrains contain unknown systematic errors. The instrument broadening $\beta_{inst}(\theta)$ is estimated with a linear regression between two reference measurements on $1\,1\,1$ and $1\,0\,0$ silicon wafers. The crystallite size is known from SEM measurements, so only the microstrain has to be fitted, improving the fit accuracy. Fitting is done in *Python* with the *scipy.optimize.curve_fit* function from the *scipy* package.

4.4   Grazing-incidence wide-angle X-ray scattering

Method fundamentals

Grazing-incident wide-angle X-ray scattering (GIWAXS) uses the same principles as XRD as X-rays are scatterd off the crystal's lattice planes. The difference is a very low incident angle in the range of a few degrees and a 2D detector that enables the measurement of an area of the reciprocal space. In the wide-angle method employed here, the 2D detector is close to the sample so that it measures a large area of the reciprocal space.

In contrast to XRD in Bragg-Brentano geometry, the 2D measurement of the reciprocal space allows the direct analysis of the texture and reflexes that might not be detectable in a line scan. Due to the high sensitivity of this method, low intense reflexes are visible and secondary phases are easier to detect.

As the measurement is still 2D in a 3D reciprocal space, one dimension is not considered. In our case the measurement displayed the planes angled in the direction of the X-ray beam and perpendicular to the beam, which leaves out the rotation of the crystals along the axis perpendicular to the sample's surface.

Experimental setup

The GIWAXS experiments were performed using a *SAXSLAB* laboratory setup from *Retro-F* equipped with a CuKα microfocus X-ray source and a multilayer X-ray optics (ASTIX) as a monochromator from *AXO DRESDEN*. A *PILATUS3 R 300K* detector from *DECTRIS* was used to record the 2D WAXS patterns. It belongs to the Polymer

Physics Group of Prof. Dr. Thomas Thurn-Albrecht and was operated by Dr. Oleksandr Dolynchuk. The measurements were performed in reflection geometry in vacuum at room temperature. The sample to detector distance was around $89\,\text{mm}$. Proper alignment of source and sample were done to minimize geometric errors. The best incident angle to get point-like reflexes and a large reciprocal area was $3°$. The measurement time was $3600\,\text{s}$

Analysis method

The analysis of the GIWAXS data was done using *SAXSGUI 2.19.02.* This program allows the visualization, transformation and averaging of the raw data obtained during the experiment. For the visualization all colormaps are made with the same parameters, including the same logarithmic intensity-scale. The raw data were transformed to display the reciprocal coordinates $q_r = \sqrt{q_x^2 + q_y^2}$ (parallel to the surface of the sample) versus q_z (perpendicular to the surface of the sample) to correct the effect of the curved reciprocal space on a flat detector. The geometry of the experiment results in blind spots in reciprocals space along the q_z axis and between the three active detector regions. For further analysis an averaging along the Debye-Scherrer rings following $|q_r + q_z| = const$ is done, creating diffractograms similar to θ-2θ measurements on a powdered material. These resulting averaged diffractograms are then fitted with split pseudo-Voigt profiles using *PDXL2* from *Rigaku.*

4.5   X-ray reflectometry

Method fundamentals

X-ray reflectometry (XRR) is a technique to analyze surfaces, thin films and even multilayer samples. An X-ray beam is reflected off a sample at a low angle and the angle dependent changes of the intensity are analyzed. The reflection depends on the X-ray wavelength, the material and its density, the layer thickness and the roughness of the surface. In this case, it is used to estimate the thickness of thin In_2S_3 layers on Borofloat glass.

Experimental setup

The *PANalytical Empyrean* used for XRR is the same as in section 4.3. In this case the calibration and measurement are performed with the parallel beam setup. The reflections off the samples are measured in the range $0.04°$ to $4°$ with a step size of $0.001°$ with the goniometer in θ-2θ mode.

Analysis method

The analysis is done in the *X'Pert Reflectivity* software from *PANalytical*. The best results were obtained assuming a SiO_2 substrate layer with a fixed thickness. Density and roughness of both the In_2S_3 and SiO_2 layers are fitted together with the thickness of the In_2S_3 layer.

The obtained thicknesses can be directly compared with the LLS thickness measurement during the growth process. The processes were aimed for the first red laser light interference extremum which in our geometry translates to a thickness of roughly $60\,nm$. The XRR measurement results displayed in table 3.2 verify that this thickness of $60\,nm$ could be achieved. The errors given by the XRR fits were in the range 0.1 to $1\,nm$ for the $60\,nm$ samples. There are various assumptions involved in the fits like the use of SiO_2 and some samples were more difficult to fit. An upper estimate of the uncertainty would be in the range of 1 to $3\,nm$ for a $60\,nm$, depending on the fit quality.

4.6   Extended X-ray absorption fine structure

Method fundamentals

While XRD yields long range order structural properties, it is also possible to look at the local structure around atoms. One method to do this is Extended X-ray absorption fine structure (EXAFS). It utilizes the X-ray energy dependent absorption of an atom at the absorption edge, also called X-ray Absorption Near Edge Structure (XANES), and above the absorption edge to get information about the binding partners, their number and distances.

The absorption edge is at the photon energy where the excited electrons can escape the atoms: The binding energy. These photoelectrons can be described as waves

moving out from the atom. The electron waves can reflect of neighboring atoms and interfere with the outgoing electron waves. At the position of the absorbing atom the constructive and destructive interference of the electron waves change the absorption coefficient. This energy dependent absorption change is detectable when using well monochromated and defined X-rays. Such X-rays are generated in Synchrons where electrons are kept near light speed at a well-defined kinetic energy and bend around a circle. The energy of the resulting white X-ray bremsstrahlung can be further increased by wigglers or undulators, forcing the electrons into zigzag paths via alternating magnets. A double crystal monochromator consisting of two Si single crystals is often used to diffract the beam into a narrow energy beam with an energy width in the range of $1\,\mathrm{eV}$. The energy width determines the resolution of the experiment and is a trade-off with the intensity of the beam. Two ways can be utilized to detect the absolute changes: Through the transmission or the fluorescence of the material. In our case we use fluorescence to measure the absorption, where the filling of the core electron holes after absorption creates detectable photons. The fluorescence intensity is dependent on the absorption coefficient of the material and used to measure the EXAFS. The fluorescence is detected via semiconductor detectors.

Experimental setup

For each measured In_2S_3:V sample two 10×10 mm $1\,\mu\mathrm{m}$ samples from the same preparation run were scraped off the substrate using silicon wafers and pressed together with high purity graphene into pellets with $8\,\mathrm{mm}$ diameter. This step was necessary to measure the samples in fluorescence mode and avoid impurities that could potentially lower the EXAFS quality.

The EXAFS experiment was conducted over three days in April 2018 at the *European Synchrotron Research Facility (ESRF)* in Grenoble on Beamline *BM08* with the experiment number *MA-3671*. This beamline is using the X-ray beam from a bending magnet and a pair of $1\,1\,1$ silicon crystals as the monochromator. The measurement team consisted of Dr. Claudia Schnohr, Stefanie Eckner and Konrad Ritter from the Friedrich-Schiller-University Jena, together with Martin Schiller and Leonard Wägele from the Martin-Luther-University Halle-Wittenberg. Fluorescence was the chosen measurement mode because of the low concentrations of the transition metals and the

small volume of the sample material. The low signal intensity also did not allow the use of Beryllium windows and therefore vacuum. Kapton windows were used instead and the measurements had to be conducted at room temperature.

A reference sample containing no vanadium was measured to make sure that only the incorporated V would create a fluorescence signal. The spectrum was measured around the V K edge at $5.465\,\mathrm{keV}$. Due to the low signal-noise-ratio, time constraints and the two suboptimal V-reference samples (VO_2 (containing V_6O_{13}) and V_2O_5) it was decided to focus on the V-hyperdoped samples and conduct repeated measurements. This allowed for measurement combinations to increase the signal-to-noise ratio. A reference V-foil is measured to be able to calibrate the measured energy scale.

Analysis method

The EXAFS analysis is done using *IFEFFIT* (()Newville2001) together with *ATHENA* and *ARTEMIS* (B. Ravel et al. 2005). Structure models are made with *ATOMS* (Bruce Ravel 2001) and the calculated spectra with *FEFF9* (Rehr et al. 2010). The analysis was conducted as part of the Master thesis by Martin Schiller and follows known procedures from literature and is not shown here with all details (Kelly et al. 2015; Claudia S. Schnohr et al. 2014).

The first step is to calculate the absorption coefficient μ from the fluorescence intensity. For this the fluorescence intensity I_f is divided by the incoming intensity I_0 to get a value proportional to the absorption coefficient:

$$\mu \sim \frac{I_f}{I_0} \tag{4.12}$$

Then the energy scale is calibrated using the reference V-foil. By fitting the background before and after the edge, the spectrum can be normalized and the influence of the background spectrum removed. After this, the absorption rises from 0 to 1 at the absorption edge and oscillates around 1 in the EXAFS region of the spectrum.

The quality of the spectra are evaluated at this point to only use the ones that have a high signal-to-noise ratio. By combining the best spectra, the overall signal-to-noise ratio of the XANES or EXAFS signal is optimized. While the XANES analysis does not require any more preprocessing, the EXAFS analysis requires the extraction of

the fine structure χ. This is done by subtracting the remaining background μ_b above the absorption edge from the normalized absorption coefficient μ_n and dividing the result by the absorption edge height $\Delta\mu_0$. By additionally converting the energy to wavenumbers k using the photonenergy of the X-ray beam E, the absorption edge energy E_0, the mass of the electron m_e and Planck's constant $\hbar$

$$k = \sqrt{\frac{2m_e(E - E_0)}{\hbar^2}} \tag{4.13}$$

we get

$$\chi(k) = \frac{\mu_n(k) - \mu_b(k)}{\Delta\mu_0} \tag{4.14}$$

By Fourier transforming $\chi(k)$ to real space it is possible to select the influence of the nearest neighboring atoms. Two windows are used for this process: One to select and weight the data in k-space, and one to select one part of the signal in real space. After this preprocessing, it is possible to fit a theoretical model on the data. The EXAFS equation is used to describe the absorption fine structure $\chi(k)$ depending on the electron wave number and the local structure and can therefore be used to fit a model to the measured $\chi(k)$. The EXAFS equation is given by

$$\chi(k) = \sum_i S_0^2 N_i \frac{|f_i(k)|}{kR_i^2} e^{-\frac{2R_i}{\lambda(k)}} e^{-2\sigma_i^2 k^2} \sin(2kR_i + 2\delta_c(k) + \delta_i(k)) \tag{4.15}$$

which sums over the different scattering paths and includes the electron wave number k independent amplitude reduction factor S_0^2, the number of identical scattering paths N_i, the complex back-scattering amplitude $f_i(k)$, the mean interatomic distance R_i, the mean free path length of the electron wave $\lambda(k)$, the standard deviation of the atom distance distribution σ_i and the phase shift induced by the potential of the absorbing atom δ_c.

Interesting for us are is the amplitude reduction factor S_0^2, as it contains the coordination number N of the material multiplied by a factor. N should allow the distinction between a tetragonally or octagonally coordinated transition metal. The mean interatomic distance R can be used to verify the position of the transition metal inside the In_2S_3 host structure. The position of the measured absorption edge itself is also of interest as it also depends on bond length of the absorbing atom. The accuracy of the

position of the absorption edge can be estimated when comparing multiple measurements of each sample. Half of the spread of the absorption edge values is taken as the uncertainty. The uncertainty of the EXAFS parameters is taken from the fits.

4.7   Rutherford backscattering spectroscopy

Rutherford back-scattering spectroscopy (RBS) is the main technique used to measure the stoichiometry of the $60\,\mathrm{nm}$ samples, including the hyperdoping concentration. In RBS, alpha particles (He-ions) are created and accelerated to energies in the low MeV range and then scattered off the sample. Due to inelastic scattering with the nuclei in the sample, the ions scatter back with lower energies. A detector is used to determine the energy and intensity of back-scattered ion-beam. The particles' energy loss depends on the scattering cross-section of the samples' nuclei and therefore on the mass and the atomic number. This element specific energy loss can be utilized to measure the stoichiometry of the sample. Due to additional loss of kinetic energy from scattering off the electrons in the material, the $1000\,\mathrm{nm}$ cannot be measured as the stopping power is too great and the particles cannot escape the material for measurement.

The measurements were conducted and analyzed by Dr. Jura Rensberg at the $3\,\mathrm{MeV}$ Tandetron accelerator JULIA of the Ion Beam Physics group of Prof. Dr. Elke Wendler from the Friedrich-Schiller-University Jena.

4.8   Raman spectroscopy

Method fundamentals

Raman spectroscopy utilizes the inelastic scattering of monochromatic light in a solid material. Raman spectra can include information about the material composition, crystallinity, crystal orientation and stress.

The Raman spectrum contains three parts. The elastic Rayleigh scattering, where the wavelength does not change, and the two parts of inelastic Raman scattering, where the wavelength is either Stokes shifted to larger wavelengths, or anti-Stokes shifted to smaller wavelengths. Rayleigh scattering occurs on objects smaller than the incident wavelength. The photon is absorbed by a molecule which enters a higher energy vir-

tual state and immediately relaxes to the original state by emitting a photon of the same energy. As such, the Rayleigh scattered photons do not contain useful information about the scattering material. The prime example is the sunlight scattering in the atmosphere, where the higher scattering cross-section of the blue light results in the blue sky and red sunsets. In Raman scattering the system also enters a high energy virtual state, but instead relaxes to a different final state. The loss, or gain of energy through this process is added (Stokes), or subtracted (anti-Stokes) from the emitted photon, respectively. This inelastic scattering is only possible if there are other energy states available next to the ground state. These can be for example molecular vibrations or phonons in a crystal lattice. Since these energy states have distinct energies depending on the molecules and environment a lot of information can be obtained from Raman measurements. If $\hbar\omega_0$ is the energy of the photon and $\hbar\omega_p$ is the energy of the phonon, the scattered photon then has the energy $\hbar\omega_s$

$$\text{Stokes:} \quad \hbar\omega_s = \hbar\omega_0 - \hbar\omega_p \tag{4.16}$$

$$\text{Anti-Stokes:} \quad \hbar\omega_s = \hbar\omega_0 + \hbar\omega_p \tag{4.17}$$

The Raman shift, typically given in wavenumbers k_{shift} with the unit cm^{-1}, is equivalent to the energy of the phonon and is derived from

$$\hbar\omega_p = \hbar(\omega_0 - \omega_s) = hc(k_0 - k_s) \tag{4.18}$$

$$\rightarrow k_{shift} = k_0 - k_s = \frac{1}{\lambda_0} - \frac{1}{\lambda_s} \tag{4.19}$$

As a result, a Stokes shift gives a positive Raman shift and the anti-Stokes shift a negative Raman shift. Figure 4.2 displays and summarizes the elastic and inelastic scattering possibilities in Raman spectroscopy.
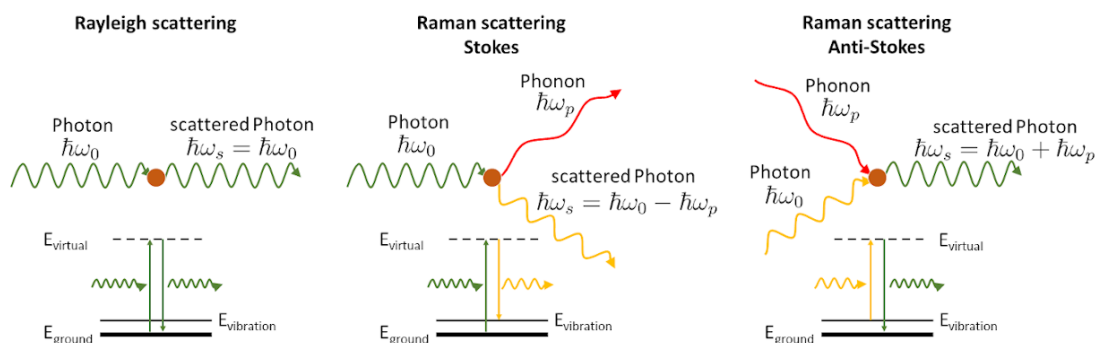
Figure 4.2: *Diagram of the three scattering possibilities in Raman spectroscopy.*

Unfortunately most photons are Rayleigh scattered and not Raman scattered so the required laser intensity or integration length is high. Therefore, the Rayleigh scattering has to be reduced for high quality Raman spectra.

Experimental setup

Back-scatter Raman spectroscopy was performed with a *LabRAM HR Evolution* from *HORIBA* belonging to the Microstructure-based Material Design Group of Prof. Dr. Ralf Wehrspohn. It includes a microscope, which allows for high local intensities with a 100x objective. The laser is a frequency doubled Nd:YAG solid state laser with a wavelength of $532\,\mathrm{nm}$ and $100\,\mathrm{mW}$ of power. A $1\,\%$ ND filter is used to reduce the power and avoid damaging the sample when using the $100\times$ objective. A CCD detector coupled with a monochromator with a $1800\,\mathrm{gr/nm}$ grating enables the acquisition of the Raman spectra. The standard setting was to measure one acquisition between 20 and $540\,\mathrm{cm}^{-1}$ with an acquisition time of $240\,\mathrm{s}$. Before the measurements of the day, a calibration with a Si wafer with a known Raman peak position was done. No polarization was used and all measurements were conducted at room temperature. To avoid measuring inhomogeneities, three measurements at different sample positions were done and compared. If one differed, a fourth measurement was done. The three spectra are then averaged to increase the signal-to-noise ratio.

Analysis method

OriginPro 2019 from *OriginLab* was used to plot the Raman spectra. No detailed analysis was conducted and the Raman peak positions were estimated via the data cursor available in *OriginPro*.

4.9   UV-VIS-NIR absorption spectroscopy

Absorption Spectroscopy in the visible and near-visible range is a widely used method to characterize optical properties of a material. It has been used for In_2S_3:TM in particular to show defect states within the band gap, in experiment as well as theory (Chen et al. 2013; Lucena, Conesa, et al. 2014; McCarthy, Weimer, Haasch, et al. 2016).

Method fundamentals

The optical absorption of a material is determined by quantum mechanical probabilities of transitions between energy states in its electronic band structure. In an optimal semiconductor the absorption of energies below the band gap is zero and rises abruptly near the band gap energy of the material, where the energy is high enough to excite electrons from the valence band into the holes of the conduction band. The absorption spectrum is also dependent on the band structure around the band gap, as a direct transition from band to band is more likely than an indirect transition which has to involve a phonon to not violate the momentum conservation. This material property is very important for the operation of a solar cell where direct transitions decrease the required thickness of a material and therefore the cost of solar cells.

Experimental setup

The UV-VIS-IR absorption spectroscopy measurements were performed with a *Lambda 900* from *PerkinElmer* belonging to the Polymer Physics Group of Prof. Dr. Thomas Thurn-Albrecht. This spectrometer is configured to use a deuterium lamp for the UV region below $319.2\,\mathrm{nm}$ and a halogen lamp for the whole VIS-IR region. The utilized detectors are a photo-multiplier tube for the UV-VIS region down to $830\,\mathrm{nm}$ and a PbS detector for the rest of the IR region. The *Lambda 900* has the option to use a

second parallel beam for reference substrate measurements. Instead of using this, the substrates were measured separately to be more flexible in the analysis.

Transmission measurements were performed by placing the samples with the In_2S_3 layer first into the beam. The sample holder ensures a 90° angle between sample and beam. Reflectance measurements are done using a sample holder with mirrors that reflect the light beam off the sample and guide it back to the detector.

Before the measurement series of a day, the lamps were warmed up for at least 30 minutes to stabilize the lamp spectra. Then a dark measurement, as well as a light measurement without a sample (for transmission) or with the reference mirror (for reflectance) were conducted to calibrate the system before use. The samples were carefully placed into the $\sim 4.5 \times 2.5\,\mathrm{mm}$ beam to ensure the measurement of the same spot in transmission and reflection. The measurements were performed at room temperature from 2200 to 250 nm with 1 nm steps.

Two sets of samples were measured. One set of about 60 nm thick samples specifically grown for this experiment and the 1000 nm set used in other experiments as well. The thicknesses of the layers were determined with two different methods. The 60 nm samples were measured with X-ray reflectometry (XRR) 4.5, the 1000 nm samples with a profilometer (see section 4.12). Bare Borofloat substrates were measured as a reference to be used for transmission correction and for sample modeling using the transfer matrix method A.6.

Analysis method

The absorption spectroscopy analysis was done with a self written *Python* program to be able to quickly implement and apply analysis changes to all measurements.

The preparation of the data starts with a correction of the detector change, which leaves a step in the spectrum at 830 nm. This is implemented by averaging the transmittance T and reflectance R values at 828 and 832 nm and shifting the two parts of the spectrum to meet this average at 830 nm.

$$\lambda < 830: \quad R_{corrected}(\lambda) = R(\lambda) + \frac{R(828nm) - R(832nm)}{2} \tag{4.20}$$

$$\lambda < 830: \quad T_{corrected}(\lambda) = T(\lambda) + \frac{T(828nm) - T(832nm)}{2} \tag{4.21}$$

$$\lambda >= 830: \quad R_{corrected}(\lambda) = R(\lambda) - \frac{R(828nm) - R(832nm)}{2} \tag{4.22}$$

$$\lambda >= 830: \quad T_{corrected}(\lambda) = T(\lambda) - \frac{T(828nm) - T(832nm)}{2} \tag{4.23}$$

The next step is the correction of the reflectance measurement, as the imperfect reference mirror with below $100\,\%$ reflectance suggests a higher reflectance in the measurements. The known reflectance of the reference mirror R_{mirror} is multiplied by the measured sample reflectance $R_{measured}$ to get the real reflectance.

$$R = R_{measured} \cdot R_{mirror} \tag{4.24}$$

An additional systematic error can be introduced, if the reference mirror has aged since its last measurement. This would be visible in all measurements and does not impact the comparison of samples.

The transmittance includes the properties of the glass substrate which have to be considered. By measuring the glass substrate on its own, its impact on the absorption can be estimated. The sample transmittance $T_{measured}$ can then be divided by the substrate transmittance $T_{substrate}$ to reduce the transmission losses due to said substrate.

$$T = \frac{T_{measured}}{T_{substrate}} \tag{4.25}$$

The problem with this route is the difference in the refractive indices of the involved media. The air/glass interface of the reference measurement will have a different reflectance than the In_2S_3/glas interface, leading to an error of the measured transmittance. This problem can be overcome by utilizing the transfer matrix method explained in the appendix A.6 or by separating the In_2S_3 layer from the glass which has not been done.

Due to the sub-optimal correction of T and R, there is a possibility of $T + R$ reaching above $100\,\%$, indicating a negative absorption. The sum of T and R is projected into the 0-100 $\%$ range by calculating a correction factor, which is then applied to both spectra.

$$T_{corrected} = \frac{100\%}{\max(T + R)} \cdot T \tag{4.26}$$

$$R_{corrected} = \frac{100\%}{\max(T + R)} \cdot R \tag{4.27}$$

Unfortunately the surface roughness can scatter the light away from the beam path, so that this transmitted or reflected light does not reach the detector. This part of the light is then falsely attributed to the absorption. Since especially the $60\,\text{nm}$ samples are very smooth, this additional error of the absorption is assumed to be small. What is also present in the transmittance and reflectance spectra is noise from the detector which can be minimized by using a smoothing algorithm without changing the quality of the data. The best results were obtained with a Savitzky-Golay filter (*savgol_filter* from the *SciPy-Python* package), which was utilized to fit polynomials of the 4th order to a window of $81\,\text{nm}$.

After this preparation the absorption can be calculated from the Beer–Lambert law:

$$R + T = \text{e}^{-\alpha d} \tag{4.28}$$

$$\Rightarrow \alpha = -\frac{1}{d} \log(T + R) \tag{4.29}$$

with the absorption coefficient α and the sample thickness d. This formula does not consider internal reflections inside a sample.

Alternatively a widely used approximation of the transmittance (compare with equation 4.32) can be used that includes the back surface reflectance:

$$T \approx (1 - R)^2 \, \text{e}^{-\alpha d} \tag{4.30}$$

$$\Rightarrow \alpha \approx -\frac{1}{d} \log\left(\frac{T}{(1 - R)^2}\right) \tag{4.31}$$

This equation is only valid for thin films on a non-absorbing substrate at higher absorption values around and above the band gap. Below the band gap it results in negative absorption coefficients.

A better approach is to use the complete formula that includes multiple internal reflections (Malerba et al. 2011). The measured transmittance T and reflectance R values are dependent on the single surface reflectance R_0 and the absorption coefficient α

$$T = \frac{I_T}{I_0} = \frac{(1 - R_0)^2 \, \text{e}^{-\alpha d}}{1 - R_0^2 \, \text{e}^{-2\alpha d}} \tag{4.32}$$

$$R = \frac{I_R}{I_0} = R_0 \left(1 + \frac{(1 - R_0)^2 \, e^{-2\alpha d}}{1 - R_0^2 \, e^{-2\alpha d}} \right) \tag{4.33}$$

where I_0 is the incident intensity, I_T the transmitted intensity and I_R the reflected intensity. Both equations can be combined to eliminate the single surface reflectance R_0 and obtain the absorption coefficient

$$\alpha = \frac{1}{d} \log \left(\frac{1 + R^2 - 2R - T^2 + \sqrt{(1 + R^2 - 2R - T^2)^2 + 4T^2}}{2T} \right) \tag{4.34}$$

A comparison of these methods to obtain the absorption coefficient is provided in the appendix A.5 and includes sample modeling by combining the Fresnel equations with the transfer matrix method. The latter approach was computationally intensive, but did not result in significantly better results than formula 4.34. Especially the $1000 \, \text{nm}$ samples performed much worse, so the absorption analysis is done using equation 4.34.

Interference is expected when working with thin films in the range of the used wavelength. The formula to calculate reflective constructive interference when no phase changes occur is given by

$$2nd \cos(\theta) = m\lambda \tag{4.35}$$

with the refractive index n, thin film thickness d, angle of incident light θ, order of interference m and wavelength of incident light λ. If the thin film has a higher refractive index than air and the substrate, one phase change at the surface occurs, which shifts the wave by $\frac{\lambda}{2}$. The constructive interference then changes to

$$2nd \cos(\theta) = (m + \frac{1}{2})\lambda \tag{4.36}$$

For a known thickness and refractive index the interference maxima can then be calculated by

$$\lambda = \frac{2nd \cos(\theta)}{m + \frac{1}{2}} \tag{4.37}$$

The refractive index n can also be calculated from the interference maxima T_M and

minima T_m and the known refractive index of the substrate n_0.

$$n = \sqrt{N + \sqrt{N^2 - n_0^2}} \tag{4.38}$$

with

$$N = 2n_0 \frac{T_M - T_m}{T_M T_m} + \frac{n_0^2 + 1}{2} \tag{4.39}$$

To determine the optical band gap of a material, a so called Tauc plot can be used (Tauc et al. 1966). It utilizes the effect that different transition types result in different shapes of the absorption spectrum. More specifically, the x-axis intercept of the extrapolation of linear parts of a $(\alpha E)^r$ versus E plot results in the band gap. For this to work, one has to know what kind of transition is present at what energy interval and use the correct value for r.

$$\begin{aligned} r &= 2 \quad \text{for a direct allowed transition} \\ r &= 2/3 \quad \text{for a direct forbidden transition} \\ r &= 1/2 \quad \text{for an indirect allowed transition} \\ r &= 1/3 \quad \text{for an indirect forbidden transition} \end{aligned} \tag{4.40}$$

Sometimes the slope of the Tauc plot is not directly going to 0, but ends in a background spectrum from e.g. scattered light. In this case the x-intercept is switched with an intercept with a fit to the background slope. Otherwise, the band gap energy will be underestimated.

If a disorder is present in the lattice where the absorption occurs the band edges extent into the band gap of the material. This extension is called the Urbach tail which follows an exponent dependent on the Urbach energy E_U (Studenyak et al. 2014; Urbach 1953).

$$\alpha(E) = \alpha_0 \, e^{\frac{E - E_0}{E_U}} \tag{4.41}$$

α_0 is a constant and E_0 is the onset of the tail and often taken as the band gap. E_0 can be omitted for the determination of the Urbach energy E_U, as it does not impact the slope:

$$\ln(\alpha(E)) = \frac{E}{E_U} - \frac{E_0}{E_U} - \ln(\alpha_0) \tag{4.42}$$

4.10   Photoluminescence spectroscopy

Photoluminescence (PL) is a spectroscopic technique to get information about opto-electronic properties of a material. By optically exciting electrons into higher energy states, like the conduction band, the recombination paths of the electrons and holes can be analyzed. This can lead to an understanding of the band positions, defect states and recombination mechanisms.

Method fundamentals

The absorption of the photons of the exciting light is necessary for the PL-technique to work. As such the light energy is usually chosen to be above the band gap energy to excite electrons to, or above the conduction band. The free charge carriers can then recombine using the available recombination paths in the material.

Three recombination paths are distinguished: Radiative recombination, defect recombination and Auger recombination (see chapter 2.2). The radiative recombination is the only one that is visible in photoluminescence and therefore necessary to use this technique. There are a few radiative recombination paths that can be observed in semiconductors. The band-band-recombination is typically an electron in or near the conduction band minimum recombining with a hole in or near the valence band maximum. Because of the band nature, the electrons move to the lowest energy positions, where then the recombination occurs. As such, the emitted photon energy is sharply centered around the difference between the two bands. The band-band recombination should not strongly depend on temperature, if no defects are present that can act as traps. If traps are present, the band-band recombination decreases with temperature due to the lower availability of free charge carriers. The emitted photons of the band-band recombination can change with temperature, as the band gap itself increases with lower temperatures.

Defects and impurities near the band edges can also be the starting- or end-point of radiative recombination. If two defects are involved they are called donor-acceptor pairs (DAPs), where an electron from a donor recombines with a hole in the acceptor. A free-to-bound (FB) transition can also occur between the conduction band and an acceptor or between donor and valence band. The defect-assisted radiative recombina-

tion is strongly dependent on the temperature. If the thermal energy is high enough, or the defects shallow enough to reemit the electrons or holes into the bands, this radiative recombination becomes very unlikely. In contrast to the band-band recombination DAPs can emit a broad band of energies due to their localized nature. The defects have different energy positions and electrons can not move to the lowest energy state like in a band, so that both recombination partners have varying energy positions. Lastly an exciton pair can also recombine radiatively.

Non-radiative recombination can occur via deep defect or impurity states within the band gap of the material that act as electron traps. It is also called Shockley-Read-Hall (SRH) recombination after the three researchers who modeled it as a type of non-radiative recombination (Hall 1951; Shockley and Read 1952). In this case, the electron falling into the deep defect emits its energy as a series of phonons, similar to the thermalization process (Lang et al. 1975). The opposite is also possible, that multiple phonons are absorbed by an electron to elevate it out of a deep defect. The latter process is very unlikely, as these phonons would need to have exactly the right energy and momentum. This is the reason that deep-defects are very efficient traps and increase the charge carrier recombination strongly to the point that a photovoltaic device becomes useless. It is also possible that the electrons transition into deep defects while emitting photons. This was not considered in the original SRH-model, but has been added since then (Beaucarne et al. 2003). This effect is important for an optimal IBSC, as the large optical cross-section that is needed for the IB absorption also increases the radiative recombination via these deep defects.

The second non-radiative recombination path is given by Auger recombination, where the energy of the excited electron is given to another electron instead of a photon. This second electron relaxes through thermalization so that no photon is emitted during the process. Materials with a direct band gap display a greater PL efficiency, as the lifetimes of radiative recombination paths are small. In indirect materials the necessity for phonons with the right momentum decrease the chance of a radiative recombination which increases the life-time of the free charge carriers and the chance for non-radiative recombinations to occur.

Experimental setup

Single photon experiment   The photoluminescence experiments were conducted by Dr. Vadim Talalaev on a custom optical setup belonging to the Innovation Center SiliNano of Prof. Dr. Jörg Schilling. The samples are placed in a *KONTI-Cryostat 4* from *CryoVac*, allowing for continuous flow liquid helium cooling to about 7 K. The samples are illuminated with a 405 nm laser diode from *Thorlabs* with an effective energy flux of $20 \, \mathrm{mW \, cm^{-2}}$ on the sample. The photoluminescence spectrum is scanned with a *SpectraPro 2550* monochromator from *Princeton Instruments* with a $150 \, \mathrm{mm^{-1}}$ grating, 800 nm blaze, 2 mm slit and a spectral resolution of 20 nm. A *Spec-10* CCD detector from *Princeton Instruments* is used for intensity accumulation. Different filters in the beam path ensure a clean laser and PL spectrum. A *BG23* band-pass filter from *SCHOTT* is set in front of the sample to isolate the 405 nm peak of the laser diode. A combination of *KG5* (*SCHOTT*), *OG550* (*SCHOTT*) and *FF02-409* (*Semrock*) long-pass filters are placed in front of the monochromator to cut off the laser wavelength, leaving mainly the PL-spectrum from the sample.

Two-photon experiment   The two-photon experiment is conducted on the same setup, swapping one laser for two lower energy ones. A 820 nm laser diode from *Thorlabs* with $40 \, \mathrm{mW \, cm^{-2}}$ on the sample is used as a continuous wave pump laser. A 1625 nm laser diode from *Thorlabs* with $80 \, \mathrm{mW \, cm^{-2}}$ is used with an alternating current as the probe laser (resulting in an effective energy flux of $40 \, \mathrm{mW \, cm^{-2}}$ on the sample). The detector is switched to a *PMT H7844* from *Hamamatsu* with a maximum sensitivity around 400 nm. This is connected to a lock-in amplifier, which only amplifies the part of the signal that is generated together with the 1625 nm probe laser. In this case, two filters are placed in the respective beam paths in front of the sample. A *BG3* band-pass filter from *SCHOTT* for the 820 nm laser and a *BBP-1430-1770* band-pass filter from *Spectrogon* for the 1625 nm laser. The samples for PL have been grown on the same Borofloat from *SCHOTT* as the other samples. To eliminate interference in the measured spectrum the middle of the glass substrate was roughened by laser ablation. Because of the limited amount of liquid helium, only three samples were measured at temperatures below 10 K. A reference sample, a V doped sample with 3.9 at.% and a Nb doped sample with 2.9 at.%. One additional V doped sample

with $0.5\,\mathrm{at.\%}$ was measured in the two-photon experiment to verify the results.

Analysis method

The analysis was conducted in cooperation with Dr. Vadim Talalaev using *OriginPro*.

An Arrhenius analysis can be performed on the temperature dependent PL spectra to calculate the activation energies of the transitions. The Arrhenius equation for one defect is given by:

$$I(T) = \frac{I_0}{1 + N \exp\left(-\frac{E_A}{k_B T}\right)} \tag{4.43}$$

with the temperature T, temperature dependent integrated PL intensity $I(T)$, the integrated intensity at $T = 0\,\mathrm{K}$ I_0, the coefficient $N = \frac{\tau_R}{\tau_0}$,the activation energy E_A and Boltzmann's constant k_B. N depends on the radiative lifetime of carriers τ_R and the non-radiative lifetime of the defect τ_0.

This equation can be expanded to include two defects (Fang et al. 2015):

$$I(T) = \frac{I_0}{1 + N_1 \exp\left(-\frac{E_{A1}}{k_B T}\right) + N_2 \exp\left(-\frac{E_{A2}}{k_B T}\right)} \tag{4.44}$$

The temperature dependency of the integrated intensity $I(T)$ is fitted with this equation to obtain E_{A1}, E_{A2}, N_1 and N_2.

4.11   Photoelectron spectroscopy

Method fundamentals

Photoelectron spectroscopy utilizes the energy of photoelectrons to get various information about a sample, depending on the used photon energy. By using high energy photons (UVs or X-rays) the sample's electrons are excited strongly enough to be able to leave the sample. The energy and amount of the electrons is then measured using a combination of an electron energy analyzer and an electron detector. A vacuum chamber is needed to avoid scattering of the electrons with air. Photoelectron spectroscopy is very surface sensitive, as the electrons have to escape the sample before

interacting with the material through e.g. scattering or recombination. The measurement depth is usually in the range of a few nanometers. As such the sample handling is very important to avoid air exposure and surface contamination.

In X-ray Photoelectron Spectroscopy (XPS) electrons are separated from their atoms using X-rays. The X-ray source can be a laboratory source or a synchrotron beam. X-rays have enough energy E_{ph} to remove core electrons from the atoms. The kinetic energy E_{kin} of these photoelectrons then depends on E_{ph}, the binding energy E_{bind} of the electrons to the atoms and allows the calculation of the binding energy:

$$E_{bind} = E_{ph} - E_{kin} \tag{4.45}$$

Binding energies are characteristic to elements and also depend on neighboring atoms. As a result XPS allows the identification of elements contained in a sample as well as their chemical state.

When using lower energy UV photons, the method is named Ultra-violet Photoelectron Spectroscopy (UPS). In this technique the photons with energy E_{ph} separate the valence electrons from the atoms, resulting in photoelectrons with kinetic energy E_{kin} dependent on the ionization energy E_{ion}:

$$E_{ion} = E_{ph} - E_{kin} \tag{4.46}$$

The resulting photoelectron energy contains information about the electron filled part of the electron band structure. Since electrons need to be present, only the filled parts of the band structure can be detected. Therefore, the Fermi-level on the sample's surface can be derived.

Experimental setup

The samples for XPS and UPS were grown on FTO to have a conductive substrate needed for the experiment. The samples are not directly exposed to air during the transfer from the preparation chamber to the measurement setup. This is achieved by wrapping the front of the preparation chamber in a glovebag. The glovebag is then repeatedly vented with nitrogen to remove as much air as possible. The chamber is then also vented with nitrogen. In this nitrogen atmosphere each sample is put in a

container and consecutively vacuum sealed in two plastic bags, the outer one coated with aluminum to be airtight. At the measurement setup the samples are opened in an argon-filled glovebox that is directly connected to the ultra-high vacuum system used for the measurements.

XPS and UPS measurements were conducted by Dr. Dirk Hauschild on devices belonging to the Applied Spectroscopy and Materials Group of Prof. Dr. Clemens Heske at the Karlsruhe Institute of Technology.

The samples' surface can be cleaned with an argon ion beam from a *Focus FDG 150*. The analysis chamber contains a *DAR 450* twin anode for the generation of Mg und Al K_α X-rays. A gas discharge lamp is used to generate UV-photons using He I and He II emission lines. The photoelectrons are detected using a *Scienta Omicron Arcus CU* analyzer.

Analysis method

The analysis of the XPS spectra is done in *OriginPro* in cooperation with Dr. Dirk Hauschild. The modified Auger parameter of indium α'_{In} is calculated by adding the kinetic energy of the In MNN Auger peak E^{kin}_{InMNN} and the binding energy of the In 3d peak E^{bind}_{In3d}:

$$\alpha'_{In} = E^{kin}_{InMNN} + E^{bind}_{In3d} \tag{4.47}$$

This approach eliminates any charging effects of the surface, which improves comparability between samples. Due to the difficulty of fitting the Auger peaks, both E^{kin}_{InMNN} and E^{bind}_{In3d} are determined visually. The resulting error for α'_{In} is estimated from the reading inaccuracy of both peak positions.

The more extensive analysis of V 2p includes fitting the XPS peaks of V $2p_{3/2}$ and V $2p_{1/2}$. First the O 1s satellite peaks are removed by subtracting the known intensity from the spectrum, then the background is fit by a linear function. The peaks themselves are fit with Voigt profiles, except for the V-V peak at $512.3\,\text{eV}$, which required the use of a split Voigt profile. The same profile shapes and relative spacing were used for both V 2p species. The analysis of the UPS spectra is done in *OriginPro* by Dr. Dirk Hauschild.

4.12   Profilometry

Method fundamentals

A profilometer consists of a stylus with a diamond tip which is dragged over the surface of a sample with a defined downforce. The vertical displacement of the tip is recorded and can be used to analyze the height of features, the thickness of layers and the roughness of the surface of a sample in the nm to mm range.

Experimental setup

The *Ambios Technology XP-1* profilometer belonging to the Polymer Physics Group of Prof. Dr. Thomas Thurn-Albrecht with its supplied software is used to measure the thickness of samples. A $1\,\mu m$ standard is used to calibrate the setup before a measurement series. All measurements were done with a speed of $0.05\,\mathrm{mm\,s^{-1}}$, over a length of $0.5\,\mathrm{mm}$, with a vertical range of $10\,\mu m$ and a force of $10\,\mathrm{mg}$.

Analysis method

The thickness of the samples in the center of the sample holder was measured three times at different positions on the same edge of the sample. The substrate holder shadows the glass during deposition, creating a good edge to measure the deposited thickness. The thickness is taken as the average of these three measurements. From earlier tests it is known that the height on all edges is the same within the error margins. Because of the laser-light scattering used to control the thickness during the deposition, the rough thickness is known for a sample and fits the measured thickness of the center sample to about 100 to $200\,\mathrm{nm}$. From multiple measurements the error is estimated to be in the range of $10\,\%$ relative. The outer samples of a preparation run have a thickness gradient, so only the center samples are used for analysis and the thickness variation is within the above-mentioned uncertainty.

Chapter 5

Transition metal incorporation into the structure of In$_2$S$_3$

Working with hyper-doped materials ($>1 \times 10^{20}$ cm^{-3} doping density), which are needed for the deep level impurity bands (see chapter 2.3), strongly effects the host lattice. For example high defect densities can increase the SRH recombination, clusters of the doping material or secondary phases can lower the mobility or create short circuits and crystal lattice changes can alter the desired band gap energy (see chapters 2.1.1 and 2.2). It is therefore important to analyze the structure changes from incorporating the transition metals V, Ti and Nb into the In$_2$S$_3$ host lattice to confirm the complete incorporation and check for secondary phases.

5.1 Crystal morphology and texture

The grain size and texture of samples with different transition metal doping and substrate temperatures are analyzed as indicators of structural defects. Only samples grown on Borofloat glass are analyzed in this section.

5.1.1 Crystal morphology

The topography of the samples and morphology of the crystals was measured with surface and cross-section scanning electron microscopy (SEM) (see chapter 4.1 for details). Figures 5.1 to 5.5 display comparisons of surface SE-images of the various samples se-

ries. The pure In_2S_3 at $500\,°C$ (**InS-1**) shown in 5.1 on the left grows into highly ordered hexagonal (nearly triangular) crystals of up to more than $1\,\mu m$ in width. Three sides of the hexagons are longer, forming triangular shapes. The easier to measure angles of the surface triangles (angles between the longer sides of the hexagon) on sample **InS-1** yields angles in the range of $50°$ to $70°$ with an average $60°$ and standard deviation of $5°$. There is no detected system to the angle variation that could be interpreted. As shown in the next section 5.1.2 the surface faces are tetragonal $1\,0\,3$ (cubic $1\,1\,1$-equivalent) faces, where this crystal shape can be expected (Huang et al. 2017; Lu, Zheng, et al. 2019; McCarthy, Weimer, Emery, et al. 2014). It is noticeable that crystallites seem to fuse into one another, making it sometimes difficult to determine the crystal boundaries. The vanadium concentration variation is also displayed in figure 5.1 ranging from sample **InSV-0.9** to **InSV-5.3**. **InSV-0.9** still has large crystals, but they are not perfectly flat and hexagonal anymore. The same is true for the other doping concentrations, where additional smaller crystallites grow on top of the larger crystals. There are still large crystals present, despite high doping concentrations, but the visible shape of the larger crystallites is not discernible anymore. The temperature variations of all three dopants (figures 5.2 to 5.5) show a trend of decreasing crystal size with decreasing temperature. Additionally, the large crystals that are present in samples grown at $500\,°C$ are less visible in $400\,°C$ samples and vanish in samples grown at $300\,°C$. This effect is independent of the dopant.
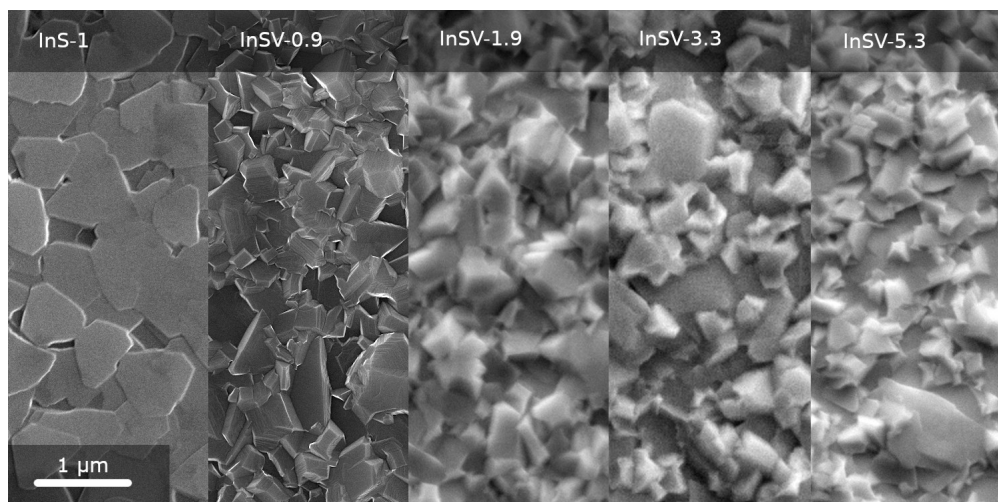
Figure 5.1: *SE images of the vanadium concentration variation.*
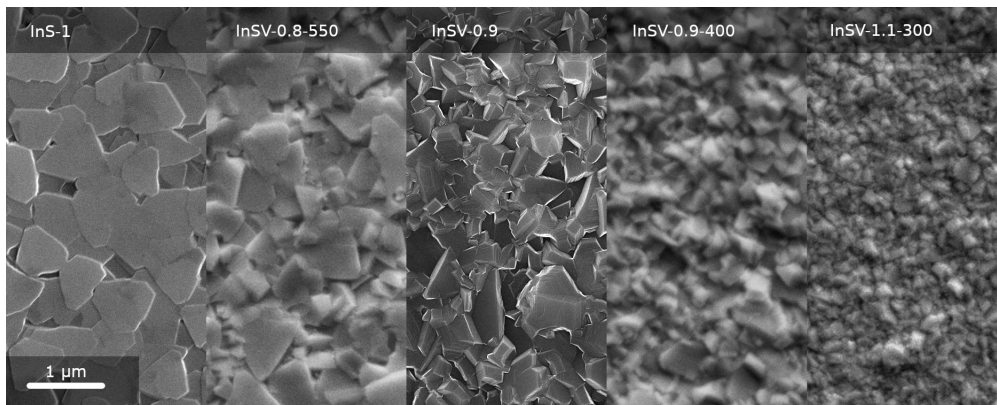
Figure 5.2: *SE images of the* $1\,at.\%$ *V substrate temperature variation.*
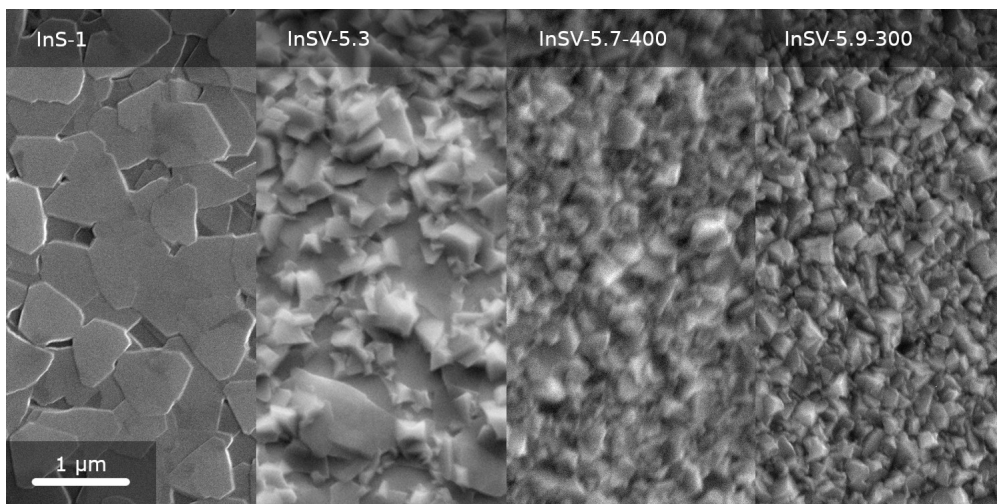
Figure 5.3: *SE images of the* $5\,at.\%$ *V substrate temperature variation.*

Using these images, it is possible to estimate the mean crystallite size of each sample. The crystals in the bulk might be slightly larger, as there are more of the smaller crystals on the sample's surface (see cross-section in fig. 5.12). By taking into account the standard deviation and maximum values a reasonable comparison between the samples is possible. Table 5.1 lists all samples with the corresponding mean crystallite sizes, the standard deviation as well as the minimum and maximum values.

Figure 5.6 compares the surface crystallite sizes of the pure In_2S_3 to In_2S_3:V samples grown at $500\,°C$ with different doping concentrations. The V-doping reduces the mean crystallite size from about $0.7\,\mu m$ to around $0.5\,\mu m$. The exact doping concentration does not seem to matter, as the mean values with the standard deviation stay in the
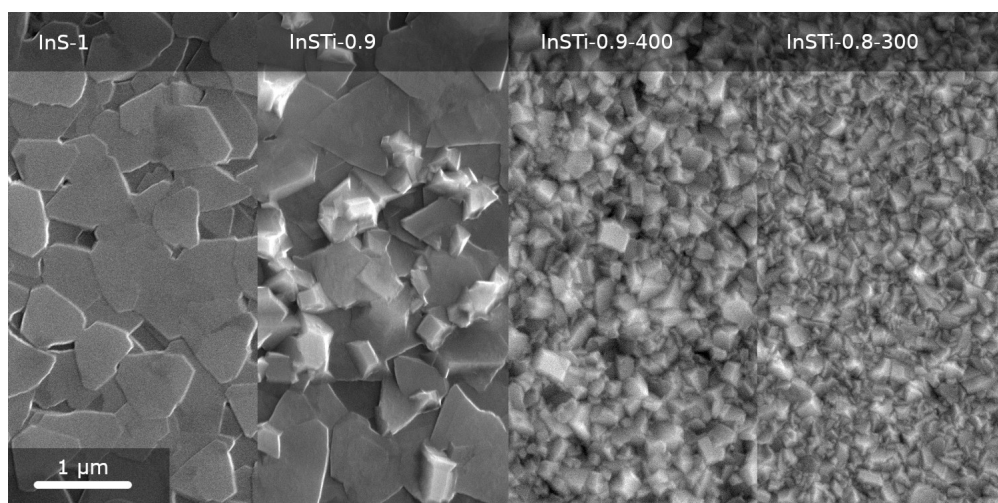
Figure 5.4: *SE images of the* $1\,\mathrm{at.\%}$ *Ti substrate temperature variation.*
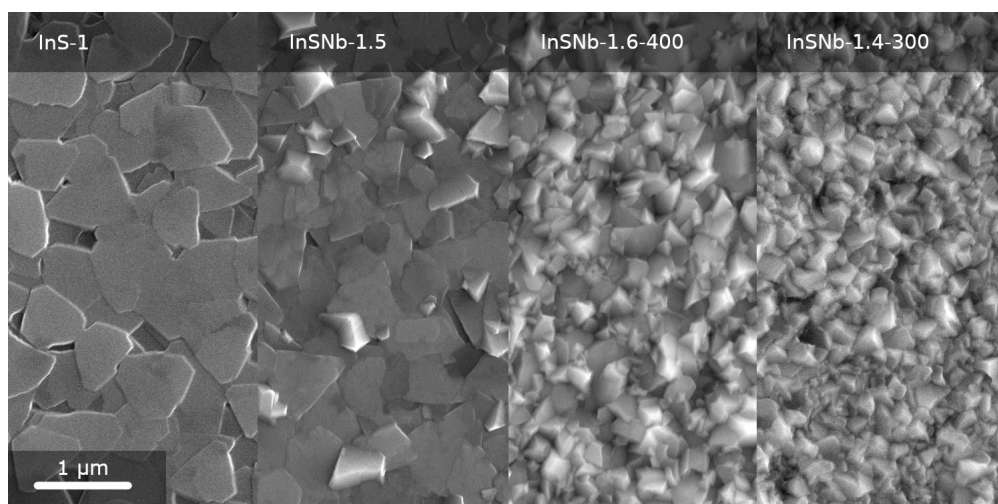
Figure 5.5: *SE images of the* $1\,\mathrm{at.\%}$ *Nb substrate temperature variation.*

same region. All samples regardless of doping, have larger crystallites with a size of $1\,\mu\mathrm{m}$ and above, but the doping increases the amount of smaller crystallites. Compared to the large standard deviation, the decrease in surface crystallite size from doping is small.

The dependence of the surface crystallite sizes on the growth temperature is shown in figures 5.7 to 5.10. As already seen in the SEM images the crystals grown at $500\,°\mathrm{C}$ are larger than the ones grown at $400\,°\mathrm{C}$ or $300\,°\mathrm{C}$. The $500\,°\mathrm{C}$ samples all have a mean crystal size of about $0.5\,\mu\mathrm{m}$ and higher, the $400\,°\mathrm{C}$ samples around $0.3\,\mu\mathrm{m}$ and

Table 5.1: *Crystallite sizes determined from top-down SE images.*

Sample	Crystallites measured	Mean (μm)	Std. Dev. (μm)	Min. (μm)	Max. (μm)
InS-1	49	0.70	0.18	0.39	1.18
InS-2	66	0.73	0.19	0.18	1.26
InSV-0.8-550	117	0.54	0.27	0.14	1.44
InSV-0.9	54	0.43	0.19	0.19	0.91
InSV-1.98	75	0.46	0.15	0.20	0.97
InSV-3.3	80	0.51	0.24	0.18	1.36
InSV-5.3	47	0.50	0.21	0.21	1.23
InSV-0.9-400	74	0.32	0.10	0.16	0.63
InSV-5.7-400	64	0.30	0.10	0.14	0.66
InSV-1.1-300	103	0.15	0.06	0.06	0.32
InSV-5.9-300	70	0.22	0.09	0.06	0.47
InSTi-0.9	48	0.92	0.34	0.29	1.44
InSTi-2.1	55	0.57	0.18	0.19	0.86
InSTi-0.9-400	76	0.26	0.10	0.07	0.54
InSTi-4.2-400	129	0.26	0.09	0.11	0.61
InSTi-0.8-300	135	0.17	0.07	0.05	0.36
InSNb-0.5	134	0.49	0.26	0.15	1.25
InSNb-1.5	39	0.57	0.26	0.18	1.05
InSNb-1.6-400	95	0.27	0.11	0.08	0.58
InSNb-1.4-300	112	0.21	0.08	0.08	0.47
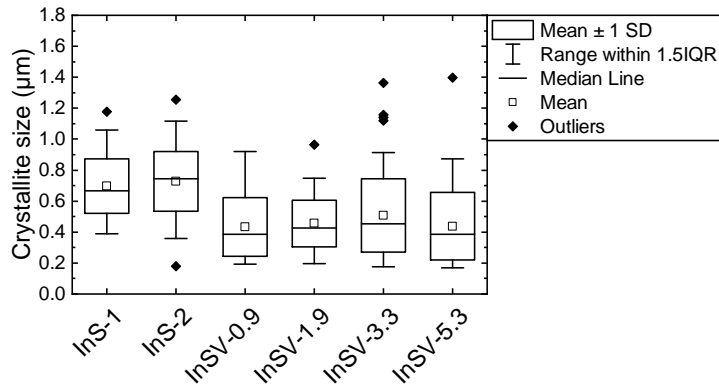
Figure 5.6: *Comparison of surface crystallite sizes with V doping concentration.*

the $300\,°C$ around $0.2\,\mu m$. The change from doping with Ti and Nb is similar to V, except for the $1\,at.\%$ Ti sample grown at $500\,°C$. This anomalous sample contains a lot of large crystallites and very few small ones. One reason might be the area on the sample where the crystallites are measured, as some areas have a larger amount of small crystals growing on top. The other reason might be an unidentified change in the growth conditions that resulted in larger crystals, but the preparation data do not hint to any changes in the process.
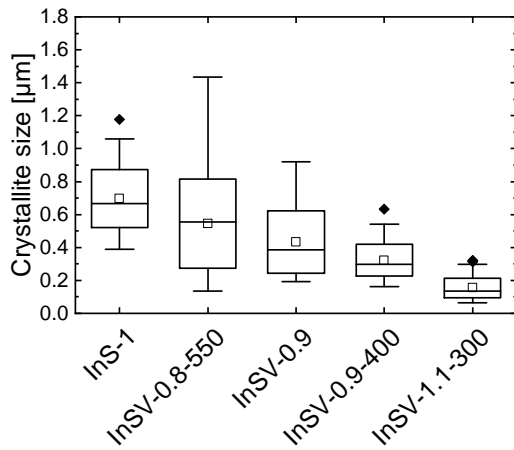
Figure 5.7: *Surface crystallite sizes of the ∼1 at.% V-doped samples.*
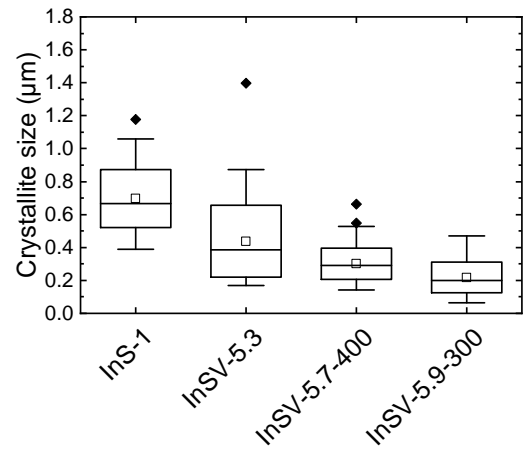
Figure 5.8: *Surface crystallite sizes of the ∼5 at.% V-doped samples.*
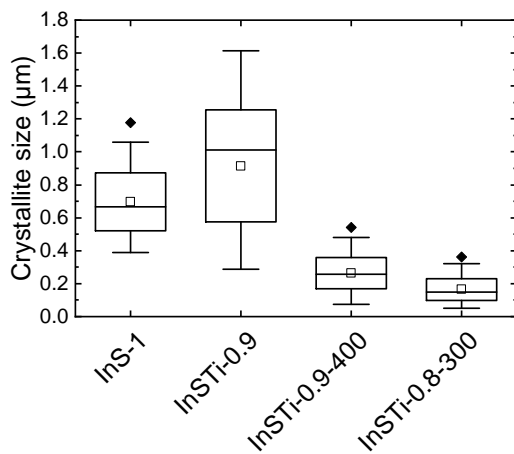
Figure 5.9: *Surface crystallite sizes of the ∼1 at.% Ti-doped samples.*
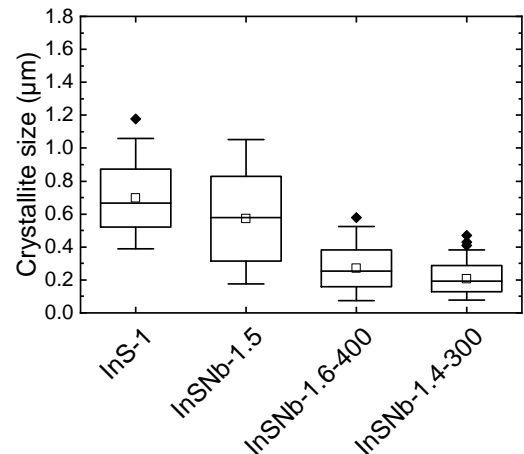
Figure 5.10: *Surface crystallite sizes of the ∼1 at.% Nb-doped samples.*

One thing that has to be kept in mind is that the samples are grown at different rates, due to the limitations of the electron beam source. Figure 5.11 shows the mean surface crystal size versus the crystal growth rate of the various samples. It visualizes that the growth rate is not the limiting factor of the crystal size, but rather the temperature during growth.
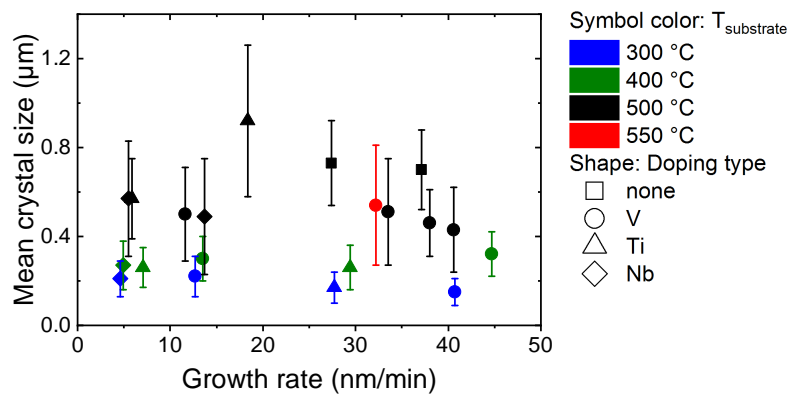
Figure 5.11: *Mean crystal size t versus the growth rate of the samples. The growth rate does not impact the crystal sizes.*

A few samples were mechanically broken in half and imaged edge on, to estimate the bulk crystal shapes and sizes. The SE images displayed in fig. 5.12 do not show very clear crystallite boundaries. As is visible on the top-down images (e.g. fig. 5.10), the crystals tend to grow into one another. This is true even for the sample grown at 300 °C. It is possible to see some crystallites, but they are difficult to separate clearly. As such, the crystallite sizes cannot be reliably measured, but appear to have similar size as seen from the surface. Some distinguishable larger crystals in the undoped sample seem to have a pyramid-like shape, growing in various directions and extending over the whole thickness of the layer. Between these larger crystals are smaller ones, similar to the top-down images. For the doped samples, the pyramid structure of the larger crystals is not as pronounced, as was already seen in the top-down images.

The surface crystallites can now be interpreted as faces and tips of these triangular pyramid-like structures, with smaller crystals growing between them throughout the bulk of the material. With higher doping, there are more of the smaller crystallites and with lower temperatures the large thickness-spanning crystals start to disappear. Other researchers also reported triangular (Huang et al. 2017; Lu, Zheng, et al. 2019;
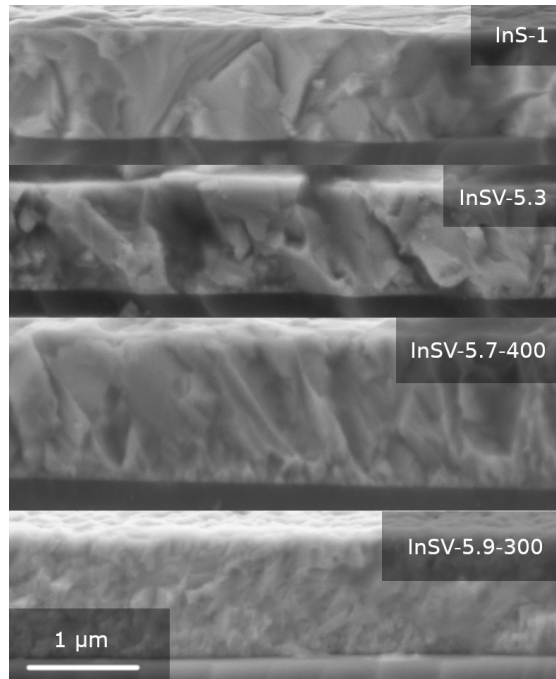
Figure 5.12: *Comparison of bulk crystals of a pure In_2S_3 and the $5\,at.\%$ V doped temperature series.*

McCarthy, Weimer, Emery, et al. 2014) and pyramid-like growth (Feng et al. 2017).

The conclusion is that a higher growth temperature like $500\,°C$ is preferable to get larger crystallites. On the amorphous glass substrates, which do not force any lattice preference on the crystals, hexagonal (nearly triangular) pyramid structures grow that extend through the whole In_2S_3 layer. Hyper-doping with larger concentrations of transition metals alters this behavior, as the shape is no long clearly hexagonal/triangular. The doping also increases the amount of smaller and more random crystallites in the samples.

5.1.2   Texture

The texture of a sample describes the relative number of crystallites in a sample that are oriented in the same direction. A powder is non-textured, while a single crystal is $100\,\%$ textured. In poly-crystalline thin-film samples there are often preferred crystal orientations depending on growth parameters and substrates resulting in certain textures. XRD and GIWAXS are used to qualitatively analyze the texture (see sections 4.3

and 4.4 for details).

Figures 5.13 and 5.14 display the XRD diffractogram measured from sample **InS-1** with a linear and logarithmic scale. The good crystallinity and large crystals allow the bremsstrahlung and the nickel Kβ-filter edge to be visible for the main peaks when using a logarithmic scale. Additional spikes caused by the aging detector are smoothed out as much as possible during the analysis without changing the actual reflex shapes.
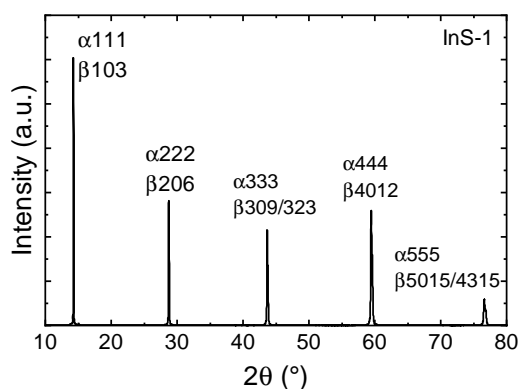
Figure 5.13: *Diffractogram of sample **InS-1**. A strong 1 1 1 texture is apparent.*
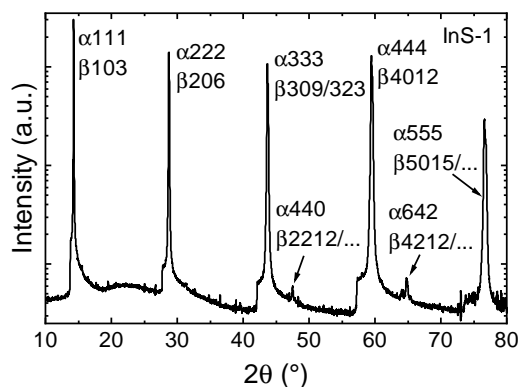
Figure 5.14: *Logarithmic diffractogram of sample **InS-1**. Bremsstrahlung, nickel filter edge and smaller peaks become visible.*

Assigning Miller indices can be done by comparing the measured diffractograms with literature data. In$_2$S$_3$ can be present in the tetragonal β-phase and the cubic α-phase which are very similar and difficult to distinguish (see section 2.4). The α-In$_2$S$_3$ phase is not stable at room temperature for the correct In$_2$S$_3$ stoichiometry of $60\,\mathrm{at.\%}$ S (Goedecke et al. 1985). To get a diffractogram of α-In$_2$S$_3$ with the correct stoichiometry the structure data have to be obtained above the phase transition temperature. PDF#00-067-0787 for α-In$_2$S$_3$ and PDF#00-067-0786 for β-In$_2$S$_3$ were chosen from the *ICDD PDF-4+* XRD-database as the references as they are both based on the same preparation experiment by Pistor et al. (2016) who correctly measured α-In$_2$S$_3$ at $475\,^{\circ}\mathrm{C}$. But as a result of the unavoidable higher temperature, the reflexes are shifted for the α-In$_2$S$_3$ reference. β-In$_2$S$_3$ and α-In$_2$S$_3$ are structurally very similar (see section 2.4), so the high intense reflexes are present in both making it difficult to distinguish them. We will later see that sample **InS-1** is in the tetragonal β-phase (see section 5.2.1). Nevertheless, both *hkl* values will be noted. Because we do not know the exact planes of e.g. the $\{1\,1\,1\}$ plane group which contribute to the diffractogram, we write the *hkl* values without

any brackets and mean any number of the corresponding planes. The Greek letters denote that the Miller indices correspond to the α- or β-phase, respectively.

It has to be noted, that some Miller index assignments differ from reference to reference. Given the complex structure of In_2S_3 and the fact that most references are measured as powders, it is difficult to assign the "correct" Miller indices. In this case, because of the $\alpha 1\,1\,1/\beta 1\,0\,3$ texture of the material it was clear that the peak at $76.4°$ should have the main Miller indices of $\alpha 5\,5\,5/\beta 5\,0\,15$ and not e.g. $\alpha 7\,5\,1/\beta 4\,3\,15$. It is still possible that other planes with the same distance contribute to these peaks, but we will use the assignments from the references PDF#00-067-0787 for α-In_2S_3 and PDF#00-067-0786 for β-In_2S_3. Only the tetragonal $4\,3\,15$ planes in this reference differ from the $5\,0\,15$ planes expected here. As such, both are noted as planes contributing to the $76.4°$ peak. In our publication (Wägele et al. 2017), we mistakingly assigned $\alpha 5\,1\,1$ to the $\alpha 3\,3\,3$ reflex, because of the different references used.
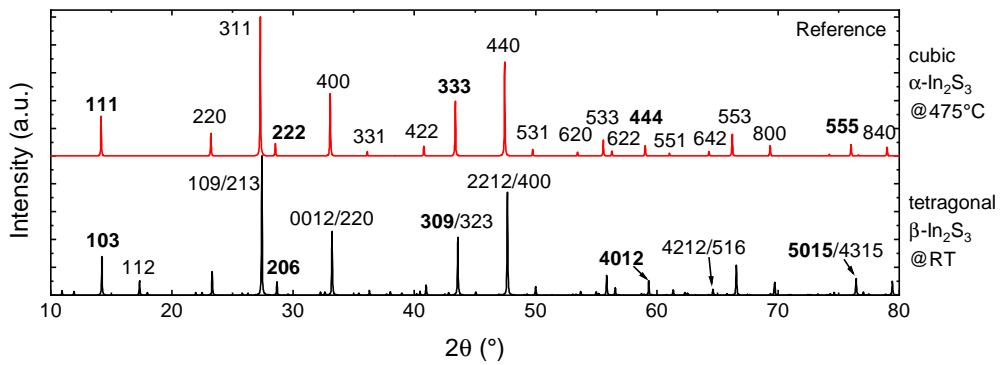
Figure 5.15: *Reference diffractograms of powder α-In_2S_3 and β-In_2S_3 with no texture. They are calculated from experimental structure data from ICDD PDF#00-067-0787 for α-In_2S_3 and PDF#00-067-0786 for β-In_2S_3 published by Pistor et al. (2016).*

Figure 5.15 displays the above-mentioned calculated reference diffractograms expected for a non-textured powder with hkl labels for α-In_2S_3 reflexes and a few select labels for the myriad of β-In_2S_3 peaks.

The reflexes of the cubic α-phase have practically the same intensity ratios between the different peaks as the β-phase. In fact the β-In_2S_3 diffractogram is nearly the same as the α-In_2S_3 diffractogram with a lot of smaller peaks added due to the additional symmetry of the In vacancy ordering (see section 2.4). In praxis the two are indistinguishable if the additional peaks from the β-phase (noteably $1\,1\,2$) are not visible. For

the texture determination it does therefore not matter if our sample is in fact perfectly in the α- or β-phase. If not otherwise noted, we will therefore use the cubic notation, so that e.g. $1\,1\,1$ stands for peaks of both $\alpha 1\,1\,1 / \beta 1\,0\,3$.
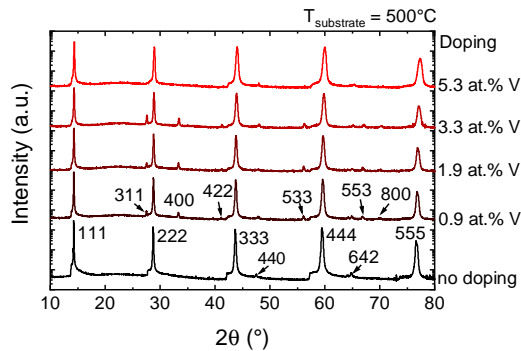
Figure 5.16: *Diffractograms of the In_2S_3:V concentration series from top to bottom: Samples **InSV-5.3**, **InSV-3.3**, **InSV-1.9**, **InSV-0.9** and **InS-1**. The strong $1\,1\,1$ texture is present in all samples, with slight non-systematic changes. The diffractogram intensities are shifted to increase visibility.*

The comparison between the randomly oriented powder references and sample **InS-1** shows that this sample has a very strong $1\,1\,1$ texture. The different sample series are displayed in log-scale in figures 5.16 to 5.20. Most samples have a similar $1\,1\,1$ texture as **InS-1**. The only exception are samples grown at $300\,°C$, which display much lower XRD intensities and a more random crystal orientation, but still with a bias for the group of $1\,1\,1$-parallel planes. In most cases the $400\,°C$ samples have a marginally weaker texture than the ones grown at $500\,°C$. As with the crystallite sizes, the transition metal doping does not seem to effect the texture very much.

To complement the XRD measurements it is useful to use GIWAXS, as it allows the detection of the reciprocal space in other directions than the θ-2θ scans shown until now. This technique is described in detail in chapter 4.4. Figure 5.21 displays the GIWAXS measurement for sample **InS-1**. The empty spaces result from the gaps between the detectors and the fact that it is not possible to detect most of what would be diffracted along the q_z axis (see section 4.4). The single planes can be seen as nearly point-like in this slice of the reciprocal space, as would be expected for a single crystal.
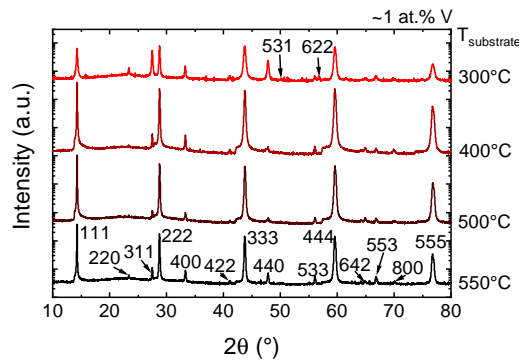
Figure 5.17: *Diffractograms of the* $1\,\mathrm{at.\%}$ *In_2S_3:V temperature series from top to bottom: Samples* **InSV-1.1-300, InSV-0.9-400, InSV-0.9** *and* **InSV-0.8-550**. *Only the sample grown at* $300\,°\mathrm{C}$ *is significantly different with a lower intensity and different intensity ratios. The diffractogram intensities are shifted to increase visability.*
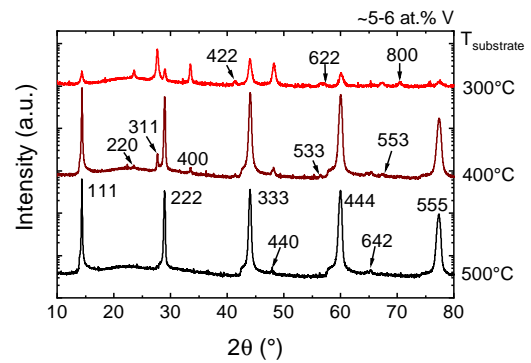
Figure 5.18: *Diffractograms of the* $5\,\mathrm{at.\%}$ *In_2S_3:V temperature series from top to bottom: Samples* **InSV-5.9-300, InSV-5.7-400** *and* **InSV-5.3**. *Only the sample grown at* $300\,°\mathrm{C}$ *is significantly different with a lower intensity and different texture. The diffractogram intensities are shifted to increase visibility.*
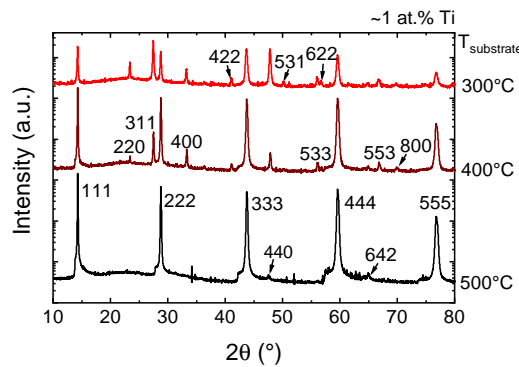
Figure 5.19: *Diffractograms of the* $1\,\mathrm{at.\%}$ *In_2S_3:Ti temperature series from top to bottom: Samples* **InSTi-0.8-300, InSTi-0.9-400** *and* **InSTi-0.9**. *The sample grown at* $300\,°\mathrm{C}$ *is significantly different with a lower intensity and different texture. The* $400\,°\mathrm{C}$ *sample has a weaker texture than the* $500\,°\mathrm{C}$ *sample. The diffractogram intensities are shifted to increase visibility.*
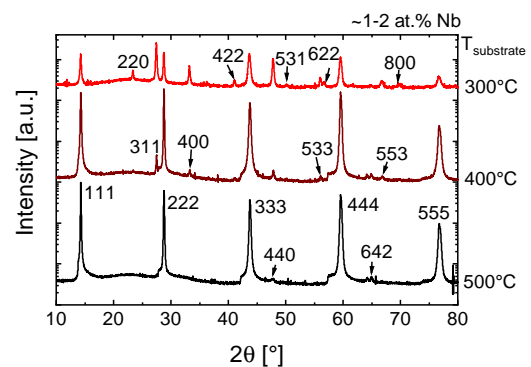
Figure 5.20: *Diffractograms of the* $1\,\mathrm{at.\%}$ *In_2S_3:Nb temperature series from top to bottom: Samples* **InSNb-1.4-300, InSNb-1.6-400** *and* **InSNb-1.5**. *The sample grown at* $300\,°\mathrm{C}$ *is significantly different with a lower intensity and different texture. The diffractogram intensities are shifted to increase visibility.*

We do know from SEM that the sample is definitely poly-crystalline. Rotating the sample on the holder by 30° results in the same image which indicates that the crystals

grow perpendicular to the 1 1 1-based planes with a random rotation distribution. This is consistent with the SEM images.
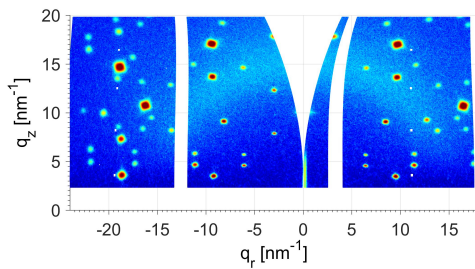
Figure 5.21: *GIWAXS graph of the sample **InS-1** in q-space taking the Ewald sphere curvature into account. The reflexes show up as near perfect circles, meaning that nearly all crystallites are growing with a 1 1 1 orientation on the glass substrate.*
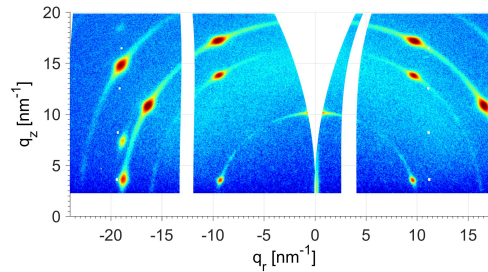
Figure 5.22: *GIWAXS graph of the sample **InSV-5.3**. The reflexes show up as ovals, meaning that most crystallites grow with a 1 1 1 orientation on the glass substrate with slight deviations in other directions. A few crystals are randomly oriented, creating weak Debye-Scherrer rings in the diffractogram.*
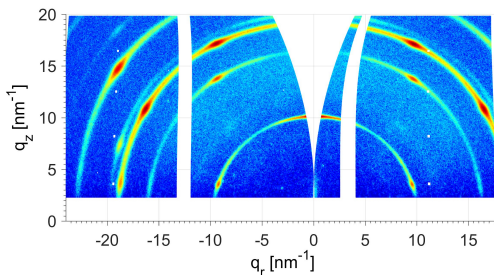
Figure 5.23: *GIWAXS graph of the sample **InSV-0.9**. The main reflexes diffuse into rings: The 1 1 1 texture is not as strong, allowing for more randomly oriented crystals to diffract into Debye-Scherrer rings.*
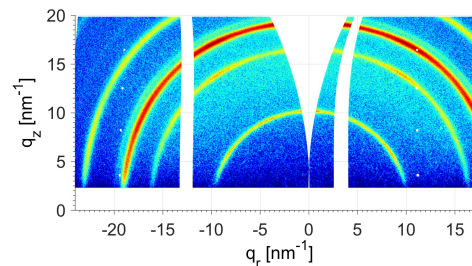
Figure 5.24: *GIWAXS graph of the sample **InSV-5.9-300**. The 1 1 1 texture is nearly gone. Most crystals are randomly oriented, but still gravitating towards the preferred 1 1 1 texture.*

Other samples do not have this near perfect texture as shown in figures 5.23 to 5.24. They represent the three different texture categories observed, excluding the near perfectly textured sample **InS-1**. Firstly samples that show a strong 1 1 1 texture, with a few randomly oriented crystallites (fig. 5.22), secondly samples with a less strong 1 1 1 texture, where the diffraction maxima are more or less diffusing into Debye-Scherrer rings (fig. 5.23) and lastly samples which show weak 1 1 1 textures (fig. 5.24). Table 5.2

displays which sample falls into which category and compares these to the observed
surface topography and the texture coefficient calculated below. The substrate tem-
perature of $300\,°C$ has again the strongest effect, while the doping concentration does
seem to hinder the near perfect texture, but no real trend is visible.

To better quantify the influences on the texture it is possible to calculate a semi-
quantitative texture coefficient t from XRD by using the Harris method introduced in
chapter 4.3. It compares the intensity of each reflex to the expected intensity with no
texture and norms it with the mean over all reflexes. As noted by Valvoda et al. (1990)
the absolute values will be wrong for high textures. But as also stated, this is mainly
relevant for intensity corrections, which we are not interested in. As before, we focus
on the high intensity reflexes. The texture coefficient of the $1\,1\,1$ plane is reduced by
the other $1\,1\,1$ parallel planes in the measured 2θ range. A more focused range would
result in a larger t, but then many of the non $1\,1\,1$ parallel planes would be excluded
and t would incorrectly default to the number of reflexes N for most samples (see
equation 4.3). Figures 5.25 and 5.26 show the texture coefficient t of the $1\,1\,1$ reflex
for all $\sim\!1\,\mu\text{m}$ samples against the growth rate and doping concentration, respectively.
The data point shape represents the doping type, the color the growth temperature.
The growth rate does not significantly influence the texture. The doping concentra-
tion slightly decreases the texture, as already suspected from the SEM and GIWAXS
measurements. The strongest influence is the temperature which significantly reduces
the texture.
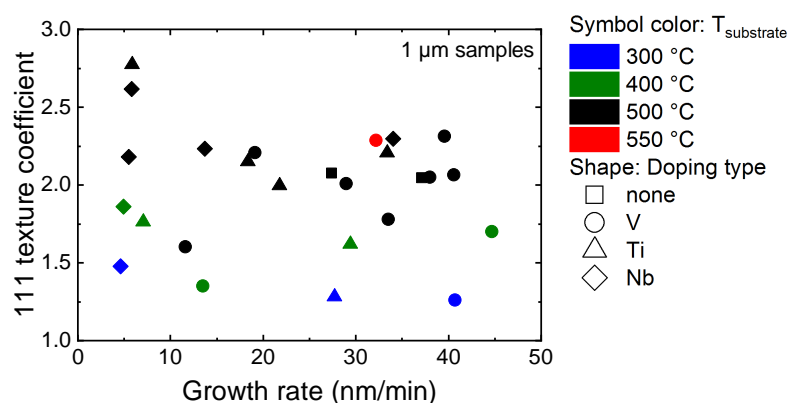
Figure 5.25: *Texture coefficient t versus the growth rate of the samples. The growth rate
does not significantly impact the texture. The substrate temperature during growth has
a larger influence on the texture.*

Table 5.2: *Texture coefficients of the 1 1 1 peak of various samples compared to GIWAXS and SEM appearance. It is noted if clear hexagonal plates are visible in SEM and how strong the texture appears from GIWAXS. There are a few discrepancies between the texture coefficient, SEM and GIWAXS. It shows that multiple measurement techniques and samples are needed to make a qualitative assessment of texture trends.*

Sample	hexagonal plates	GIWAXS texture	texture coefficient
InS-1	yes	very strong	2.04
InS-2	yes		2.08
InSV-0.1			2.01
InSV-0.5	no	weak	2.31
InSV-0.8			2.21
InSV-0.8-550	yes		2.29
InSV-0.9	yes	medium	2.06
InSV-0.9-400	no		1.70
InSV-1.1-300	no		1.26
InSV-1.9	no	medium	2.05
InSV-3.3	partly		1.78
InSV-5.3	partly	strong	1.60
InSV-5.7-400	no	strong	1.35
InSV-5.9-300	no	very weak	0.85
InSTi-0.3			1.99
InSTi-0.5			2.21
InSTi-0.9	yes	strong	2.15
InSTi-0.9-400	no		1.62
InSTi-0.8-300	no		1.28
InSTi-2.1	yes		2.77
InSTi-4.2-400	no	medium	1.76
InSNb-0.2			2.30
InSNb-0.5	yes		2.23
InSNb-1.1			2.62
InSNb-1.5	yes	strong	2.18
InSNb-1.6-400	no		1.86
InSNb-1.4-300	no		1.48
InSNb-2.9			2.16

5.1.3 Conclusion

Combining the information obtained from SEM, XRD and GIWAXS, we can say that In_2S_3 on Borofloat glass grows as strongly textured poly-crystalline layers. Some growth
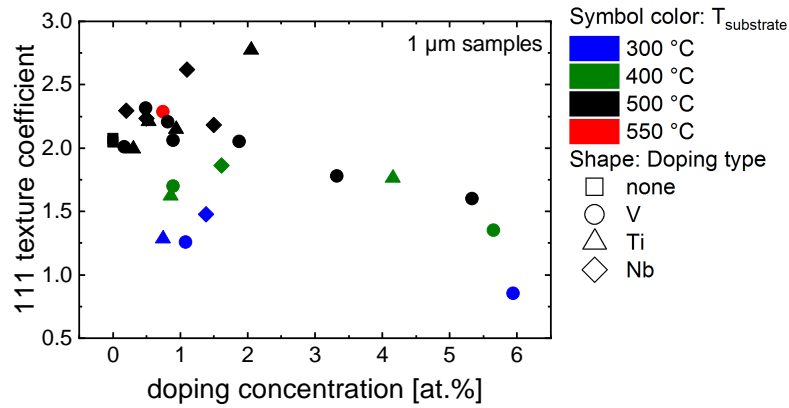
Figure 5.26: *Texture coefficient t versus the doping concentration of the samples. Higher doping concentrations slightly decrease the texture strength. The growth temperature has again a larger impact on the texture.*

directions are preferred as is typical for crystals. The growth occurs preferably perpendicular to the most stable $1\,1\,1$ plane into hexagons. Three of the six sides of the hexagonal base grow faster than the others, which leads to triangular crystal surfaces. In the cross-section SEM this growth can be seen to form (upside-down) pyramids spanning the whole material layer. The rotation distribution of the pyramids is random, as can be expected from the amorphous substrate. Similar crystal growth has been reported by other groups. For example near perfect $1\,1\,1$ triangle/pyramid layer growth can be seen in layers grown with ALD on $1\,0\,0$ silicon (McCarthy, Weimer, Emery, et al. 2014). In$_2$S$_3$ nano flakes grown by CVD on mica by Huang et al. (2017) also show perfect $1\,1\,1$ triangular crystals. Feng et al. (2017) grew In$_2$S$_3$ thin-films on FTO using hydrothermal synthesis and observed a pyramid-like growth. For lower growth temperatures the crystallites become smaller, more randomly oriented and the texture is reduced. This is expected as the mobility of the molecules on the sample's surface depends on the sample temperature. A threshold seems to be between 300 and $400\,°C$, at which point the adsorbed molecules have enough energy to settle in the existing crystals instead of forming new nuclei. The independence of the crystal size and texture from the growth rate indicates that the In-S molecule saturation on the sample surface is well-balanced. It is not too large to increase nuclei formation and not too small to decrease the crystal sizes (see chapter 2.1.1). This is true for all the growth rates that were employed to get the desired transition metal doping and validates the

comparability of samples grown with different rates. The important takeaway is that doping with transition metals influences the In_2S_3 crystal growth, but even with the highest concentrations, large crystals and high textures are achieved. For samples in the 1-2 at.% range the amount of smaller and randomly oriented crystals increases, but the bulk crystals still span the thickness of the layer and are strongly 1 1 1 textured. For higher concentrations the texture is further reduced and most crystals do not have the triangular shape anymore. This does increase the roughness of the sample's surface, but does not significantly decrease the large crystal sizes. In fact GIWAXS measurements show sample **InSV-0.9** with a weaker texture than **InSV-5.3**, indicating that other preparation parameter fluctuations have a larger impact than the hyperdoping.

5.2 Polymorphism and secondary phases

One of the main concerns when doping a material with high concentrations of another element is the formation of secondary phases. The goal is to include the elements in the given crystal structure without the element forming separate crystals with differing stoichiometries. Before we can look into this, we have to look at the doping-dependent polymorphism of the In_2S_3 itself, as it can theoretically be present in three different crystal structures.

5.2.1 Polymorphism

As described in section 2.4 the structure of In_2S_3 is based on the defect spinel and can be present in three phases: the cubic α-In_2S_3, the tetragonal β-In_2S_3 and the trigonal γ-In_2S_3. The difference between these phases comes from the ordering of the In vacancies (v_{In}) intrinsic to the defect spinel structure. With the correct stoichiometry of 60 at.% S, the only stable phase at room temperature is the β-phase, where the v_{In} are systematically ordered on the tetrahedral sites. The α-phase is stable at high temperatures of above $\sim$440 °C with disordered v_{In} on tetrahedral sites, while in the γ-phase In occupies only the octahedral sites at above $\sim$810 °C (Pistor et al. 2016). It is possible to stabilize α-In_2S_3 at room temperature when reducing the sulfur content of the crystals. A reduction to 59.5 to 59.0 at.% S seems to be enough to reduce the order of the v_{In} to a point, where the α-phase becomes stable (Goedecke et al. 1985). As such,

the presence of the β-phase is a very good indicator of a near perfect stoichiometry. It is possible to stabilize the γ-phase as well, which has been achieved by adding $5\,\mathrm{at.\%}$ of As or Sb (Diehl et al. 1976).

From the already examined diffractograms in section 5.1.2 we can directly compare the peak positions to the three references, this time also including γ-In$_2$S$_3$ (PDF#00-067-0788 @825 °C) for completeness. Figure 5.27 displays the strongly textured sample **InS-1** compared to the literature peak positions, while figure 5.28 shows the weakly textured sample **InSV-5.9-300**. A few things have to be considered here. The temperatures of the references are higher than of the samples which were measured at room temperature (20-22 °C), shifting the peaks to lower angles. When looking at the complete data published by Pistor et al. (2016) the temperature dependent measurements show that the main β-reflexes are the same as the α-reflexes. Only the difference in temperature shifts the peaks of the α-phase to lower angles. The peaks of the γ-phase are however different, as a more significant structural change occurs. The measurement data of the samples also have significant systematic errors, which result in a different shift of every peak. The main error stems from the fact that the samples are flat, as detailed in appendix A.2. The reference peak positions do not have this shift, as they are directly calculated from the structure data.
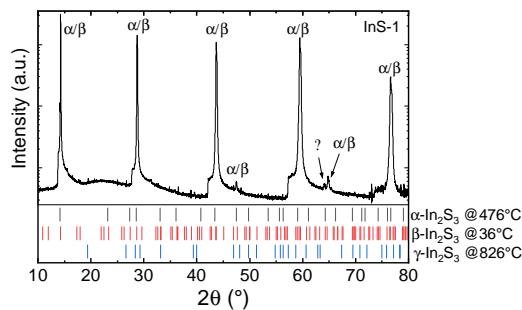
Figure 5.27: *Comparison of XRD intensities of strongly textured sample **InS-1** to the expected peak positions of the α-, β- and γ-phase.*
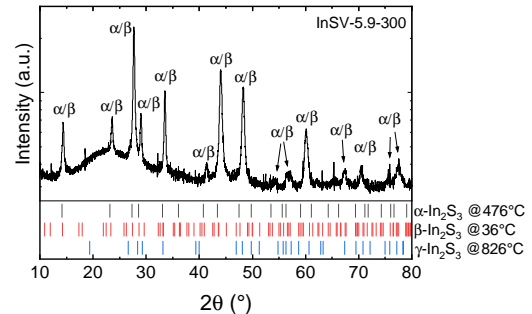
Figure 5.28: *Comparison of XRD intensities of weakly textured sample **InS-5.9-300** to the expected peak positions of the α-, β- and γ-phase.*

As can be seen in the two figures, the similarity between α-In$_2$S$_3$ and β-In$_2$S$_3$ makes it impossible to determine the phase of the In$_2$S$_3$-material of many samples solely by XRD. In this case sample **InS-1** has a very strong texture, so that most other peaks

are not detectable in the θ-2θ-scans. Sample **InSV-5.9-300** is not strongly textured, but the intensity of the reflexes is very low. This decreases the signal-to-noise ratio and makes it impossible to see any peaks with a small intensity, which most of the β-characteristic peaks have. To be able to determine the polymorphism of the samples, another method is needed. GIWAXS is useful here, as texture effects can be significantly reduced. We know already that the crystals have a random rotation distribution so that all planes not parallel to the surface should be visible. Additionally, the XRD intensity of the samples grown at $500\,°C$ is very high, so that even in the doped samples the smaller peaks of the β-phase should be visible. Figure 5.29 displays a section of the GIWAXS measurements for the V-concentration series. Marked in a red circle is the most intense β-characteristic reflex belonging to one of the tetragonal $\{1\,1\,2\}$-planes. For higher concentrations of vanadium this reflex vanishes together with the other β-reflexes, while the more intense peaks belonging to the $\alpha1\,1\,1/\beta1\,0\,3$, $\alpha2\,2\,0/\beta1\,1\,6$ and $\alpha3\,1\,1/\beta1\,0\,9$ planes remain. The same intensity reduction of the β-characteristic peaks is visible for the samples doped with Ti and Nb.
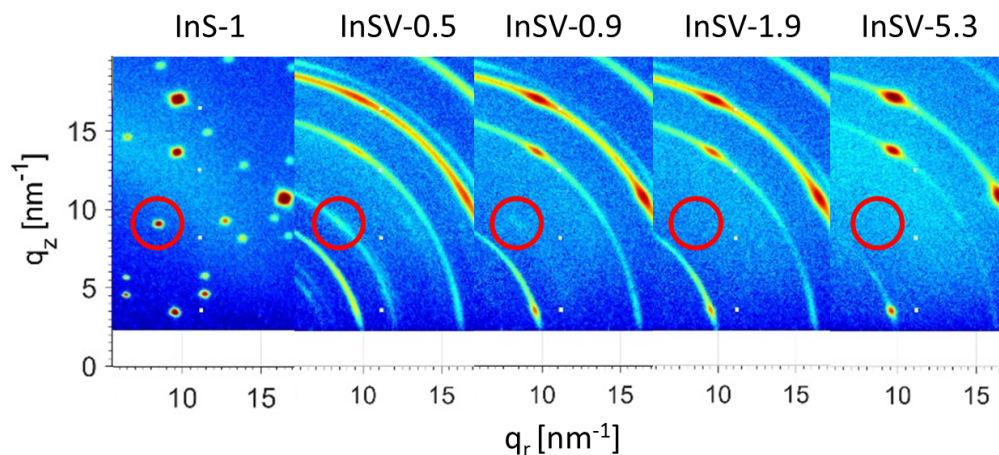
Figure 5.29: *Comparison of GIWAXS diffractograms from samples with different V-doping concentration. The β-phase characteristic reflexes vanish with higher concentrations.*

When averaging these GIWAXS measurements along the Debye-Scherrer rings ($|q_r + q_z| = $ const), it is possible to create diffractograms, which ideally should have the intensities of a powder. This is not perfectly so, as only parts of the rings are detectable. Figure 5.30 displays a comparison between sample **InS-1** to a calculated

powder diffractogram of β-In$_2$S$_3$. Sample **InS-1** is very clearly β-In$_2$S$_3$. All the expected characteristic peaks of the β-phase are detected. The averaged GIWAXS intensities match the reference very well, except for the expected reduced intensities for e.g. the 1 0 3 parallel planes. A lot of intensity is diffracted into the area along the q_z axis which is not detectable. The peaks at high angles show lower intensities, as their Debye-Scherrer rings are mostly clipped by the edge of the detectors. The large background with a maximum at around 20° is a result of the substrate glass. In GIWAXS it is possible that the center of scattering does not coincide with the primary beam. This causes the reflex positions to shift and might be the reason why the peak positions do not fit perfectly. Due to the narrow area in the In-S phase diagram (Goedecke et al. 1985) the verification of the tetragonal β-phase confirms that the In$_2$S$_3$ samples have the correct stoichiometry and no sulfur deficit.
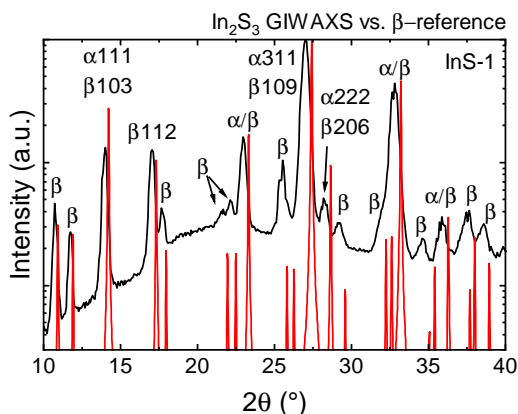
Figure 5.30: *Averaged GIWAXS measurement of sample **InS-1** compared to the calculated powder diffractogram of β-In$_2$S$_3$. Considering the peak shift of the measured data, nearly all β-In$_2$S$_3$ peaks are visible.*
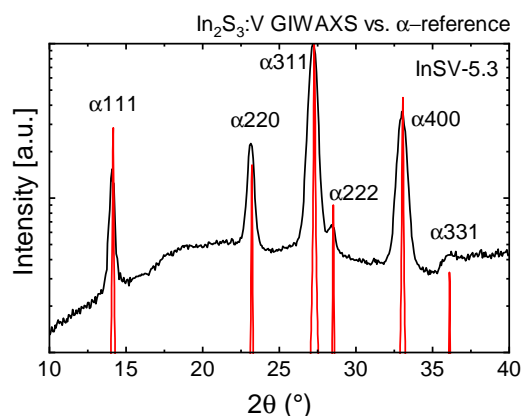
Figure 5.31: *Averaged GIWAXS measurement of sample **InSV-5.3** compared to the calculated powder diffractogram of α-In$_2$S$_3$. This sample is clearly in the α-phase.*

As we could already see in figure 5.30, the characteristic β-peaks vanish with high doping concentrations. This effect is very visible in the averaged GIWAXS intensities shown in figure 5.31. This time the reference is a calculated α-In$_2$S$_3$ diffractogram, showing that the sample is crystallized in the cubic α-In$_2$S$_3$. Both diffractograms shift similarly in this case, resulting in a near perfect match. The reflex intensities of the 1 1 1 parallel planes are again reduced because of the strong texture of the film, making

one of the planes undetectable. The 3 3 1 reflex is at the edge of the detector, so that most of the intensity is not detected. The large background is again a result of the glass substrate. The finding that the doping creates an order-disorder transition from β- to α-In$_2$S$_3$ can be further visualized. Figure 5.32 displays the integrated, averaged GI-WAXS intensity of the β1 1 2 reflex divided by the α3 1 1/β1 0 9 peak for all measured samples. Also shown as a reference is the expected value for a β-In$_2$S$_3$ powder calculated from PDF#00-067-0786. The undoped sample has a lower intensity ratio than the reference, which is explained by the influence of texture and the not detectable parts of the 2D-diffractogram. All samples doped with a transition metal show a reduced peak ratio indicating a bimorphism between β- and α-In$_2$S$_3$. Somewhere around 2 at.% doping the order-disorder transition to pure α-In$_2$S$_3$ is completed.
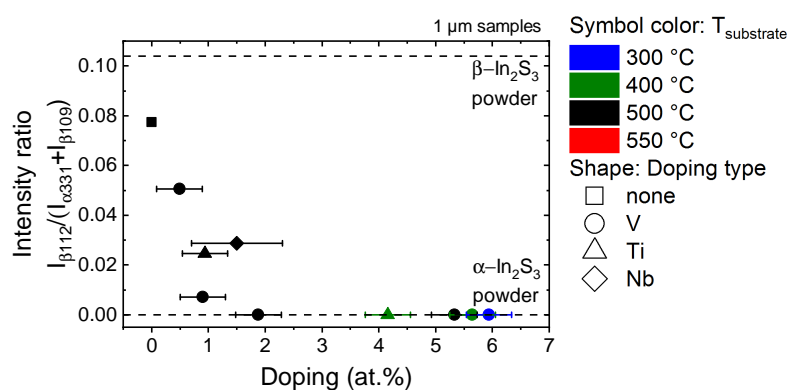
Figure 5.32: *Fraction of the β1 1 2 to the combined α3 1 1/β1 0 9 peak intensity plotted over the doping concentration. This fraction should be at 0.104 for β-In$_2$S$_3$ and 0 for α-In$_2$S$_3$. Doping with any transition metal causes a gradual order-disorder transition from the tetragonal β- to the cubic α-phase. The powder intensity ratios are taken from PDF#00-067-0787 for α-In$_2$S$_3$ and PDF#00-067-0786 for β-In$_2$S$_3$.*

It has to be checked if the observed phase transition is a result of a reduction of the sulfur concentration in the samples (see chapter 2.4). Figure 5.33 shows that there might be a trend to lower sulfur concentrations with higher doping concentrations. Some samples with higher doping concentration that were measured to be mostly in the α-phase (blue marker) should be mostly in the β-phase (red marker), if the sulfur concentration is correct. The uncertainty in the sulfur concentration measurement is large and it is uncertain how exact the sulfur deficiency induced phase transition points are applicable for these samples. It is therefore not possible to conclude if the

sulfur deficiency alone could be the cause of the phase transition. A similar transition from the β- to the α-phasehas been detected in In_2S_3:Fe by Chen et al. 2013.
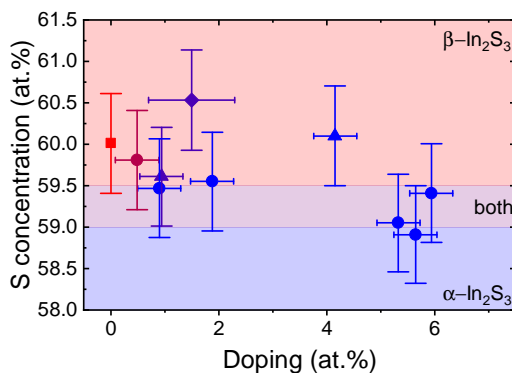
Figure 5.33: *Sulfur concentration (from EDS) plotted versus the doping concentration. The colored background marks the sulfur concentrations where the α-β-phase transition and bimorphism should occur in pure In_2S_3 Goedecke et al. 1985. The color of the measured data points corresponds to the intensity ratio shown in figure 5.32 with red (closer to β-In_2S_3), purple (bimorphism) and blue (closer to α-In_2S_3).*

To get another confirmation of the bimorphism it is possible to compare Raman spectra of the different samples. Utilizing inelastic Raman scattering, the characteristic lattice vibrations or phonon modes of a material can be detected. Details on the Raman measurements can be found in chapter 4.8.

Figure 5.34 displays the measurements on the V-concentration series. The pure In_2S_3 sample **InS-1** has many distinct Raman-active modes, while the doped samples have fewer and broader peaks. Group theory predicts a total of 36 active Raman modes for β-In_2S_3 (Lutz and Haeuseler 1971) and 5 for a spinel similar to α-In_2S_3 (Lutz 1969). A decrease in the peak number is therefore expected. The biggest change in the spectrum happens between 0.5 and $2\,at.\%$, where most of the modes vanish. This coincides with the vanishing of the $1\,1\,2$ reflex in the X-ray diffractograms.

While there is a good reference for a β-In_2S_3 from Kambas et al. (1981), there is none for α-In_2S_3. There are works that show Raman of a supposedly cubic In_2S_3 phase. One of them is from Lu, Wei, et al. (2018), but the contradictions in the phase naming,
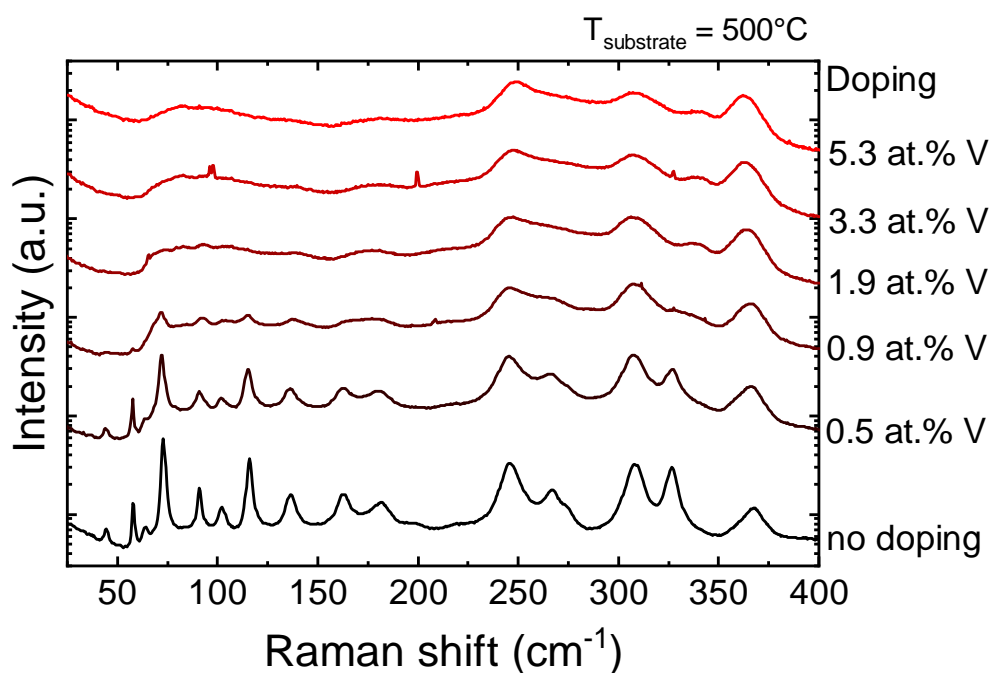
Figure 5.34: *Comparison of the Raman spectra of samples **InS-1**, **InSV-0.5**, **InSV-0.9**, **InSV-1.9**, **InSV-3.3**, **InSV-5.3**. The intensities are shown on a log-scale and shifted for better visualization. A lot of peaks vanish with the doping and the overall intensity decreases.*

the unconvincing XRD and selected-area electron diffraction (SAED) patterns and the incomplete Raman spectrum make it difficult to trust the phase determination. Tao et al. (2008) is another such publication where only θ-2θ XRD was used for phase determination. They assign the diffractogram to the cubic phase, while there are clearly reflexes that are characteristic to β-In$_2$S$_3$. As was shown above, distinguishing the α- from the β-phase is not always trivial. Nevertheless, because of lack of alternatives, the Raman spectrum of Lu, Wei, et al. (2018) will be used as a reference. For additional verification a comparison to MIn$_2$S$_3$ (M = Mn, Mg, Co ...) spinels (Lutz, Becker, et al. 1989; Ursaki et al. 2002) is done, which have similar cubic spinel structures to α-In$_2$S$_3$ and for the same reason were used as a substitution for theoretical calculations (Lucena, Conesa, et al. 2014).

Figures 5.35 and 5.36 compare the measured spectra of samples **InS-1** and **InSV-5.3** with literature values from Kambas et al. (1981), Lu, Wei, et al. (2018), and Ursaki et al. (2002). Most Raman peaks measured for sample **InS-1** can be attributed to β-In$_2$S$_3$

except for a few additional peaks that were not found in the measurements of Kambas et al. (1981) on single crystalline β-In$_2$S$_3$. The measurements on cubic indium sulfides from (Lu, Wei, et al. 2018; Ursaki et al. 2002) are missing most of the peaks found in measurements of sample **InS-1**. The α-In$_2$S$_3$ can be expected to look nearly identical to the β-In$_2$S$_3$ in the range 230 to $400\,\mathrm{cm}^{-1}$ Kambas et al. (1981), Lutz, Becker, et al. (1989), and Ursaki et al. (2002). This range is also where the Raman measurement of the sample **InSV-5.3** fits quite well on the references, except for one additional peak around $340\,\mathrm{cm}^{-1}$. The modes of the cubic MnIn$_2$S$_4$ are similar to our measurement of sample **InSV-5.3**, except for the peak with the highest energy, which is shifted for this particular MnIn$_2$S$_4$. In MnIn$_2$S$_4$ the highest energy mode does match the one measured here (Lutz, Becker, et al. 1989). The intensity ratios between the modes of MnIn$_2$S$_4$ is very different to the V-doped In$_2$S$_3$, but other cubic spinels like CoIn$_2$S$_4$ are similar in that regard making this comparison viable (Lutz, Becker, et al. 1989).
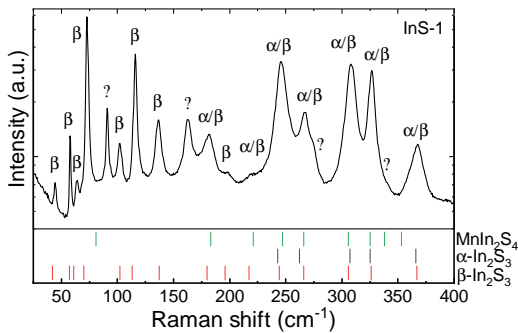
Figure 5.35: *Raman spectrum of sample **InS-1** compared to the peak positions of single crystals of β-In$_2$S$_3$ (Kambas et al. 1981), α-In$_2$S$_3$ flakes (Lu, Wei, et al. 2018) and MnIn$_2$S$_4$ single crystals (Ursaki et al. 2002).*
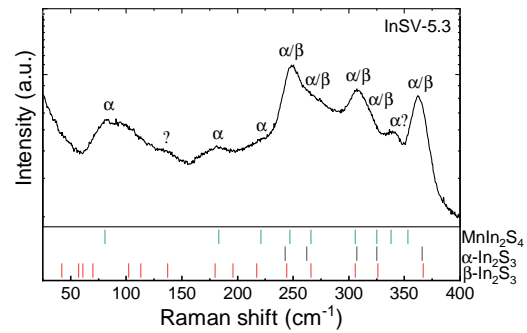
Figure 5.36: *Raman spectrum of sample **InSV-5.3** compared to the peak positions of single crystals of β-In$_2$S$_3$ (Kambas et al. 1981), α-In$_2$S$_3$ flakes (Lu, Wei, et al. 2018) and MnIn$_2$S$_4$ single crystals (Ursaki et al. 2002).*

The comparison to Raman measurements of other MIn$_2$S$_4$ (M = Mn, Mg, Co ...) cubic spinels indicates that the highly doped sample **InSV-5.3** is in the cubic α-phase(Lutz, Becker, et al. 1989; Ursaki et al. 2002). Additionally, most of the characteristic peaks of the β-phase vanish with doping, which is expected from theory (Lutz 1969; Lutz and Haeuseler 1971). It is likely that the remaining Raman peaks resemble the α-phase. The order-disorder transition from the tetragonal β-In$_2$S$_3$ to the cubic α-In$_2$S$_3$ detected with GIWAXS is therefore confirmed.

5.2.2   Secondary phases

There are no secondary phases detected with XRD or GIWAXS in samples doped with up to $6\,at.\%$ with transition metals (see figures 5.16 and 5.22).

The Raman spectra do show additional peaks, or at least changed peak intensities as seen in figures 5.34 to 5.36.

For pure β-In_2S_3 there are peaks at 91, 163, $\sim$275 and $\sim$340 cm^{-1} that are not visible in the reference (Kambas et al. 1981). The PVD growth method used here is known for its purity and the sensitive GIWAXS measurements showed no non-In_2S_3 peaks. It is most likely that these additional peaks are visible due to the difference in the β-In_2S_3 growth. The β-In_2S_3 in the reference are grown with a solid state reaction to be single crystals, while our samples are poly-crystalline thin layers with probably higher defect densities.

The transition metal-doped samples show a few additional peaks emerging with higher doping concentrations. Raman spectra of the highest doped samples grown at $500\,°C$ are shown in figure 5.37.
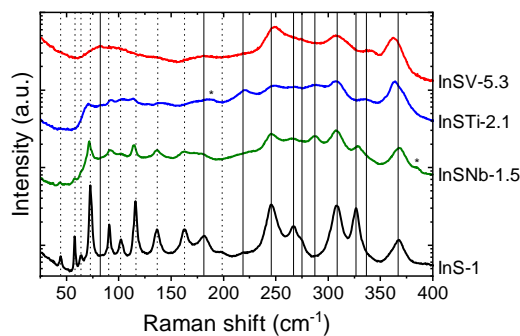
Figure 5.37: Raman comparison of highest doped samples against the undoped sample. Dotted lines indicate positions of modes that are most likely β-In_2S_3-characteristic, solid lines mark modes that are probably present in α and β phases. Stars mark the peaks that do not seem to be present in the pure In_2S_3 sample.

No mode assignment was attempted here, as the newest reference used for Raman assignments (Izadneshan et al. 2014; Spasevska et al. 2012) assumes to have a cubic

structure, while clearly showing a tetragonal one (Tao et al. 2008). In our first publication we also used the tetragonal InS_4 and octahedral InS_6 peak assignment (Wägele et al. 2017), but without another independent comprehensive Raman analysis we cannot be certain. It would be possible to use the mode assignments of cubic spinels from e.g. Ursaki et al. (2002), that based their assignment on previous measurements on cubic spinels by Gubanov et al. (1988) and Lutz, Becker, et al. (1989). But we have already seen that the intensities and mode positions are not necessarily the same for In_2S_3, making peak assignments difficult.

Two additional or shifted modes are detected in the shown Raman range. While no distinct additional peaks are detected for In_2S_3:V, In_2S_3:Ti has a new mode at $188\,cm^{-1}$ and In_2S_3:Nb at $385\,cm^{-1}$. The possibility of peaks from the glass substrate can be excluded as the laser is strongly focused on the surface of the sample and any such peaks would be visible in the sample **InS-1**. The most likely possibility is the emergence of modes from the additional bonds between transition metal and sulfur atoms. This can be the case for the $385\,cm^{-1}$ mode from the Nb-doping. The A_{1g} mode is found in other MIn_2S_4 spinels at similar energies (Lutz, Becker, et al. 1989; Ursaki et al. 2002). But without more elaborate measurements and a detailed mode analysis it is not possible to use these Raman measurements to distinguish secondary phases from doping induced changes.

5.2.3   Conclusion

With the help of GIWAXS and Raman measurements it was possible to determine that pure In_2S_3 samples were grown in the tetragonal β-phase. This verification confirms that the samples were grown with the correct stoichiometry of $40 \pm 0.5\,at.\%$ indium and $60 \pm 0.5\,at.\%$ sulfur.

Doping with transition metal concentrations of up to $6\,at.\%$ does not create any secondary phases that are detectable in XRD or GIWAXS, which is a good indicator for the incorporation of the dopants into the host In_2S_3 lattice.

The order-disorder transition from tetragonal β-In_2S_3 to cubic α-In_2S_3 due to doping could be confirmed. As was already apparent in the previous chapter 5.1, the transition metals do change the growth of In_2S_3, increasing the disorder of the crystal structure. The influence of a sulphur deficiency cannot be completely discarded. The

order-disorder transition is important to note for future theoretical calculations regarding intermediate bands in In$_2$S$_3$Ḃoth phases are very similar and as stated by Lucena, Aguilera, et al. (2008) the transition metals should still be able to create an equivalent intermediate band in the α-phase.

5.3 Crystal lattice

To quantify the changes the TM-doping induces in the In$_2$S$_3$ host lattice, we can analyze the XRD measurements in more detail.

5.3.1 Lattice constants

It is possible to calculate the lattice constants for the cubic α-In$_2$S$_3$ and tetragonal β-In$_2$S$_3$ lattices by using the already known lattice planes and XRD peak positions from section 5.1.2.

Calculating the cubic lattice constant a_{cubic} is straightforward and done with the data from one reflex (see equation 4.6). In the case of the tetragonal lattice two peaks have to be used to solve the equation with two unknowns a_{tet} and c_{tet} (see equations 4.8 and 4.9). The problem in our case is, that most samples are strongly 1 1 1 textured. The most accurate fits are only possible for the reflex-peaks of 1 1 1-parallel planes. Unfortunately, these parallel planes cannot be used together to calculate the tetragonal lattice constants. Additionally, we already know that only the pure In$_2$S$_3$ samples are truly in the tetragonal phase (see section 5.2.1), so the tetragonal lattice constants will only be calculated for these. The reflex choice and error calculation is explained in the appendix A.2.

For sample **InS-1** the results are $a_{tet} = 7.6030 \pm 0.0035$ Å and $c_{tet} = 32.341 \pm 0.015$ Å with a c/a-ratio of 4.254. For sample **InS-2** we get $a_{tet} = 7.6019 \pm 0.0035 \times 10^{-3}$ Å and $c_{tet} = 32.330 \pm 0.015$ Å with c/a-ratio of 4.253. The reflexes $\beta 5\,0\,15$ and $\beta 4\,2\,12$ have been used for this calculation. The lattice constants of both samples lie within the range of each other and the c/a-ratio is identical. Pistor et al. (2016) measured $a_{tet} = 7.6231 \pm 0.0004$ Å and $c_{tet} = 32.358 \pm 0.003$ Å, which shows a slightly larger unit cell. Their c/a-ratio is with 4.245 slightly smaller.

Since the main XRD reflexes of the β-In$_2$S$_3$ lattice are the same for the α-In$_2$S$_3$

lattice, it is possible to calculate cubic lattice constants for these samples, as well. The results from reflex $\alpha 5\,5\,5$ are $a = 10.762 \pm 0.005\,\text{Å}$ for sample **InS-1** and $a = 10.759 \pm 0.005\,\text{Å}$ for sample **InS-2**. When extrapolating the α-In_2S_3 measurements of Pistor et al. (2016) to room temperature (see appendix A.2) this gives us a reference value of $a = 10.7816\,\text{Å}$ which is again larger than the measured value.

Both the cubic and tetragonal unit cells are smaller than the ones in literature. The latter were obtained by elaborate full-profile fitting of powder diffractograms, which gives much more accurate results than our use of uncorrected peak positions of textured thin-films. Our samples are poly-crystalline thin films instead of ground single crystals. Thin films are always subject to strain, grain boundaries and higher defect densities, changing the mean lattice constant of the crystallites (see section 2.1.1). Since all samples are polycrystalline thin films, this should not affect the qualitative analysis of the changes due to hyperdoping with transition metals.

For the doped samples only the cubic lattice constants are calculated using the $\alpha 5\,5\,5$-reflex. The results for all samples, including the $60\,\text{nm}$ samples, are shown in figures 5.38 through 5.40. Because of the amorphous substrate, no additional strain is introduced at the substrate interface, enabling the use of these samples for a larger statistic.
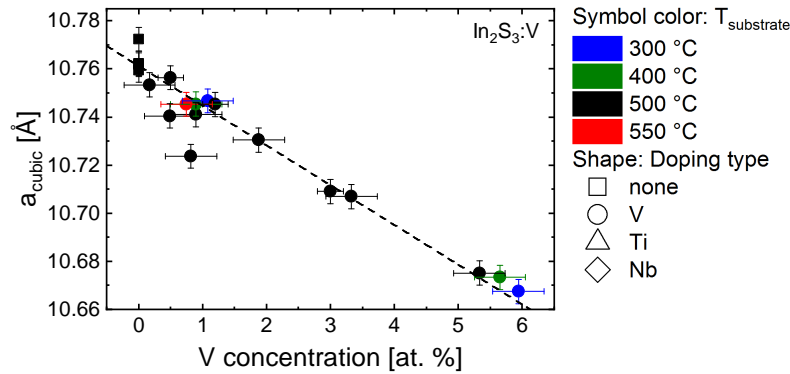
Figure 5.38: *Cubic lattice constants of all In_2S_3:V samples.*

A linear decrease in the lattice constants is detectable for all three dopants. This fact reveals that the TM atoms are inserted into the host In_2S_3 lattice. As was shown in section 5.2.2, they also do not form any crystalline secondary phases. It is likely that most TM atoms are incorporated. It is still possible to have amorphous TM clusters, as
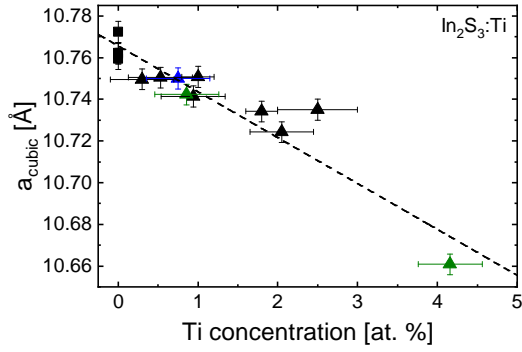
Figure 5.39: *Cubic lattice constants of all In$_2$S$_3$:Ti samples. The legend is shown in figure 5.38.*
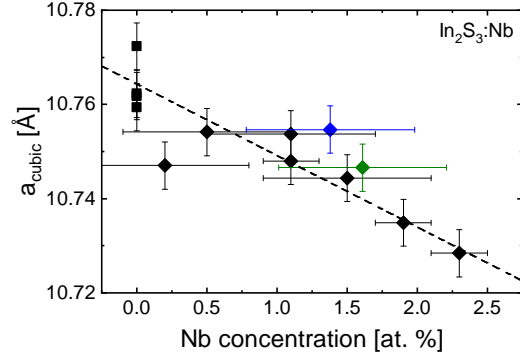
Figure 5.40: *Cubic lattice constants of all In$_2$S$_3$:Nb samples. The legend is shown in figure 5.38.*

XRD and GIWAXS are bulk measurement techniques, detecting only crystalline material. The confirmation of the incorporation is crucial, as only the TM atoms integrated into the host lattice can contribute to the formation of an intermediate band.

The three linear regressions of the lattice constant decrease are given by

$$V : a_{cubic} = -0.0165(9)\,\text{Å at.\%}^{-1} * x_V + 10.761(2)\,\text{Å}$$
$$Ti : a_{cubic} = -0.015(3)\,\text{Å at.\%}^{-1} * x_{Ti} + 10.761(3)\,\text{Å} \qquad (5.1)$$
$$Nb : a_{cubic} = -0.015(2)\,\text{Å at.\%}^{-1} * x_{Nb} + 10.764(2)\,\text{Å}$$

with the concentrations x_M of the three dopants. To improve the fit on the In$_2$S$_3$:Ti data the two outliers (**InS-60-2** and **InSTi-4.2-400**) had to be removed from the fit. All three dopants show a nearly identical slope which hints to the incorporated atoms having similar crystal radii.

5.3.2 Crystal defects

We could already see in chapter 5.1 that the TM-doping decreases the crystal quality. It is possible to quantify this effect from the available XRD data.

We can extract the mean microstrain ϵ inside the grains of a sample from the FWHM of the XRD reflexes (see section 4.3). The microstrain describes the strain of the different crystal defects inside a grain on the crystal structure, as the crystal lattice constants change to accommodate for these defects.

In figure 5.41 the XRD FWHM of different $1\,\mu\text{m}$ samples are displayed. The FWHM increases with higher doping concentrations for all substrate temperatures and dopants. The strongest increase comes from lowering the substrate temperature during growth to $300\,°\text{C}$. The difference between 400, 500 and $550\,°\text{C}$ is negligible. These results are similar to the morphology and texture observations in chapter 5.1.
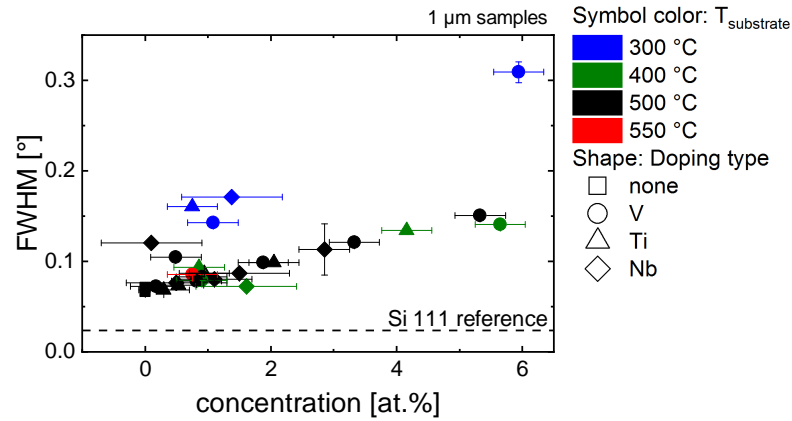
Figure 5.41: *FWHM of the $\alpha2\,2\,2/\beta2\,0\,6$ reflex of $1\,\mu\text{m}$ samples. A systematic increase of the FWHM with the doping concentration is detected. The lower $300\,°\text{C}$ growth temperature increases the FWHM significantly.*
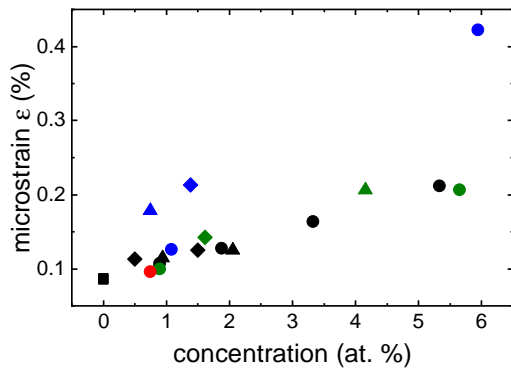
Figure 5.42: *Microstrain of all samples with measured crystal sizes. The samples grown at $300\,°\text{C}$ (blue) are outliers compared to the rest.*
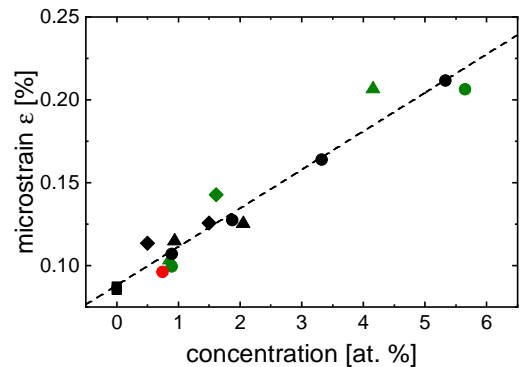
Figure 5.43: *Microstrain of samples grown at 400 or $500\,°\text{C}$ including a linear fit.*

To get the microstrain ϵ from the FWHM it is best to include all measured reflexes and fit the FWHM(θ) dependence (formula 4.10) for every sample. This way it is possible to consider the effects of grain size and instrument broadening on the FWHM.

By providing the grain size (approximately the crystal size from SEM, table 5.1) to the fit, only the microstrain has to be fitted. This approximation does improve the regression as it eliminates one variable.

The microstrain of the samples with available crystal sizes is shown in figure 5.42. It looks very similar to the FWHM. When excluding the $300\,°C$ samples, we get a linear dependence of the microstrain ϵ on the doping concentration c (see fig. 5.43):

$$\epsilon = 0.0233(15)\,\%\,at.\%^{-1} * c + 0.0881(39)\,\% \tag{5.2}$$

Table 5.3 lists the microstrain of a few samples. This strain is of course the mean strain of all the grains of a sample and gives a good indication of the defect density trend. The absolute values are not exact, as a few assumptions are made that cause a systematic error by an unknown amount: The instrument broadening is only roughly estimated and the grain size is assumed to be equal to the measured surface crystallite sizes. The statistic error can be estimated from the final linear fit (fig. 5.43) and is around $5\,\%$ relative. There are more advanced techniques involving deconvolutions or fourier analysis, but the analysis done here is sufficient for the desired sample comparison.

It is also possible to get the strain from Raman by checking the peak position change of the main modes (Chong et al. 2019). Unfortunately, the peak positions also change with the doping concentrations which makes it very difficult to separate these two effects.

The high doping concentrations around 4 to $6\,at.\%$ double the microstrain in comparison to pure In_2S_3. As the strain in the crystallites is caused by defects, a higher defect density can be expected in these samples. These defects can also come from the increased amount of grain boundaries between the smaller crystallites, but the $400\,°C$ samples with even smaller crystallites do not show an increased microstrain. This warrants the conclusion that the TM atoms themselves increase the defect densities, likely due to their lower mobility on the crystal surface. The $300\,°C$ substrate temperature consistently increases the defect density to a degree, that it had to be excluded from the fit to the rest of the data. This is most likely again caused by the significantly reduced mobility that causes the incoming atoms and molecules to settle in unfavorable positions, increasing the strain inside the growing grains.

Table 5.3: *Microstrain ϵ of a few representative samples. The absolute values are not exact, as a few assumptions have been used that may cause a systematic error by an unknown amount.*

Sample	ϵ (%)
InS-1	0.087(4)
InS-2	0.085(4)
InSV-0.8-550	0.096(5)
InSV-0.9	0.107(5)
InSV-0.9-400	0.099(5)
InSV-1.1-300	0.126(6)
InSV-5.3	0.212(12)
InSV-5.7-400	0.206(12)
InSV-5.9-300	0.422(13)
InSTi-0.9	0.115(5)
InSTi-2.1	0.125(7)
InSTi-4.2-400	0.206(10)
InSNb-0.5	0.114(5)
InSNb-1.5	0.126(6)
InSNb-1.6-400	0.143(6)

5.3.3   Conclusion

The decreasing lattice constants together with the absence of secondary phases are a strong indicator for the incorporation of the transition metals into the In_2S_3 crystal lattice. This means that a potential intermediate band should form, if the transition metal concentrations are sufficiently high for an overlap of the band gap energy states to occur.

Doping with any transition metal causes the defect density to increase. More grain boundaries do not seem to be the reason, but a lower mobility of the transition metals might be. It is also possible that local TM concentration differences cause lattice constant deviations in a grain, causing defects and therefore microstrains in the crystal lattice.

Comparing the linear strain increase with doping to the β- to α-In_2S_3 transition (fig. 5.32), it becomes apparent that the order-disorder transition between 1 and $2\,\mathrm{at.\%}$ does not relieve any strain on the crystal structure. This can be expected as the disordered α-phase is nearly identical and cannot incorporate the transition metals any better than

the β-phase. If the strain increase is mainly due to the low mobility of the transition metals, it should be independent of the crystal phase.

The mobility of the In and/or S atoms also seems to affect the microstrain, as the samples grown at the lower temperature of $300\,°C$ have a significantly higher microstrain. There seems to be a minimum temperature between 300 and $400\,°C$ needed for the In$_2$S$_3$:TM crystals to grow larger and with less defects. Any further temperature increase mainly impacts the crystallite size and texture, but not the defect density in the crystallites themselves.

Chapter 6

Analysis of the transition metal environment in In$_2$S$_3$:TM

After the analysis of effects of the TM incorporation on the crystal growth, we go into more detail on the TM atoms themselves. A useful intermediate band is only formed if the TM atoms are situated on the correct lattice positions with the correct oxidation state. The lattice positions determine the distance and interaction between the TM atoms and therefore the energy position of the IB, while the oxidation state defines the free electrons that can fill the IB.

6.1   Chemical environment

The chemical environment around the transition metal atoms can be measured with X-ray photoelectron spectroscopy (XPS) (see chapter 4.11). Due to time constraints only three samples were measured with this technique: A reference sample **InS-3**, and the two doped samples **InSV-0.8** and **InSNb-1.1**.

An overview graph of the XPS measurments is shown in figure 6.1 together with the peak assignments. Despite the careful preparation and transportation without air exposure it could not be completely avoided having carbon and oxygen present on the surface (C 1s and O 1s). V 2p and Nb 3d peaks are detectable in the vanadium and niobium hyperdoped samples, respectively. The remaining peaks can be attributed to indium (In 3p, In 3d, In 4d, In MNN) and sulfur (S 2s and S 2p, S LMM).
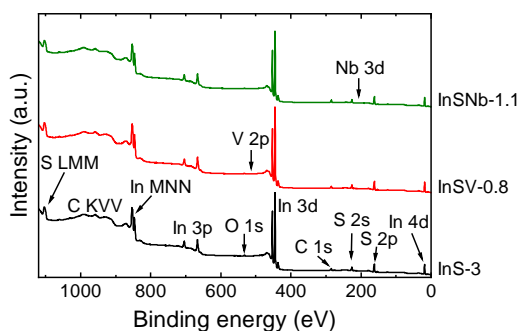
Figure 6.1: *XPS overview of the three samples before Ar$^+$ cleaning. The expected peaks from In and S are dominating the spectrum, while small O and C peaks are detectable. The peaks from V and Nb are very small and not visible in this overview. The intensities for each sample are shifted to better separate the samples.*

All three samples are treated with $50\,\text{eV}$ Argon ions (Ar$^+$) to remove some carbon and oxygen from the surface. As shown in figures 6.2 and 6.3 in all samples the amount of surface oxygen could be reduced, while no carbon was removed from the reference In$_2$S$_3$ sample. Oxygen is the problematic element and the overall amount on the surface is very low. But since it is present, it can form bonds with In or the TMs.
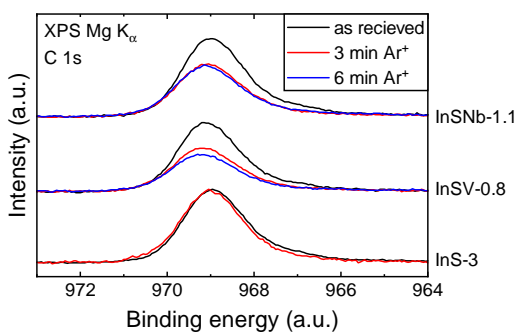
Figure 6.2: *The C 1s peak of all three samples before and after Ar$^+$ treatment for 3 and 6 minutes. The intensities for each sample are shifted to better separate the samples.*
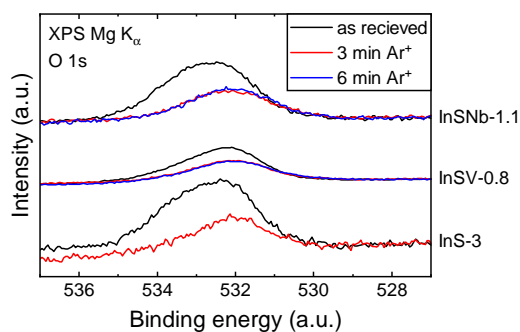
Figure 6.3: *The O 1s peak of all three samples before and after Ar$^+$ treatment for 3 and 6 minutes. The intensities for each sample are shifted to better separate the samples.*

The cleaning step does affect the surface so that we have to check on the changes of the In peaks. Figures 6.4 and 6.5 display the In 3d and In MNN peaks for all cleaning steps. There are slight shifts in the peak position after cleaning, but this can be caused by charging the surface of the sample. To eliminate this effect, we can calculate the modified Auger parameter of indium α'_{In} by adding the kinetic energy of the In MNN

Auger peak and the binding energy of the In 3d peak (see chapter 4.11). α'_{In} is shown in figure 6.6 for the three samples and all cleaning steps. There is no real trend following the Ar^+ treatment and all values lie within each other's errors at around $\alpha'_{In} = 852.5\pm 0.1\,eV$. This result fits well within the range of literature values between 852.0 and $853.3\,eV$ (Moretti 1998; Powell 1989). It can be said that neither the cleaning nor the doping strongly impact the In atoms. For the remaining analysis only the cleaned samples are shown.
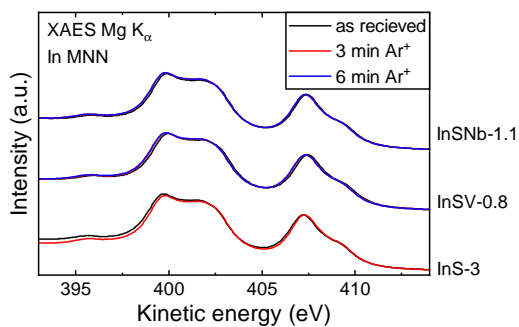
Figure 6.4: *The In MNN Auger peak of all three samples before and after being Ar^+ treated for 3 and 6 minutes. The intensities for each sample are shifted to better separate the samples.*
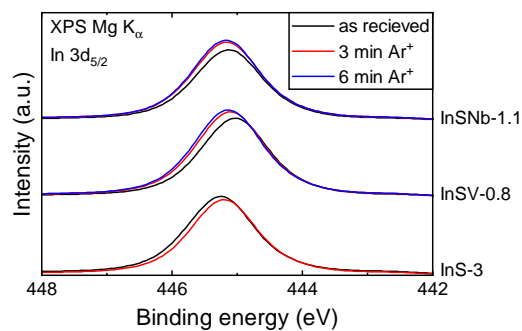
Figure 6.5: *The In $3d_{5/2}$ peak of all three samples before and after being Ar^+ treated for 3 and 6 minutes. The intensities for each sample are shifted to better separate the samples.*
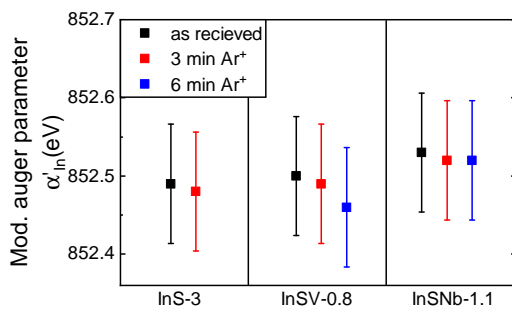
Figure 6.6: *Modified Auger parameter of indium α'_{In} for the three samples and cleaning steps. Slight changes occur, but all values are within the estimated errors.*
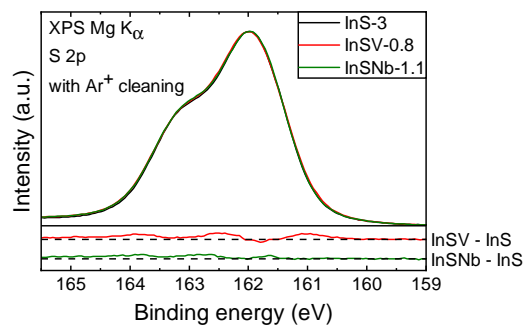
Figure 6.7: *S 2p peak of the three samples. The differences in the peaks displayed below are multiplied by a factor of two, to better show the changes.*

The S 2p peak of the doped samples is slightly broader than for the pure sample. Figure 6.7 displays this peak for the three samples as well as the differences between

the undoped and doped samples.

The next figure 6.8 displays the XPS spectrum of the V 2p peaks together with literature values of different V compounds. The peaks have been fitted with two Voigt profiles and a nearly symmetric split Voigt profile for the lowest energy peak. Comparing these fits to literature data (Powell 1989), it can be assumed that the V on the sample's surface is mainly bound to sulfur ($513.2\,\text{eV}$), but also to oxygen ($515.2\,\text{eV}$). Metallic vanadium might also be present ($512.3\,\text{eV}$). Comparing the V $2p_{3/2}$ binding energy with XPS measurements on other vanadium sulfides, the V^{5+} can be safely excluded, as it has a higher binding energy of around $517\,\text{eV}$ (Zhou et al. 2017). V^{4+} in VS_4 is placed between 513.5 and $514\,\text{eV}$ (Shimoda et al. 2019; Wang et al. 2018; Weimer et al. 2017) which is closer to our measurement, but still at slightly higher energies. Measurements on V_2S_3 show the V $2p_{3/2}$ peak at lower energies of $513\,\text{eV}$ (Weimer et al. 2017), which indicates that V^{3+} can be expected to be closer to the $513.2\,\text{eV}$ that we measured. Since vanadium is substituting In^{3+} in In_2S_3:TM and does not change the crystal structure, it can be expected that V is mainly present as V^{3+}, while V^{4+} cannot be completely excluded.
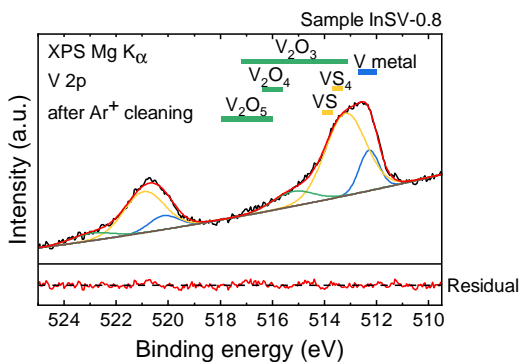
Figure 6.8: *Fit on the V 2p peak of sample **InSV-0.8**. Three fits describe the peak and can be attributed to V-O, V-S and V-V bonds by comparison with literature values for different V compounds (Powell 1989). The influence of the O 1s peak has been subtracted before fitting.*
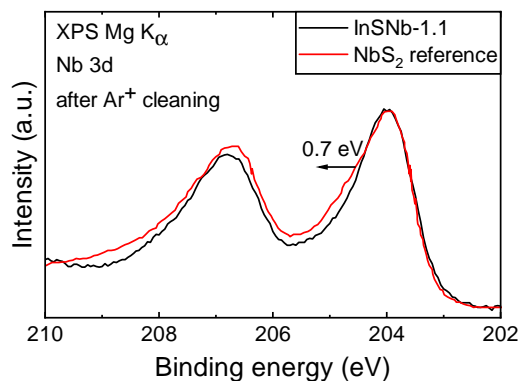
Figure 6.9: *Comparison of the Nb 3d peak of sample **InSNb-1.1** to a $0.7\,\text{eV}$ shifted NbS_2 spectrum from the publication of Ettema et al. (1993). The spectra look very similar.*

It is possible to estimate the portion of each of the vanadium bonds by calculating the integrated intensities for all three peaks. The contributions of the peaks to

the overall intensity are shown in table 6.1. The results show that about $70\,\%$ of the vanadium atoms are bound to sulfur on the surface of sample **InSV-0.8**.

$13\,\%$ of the V atoms on the surface are bound to oxygen. The sample measured with XPS was not directly exposed to air, so the oxygen amount on other samples can be much higher. Oxygen is known to increase the band gap of In_2S_3 (Barreau, Marsillac, Bernède, and Assmann 2003) and introduce defects (Pai et al. 2005) which should be noticeable in the absorption and photoluminescence experiments. No In-O bonds were detected and as shown in chapter 7.1.1 the band gap energy is as expected for pure In_2S_3, despite having those samples repeatedly exposed to air.

Table 6.1: *The intensity contributions to the V 2p XPS peaks of **InSV-0.8**, which equal the bond ratios on the surface of the sample.*

Peakposition (eV)	Bond	Bond ratio (%)
512.3	V-V	16.8
513.2	V-O	12.7
515.2	V-S	70.5

Interesting is the existence of the metal-like V compound that was not detected with other methods. XRD shows a good incorporation into the host lattice and there are no visible V clusters in SEM/EDX. Its amount is with $16.8\,\%$ even larger than the V-O bonds. While Ar^+ bombardment with high energies is known to reduce transition metal oxides and sulfides (Coyle et al. 1980; Kasperkiewicz et al. 1983), the lower energy Ar^+ sputtering did not have any effect on the shape of the V 3d peaks in our case. It has been shown that V-V bonding does occur to a significant amount in various V-S compounds (England et al. 1974; He et al. 2007). This can be one explanation for the V-V bonds in hyperdoped In_2S_3:V. This would mean that V can be expected to also occupy S positions. Unfortunately small amorphous V clusters cannot be excluded to exist, as they would have been difficult to detect with the analysis methods used.

The Nb 3d peaks of sample **InSNb-1.1** are displayed in figure 6.9 together with NbS_2 literature data from Ettema et al. (1993). The NbS_2 data were shifted by $0.7\,eV$, to compare the XPS peak shapes to our measurement. Both peak shapes of the Nb $3d_{5/2}$ and the Nb $3d_{3/2}$ electrons in NbS_2 look very similar to our measurement of In_2S_3:Nb. Other XPS measurements on NbS_2 alos show similar Nb 3d peak positions and shapes

without a shift in the peak position (Bark et al. 2018; Dash et al. 2015; Mansouri et al. 2018). It is therefore safe to assume that the Nb-S bonding is comparable to pure NbS_2, where Nb is present as Nb^{4+}. Nb-O bonds (Nb $3d_{5/2}$ $207\,eV$ for Nb_2O_5 (Powell 1989)) cannot be excluded. Nb-Nb bonds (Nb $3d_{5/2}$ $202\,eV$ (Powell 1989)) do not seem to be present.

6.1.1   Conclusion

The XPS measurements on samples **InSV-0.8** and **InNb-1.1** show both transition metals binding mainly to sulfur as V^{3+} (similar to V_2S_3) and Nb^{4+} (similar to NbS_2).

Additional V-O and V-V bonds were detected in the In_2S_3:V sample. The samples did show small amounts of oxygen on the surface, that was not completely removed by the Ar^+ treatment, explaining the presence of V-O bonds. The existence of V-V bonds can have multiple reasons. The simplest explanation is the presence of Vanadium clusters in the sample. These are difficult to detect and cannot be excluded to exist. The large amount of V-V bonds would have been detected in XRD, if the vanadium forms ordered V metal clusters. Since this is not the case, the clusters have to be amorphous, if they exist at all. Another explanation is given by intrinsic V-V bonds that have been previously detected in vanadium sulfides. This would be possible if some vanadium atoms substitute sulfur.

Nb-O bonds are not as pronounced for the In_2S_3:Nb sample, but likely present. Nb-Nb bonds on the other hand are not detected.

6.2   Coordination number and lattice position

Extended X-ray absorption fine structure (EXAFS) is used to resolve the local environment of the transition metal atoms. Due to the complexity of the experiment the focus is set on hyperdoped In_2S_3:V samples. This includes a concentration variation with samples **InSV-1.9**, **InSV-3.3** and **InSV-5.3** and a substrate temperature variation with samples **InSV-5.9-300**, **InSV-5.7-400** and again **InSV-5.3**. Unfortunately, because of relatively low V concentrations and complications during the measurement, the signal-to-noise ratio is not very good. The EXAFS analysis is therefore focused on the absorption edge position and the first shell (see chapter 4.6).

6.2.1 V K absorption edge

The measured V K absorption edges are displayed in figure 6.10. All samples look very similar, but samples **InSV-1.9** and **InSV-5.9-300** are slightly shifted compared to the other three. This becomes even more apparent when plotting the edge position for all five samples in figure 6.11. Table 6.2 lists the measured values.

The V K absorption edge of the lowest doped sample **InSV-1.9** has the lowest energy position. The higher doped samples **InSV-3.3** and **InSV-5.3** have the same energy within the error margin with $0.39\,\text{eV}$ and $0.38\,\text{eV}$ above **InSV-1.9**.

The temperature series shows a similar behavior with the lowest temperature sample **InSV-5.9-300** at the highest absorption edge position. The other two samples **InSV-5.7-400** and **InSV-5.3** are again at the same energy position $0.32\,\text{eV}$ below **InSV-5.9-300**.
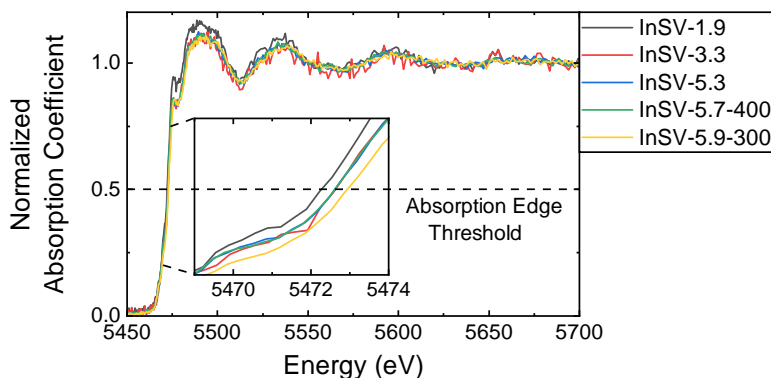
Figure 6.10: *V K absorption edges of all measured In_2S_3:V samples. The insert shows a detailed view of the spectrum near the absorption threshold.*

Table 6.2: *V K absorption thresholds obtained from EXAFS measurements.*

Sample	Threshold position (eV)	difference to InSV-5.3 (eV)
InSV-1.9	5472.25(4)	-0.38
InSV-3.3	5472.64(12)	0.01
InSV-5.3	5472.63(4)	-
InSV-5.7-400	5472.63(4)	0.00
InSV-5.9-300	5472.95(4)	0.32

The position of the X-ray absorption edge of an atom has long been used as an
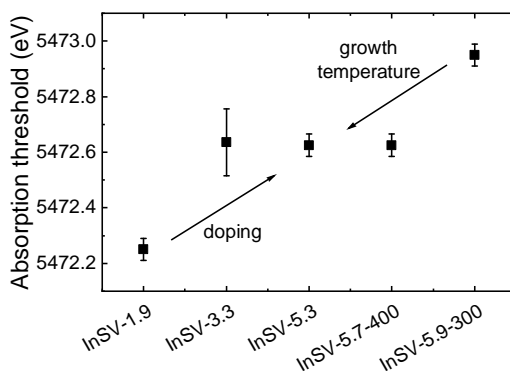
Figure 6.11: V K absorption thresholds of all measured In$_2$S$_3$:V samples.

indicator for the oxidation state of a material (Kunzl 1932; Wong et al. 1984). But as discussed by Glatzel et al. (2009) bond distances also have a large impact on the absorption edge, especially if there are constraints on the atom's positioning. In the case of In$_2$S$_3$ the vanadium atoms are very constraint by the host lattice. This means that the position of the absorption edge will be dependent on both the oxidation state and the band distance.

In the work of Wong et al. (1984) the vanadium absorption edge position shift is solely attributed to the change of the oxidation state. They measured a change of $2.5\,\mathrm{eV}$ per oxidation state for vanadium oxides. The maximum change from sample **InSV-1.9** to sample **InSV-5.9-300** of $0.7\,\mathrm{eV}$ would mean a reduction of the mean V valence by 0.3.

Following the work of Glatzel et al. (2009) it is also possible to interpret the absorption edge shift solely as a change in the bond length. Their measurements and calculations on manganese compounds showed a bond-length dependent shift of the absorption edge by about -12 to $-14\,\mathrm{eV/\mathring{A}}$. The measured $0.7\,\mathrm{eV}$ shift would therefore result in a bond-length shift of about -0.05 to $-0.06\,\mathring{A}$ from sample **InSV-1.9** to sample **InSV-5.9-300**.

We calculate the actual bond lengths from EXAFS (see 6.2.2) which shows the expected trend of a decreasing bond length. But the bond length shift is with $-0.03\,\mathring{A}$ smaller. The estimated -0.05 to $-0.06\,\mathring{A}$ are of course based on manganese and not vanadium. Assuming that the value is in that -0.05 to $-0.06\,\mathring{A}$ range, the absorption edge shift originating from a bond length change of $-0.03\,\mathring{A}$ would be $0.4\,\mathrm{eV}$. Subtract-

ing this from the measured $0.7\,\text{eV}$ leaves about $0.3\,\text{eV}$ to be explained by the oxidation state. Unfortunately the $2.5\,\text{eV}$ shift per oxidation state from Wong et al. (1984) is also a mixture of both effects and can therefore not be used to calculate the true oxidation shift. On the other hand this also means, that the real oxidation state change could be somewhere in the range of 0.3 as calculated above, if vanadium sulfides behave the same as vanadium oxides.

Only one sample (**InSV-0.8**) was measured with XPS (see chapter 6.1), so the existence and magnitude of a valence change in the EXAFS data cannot be verified.

6.2.2 Bond length and coordination number

The EXAFS region is analyzed by fitting the fine structure equation 4.15 with a structure model on the measured data. A detailed description of the process can be found in section 4.6. The results of this fitting are listed in table 6.3 and shown in figures 6.12 to 6.14. For the threshold difference between theory and measured spectrum a fixed value of $\Delta E_0 = -0.1$ was found to represent all samples. This reduces the amount of fit parameters to three: The mean bond length R, the variance of the bond length distribution σ^2 and the product of coordination number N and amplitude reduction factor S_0^2: $N S_0^2$.

Table 6.3: *Results from fitting the fine structure equation on the EXAFS data with fixed $\Delta E_0 = -0.1$.*

Sample	Bond length (Å)	σ^2 (Å^3)	$N S_0^2$
InSV-1.9	2.495(10)	0.004(3)	2.9(6)
InSV-3.3	2.491(13)	0.003(4)	2.5(7)
InSV-5.3	2.484(5)	0.004(2)	2.6(3)
InSV-5.7-400	2.481(8)	0.007(3)	2.9(4)
InSV-5.9-300	2.467(7)	0.012(3)	3.1(4)

The bond lengths displayed in figure 6.12 are in the range 2.47 to $2.50\,\text{Å}$ and decrease slightly with higher doping concentrations and lower growth temperatures. The uncertainties of the values are larger than the changes from one sample to the next, but there is a significant decrease between sample **InSV-1.9** and **InSV-5.9-300**. Like in all other experiments before, the largest change seems to come from lowering the growth
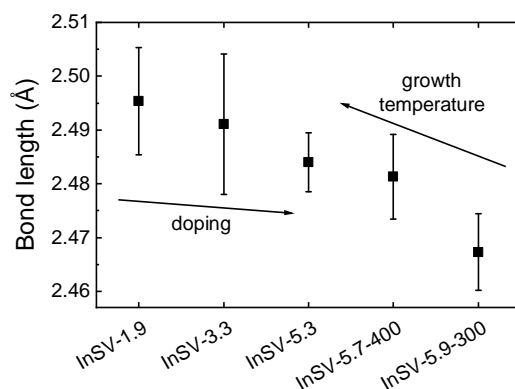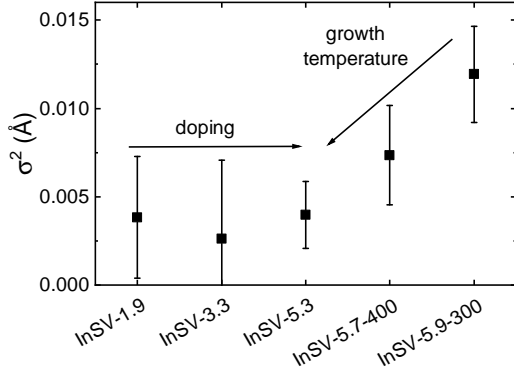
Figure 6.12: *The bond length R after the final numerical fitting procedure using the tetrahedral structural model with $\Delta E_0 = -0.1$.*

temperature to $300\,°C$. This result verifies the behavior of the V K X-ray absorption threshold, where the same trends were visible: Higher doping and lower substrate temperatures during growth decrease the mean bond length between vanadium and the nearest sulfur atoms.

This is in accordance with the decreasing lattice constants measured with XRD (see chapter 5.3.1). The more V atoms occupy In positions, the smaller the crystal lattice becomes, shifting the S atoms closer to the V atoms. These shorter V-S bonds are preferred by vanadium as seen in the material comparison in table 6.4. The low substrate temperature of $300\,°C$ hinders the In_2S_3 growth (as concluded in section 5.3.3) so that higher defect densities might relax the boundary conditions for the V-S bonding, allowing the vanadium to form energetically preferred closer bonds.

To translate the V-S distances of about 2.47 to $2.50\,Å$ into a lattice position, it is necessary to compare them to the host lattice and other known vanadium sulfides. The In-S distances in In_2S_3 and V-S distances in other materials are displayed in table 6.4. The In-S bond length in In_2S_3 depends on the position in the lattice. Tetrahedrally coordinated indium atoms are with 2.46 to $2.47\,Å$ (Pistor et al. 2016; Steigmann et al. 1965) closer to their four sulfur partners than octahedrally coordinated indium atoms with 2.59 to $2.64\,Å$ (Pistor et al. 2016; Steigmann et al. 1965) to their six sulfur partners. The difference between α-In_2S_3 and β-In_2S_3 is negligible, so they cannot be distinguished here. Taking just the bond lengths as an indicator one would assume that the tetrahedral positions are a better fit for the incorporation of V into In_2S_3. Ghorbani, Erhart,

et al. (2019) have calculated the bond lengths for octahedral V in β-In_2S_3:V. The result shows V_{Oh}-S at 2.49 Å, which is in the bond length range that was measured here. Just from the bond length it is therefore not possible to decide the position V prefers to occupy.

Table 6.4: *Bond length comparison to other materials. 8c and 16h denote the two octahedral position in β-In_2S_3. The V-S bond length in In_2S_3:V is similar to octahedral V-S bonds in other materials, but the octahedral In-S bonds of In_2S_3 are longer.*

Material	Bond	Coordination	Bond length (Å)	Source
α-In_2S_3:V	V-S	4	2.47 - 2.50	this work
β-In_2S_3:V	V-S	6	2.49	Ghorbani, Erhart, et al. 2019
α-In_2S_3	In-S	4	2.47	Pistor et al. 2016
α-In_2S_3	In-S	6	2.64	Pistor et al. 2016
β-In_2S_3	In-S	4	2.46	Pistor et al. 2016 Steigmann et al. 1965
β-In_2S_3	In-S	6 (8c)	2.59 - 2.61	Pistor et al. 2016 Steigmann et al. 1965
β-In_2S_3	In-S	6 (16h)	2.60 - 2.63	Pistor et al. 2016 Steigmann et al. 1965
V_3S_4	V-S	6	2.33 - 2.50	Kawada et al. 1975 Bensch et al. 1993
V_5S_8	V-S	6	2.31 - 2.45	Kawada et al. 1975
VS_4	V-S	8	2.41	Allmann et al. 1964
α-V_3S	V-S	4	2.32 - 2.46	Pedersen et al. 1959
β-V_3S	V-S	4	2.31 - 2.47	Pedersen et al. 1959

The variance of the bond length distribution σ^2 (figure 6.13) is constant within the uncertainty for the $500\,°C$ samples, and increases for samples grown at lower temperatures. σ^2 is a measure of the local order around the V atoms, so it is not unexpected to see it increase especially for the $300\,°C$ which showed a higher disorder in the other experiments. The crystal quality difference between 400 and $500\,°C$ was barely noticeable in SEM, XRD and GIWAXS, if at all. But on the atomic level the higher growth temperature seems to increase the local order around the V atoms. Unfortunately the low data quality makes this interpretation only significant for the jump from 300 to $500\,°C$.

The mean amplitude reduction factor NS_0^2 for all samples shown in figure 6.14

Figure 6.13: *The variance of the bond length distribution σ^2 after the final numerical fitting procedure using the tetrahedral structural model with $\Delta E_0 = -0.1$.*
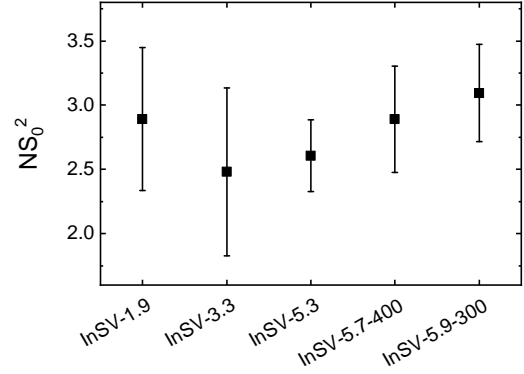
Figure 6.14: *The variance of the bond length distribution σ^2 after the final numerical fitting procedure using the tetrahedral structural model with $\Delta E_0 = -0.1$.*

is about 2.8, with all sample values within the error bars of the other samples. It is therefore not possible to declare a significant trend for NS_0^2. We are mainly interested in the coordination number N, so we have to separate it from S_0^2 by doing a literature comparison. Li et al. (1995) did an extensive survey of the S_0^2 values for a lot of different materials with transmission EXAFS. The group of C. S. Schnohr (2021) compared S_0^2 values for transmission- and fluorescence EXAFS measurements as shown in table 6.5.

Our NS_0^2 values measured in fluorescence are between $2.5(7)$ and $3.1(4)$. Assuming a tetrahedral coordination with $N = 4$, S_0^2 would have to be in the range $0.63(18)$ to $0.78(10)$. For octahedral coordination with $N = 6$, the S_0^2 range would change to between $0.42(12)$ and $0.52(7)$. While V (Z = 23) was not measured, S_0^2 values from other transition metals like Ni (Z = 28) and Cu (Z = 29) are available. They are all in the range 0.64 to 1.20 for transmission measurements. The comparison between amplitude reduction factors measured in transmission and fluorescence show that S_0^2 values from fluorescence are even larger. This might lead to the conclusion that for the determined S_0^2 range the octahedral coordination with $N = 6$ is unlikely and tetrahedral coordination is favored. Unfortunately this value comparison is still no substantial proof of tetrahedral coordination.

Newer EXAFS measurements on these samples and their analysis became available during the finalization of this thesis. These show that, while the bond-length is unfavorable for octahedral coordination, it still seems energetically favorable for V to sit

Table 6.5: *Comparison of the amplitude reduction factors S_0^2 for various materials, elements and both transmission and fluorescence modes.*

Material	Z	EXAFS modus	S_0^2	Source
CuO	Cu (29)	trans.	0.64(1)	Li et al. 1995
Cu_2O	Cu (29)	trans.	0.69(2)	Li et al. 1995
NiO	Ni (28)	trans.	1.04(4)	Li et al. 1995
Ni	Ni (28)	trans.	0.82	Li et al. 1995
$CuInGaSe_2$	Ga (31)	trans.	0.98	C. S. Schnohr 2021
$CuInGaSe_2$	Ga (31)	fluor.	0.99 - 1.04	C. S. Schnohr 2021
$CuInGaSe_2$	In (49)	trans.	0.95	C. S. Schnohr 2021
$CuInGaSe_2$	In (49)	fluor.	1.05	C. S. Schnohr 2021

on octahedral sites. This is determined by the calculated shape for nearest neighbor scattering of V on octahedral and tetrahedral sites, as well as the energetic position of the X-ray absorption edge. As such the initial indications of tetrahedral coordination seem to be false. (Ghorbani, Schiller, et al. n.d.)

6.2.3 Conclusion

The conclusion from the EXAFS experiment on In_2S_3:V is that vanadium most likely substitutes octahedral indium. By fitting the EXAFS spectrum it was possible to get the V-S bond lengths of 2.47 to $2.50 \, \text{Å}$ which are in the same range of the In-S bonds in tetrahedral positions (2.46 to $2.47 \, \text{Å}$). The DFT calculations of Ghorbani, Erhart, et al. (2019) reveal a similar value of $2.49 \, \text{Å}$ for octahedral coordination so that the bond length alone is not enough to determine the V position in the In_2S_3 lattice. The estimation of the amplitude reduction factor S_0^2 value range in the NS_0^2 product is possible via a literature data comparison that indicates a tetrahedral coordination of V atoms. Improved measurements with more extensive analysis on the same samples disprove the tetragonal coordination by revealing that the V absorption edge fits to octahedral coordination for nearest neighbor scattering (Ghorbani, Schiller, et al. n.d.).

Chapter 7

Band structure changes from transition metal doping and detection of the intermediate band

7.1 Band structure

Spectroscopy methods are useful to determine the different electron transition channels in a semiconductor. The absorption of photons in the ultraviolet, visible and near infrared range is used to determine the band gaps and the transition type (direct, indirect, allowed, not allowed). After the absorption of photons with energies above the band gap, the excited electrons can recombine with the holes or defects, resulting in photoluminescence with distinct wavelengths. The temperature dependence of the PL intensity allows for the determination of activation energies of defects. Ultraviolet electron spectroscopy (UPS) is used to get an idea of the Fermi level position and changes at the surface of the sample.

7.1.1 Optical band gap

The absorption coefficient of two sample sets is measured with UV-VIS-NIR spectroscopy. The first set consists of $60\,\mathrm{nm}$ In_2S_3:TM layers on Borofloat glass as displayed in table 3.2. The second set consists of a representative fraction from the $1000\,\mathrm{nm}$ series used in the previous experiments (see table 3.1). The methods used are explained

in detail in chapter 4.9 and the determination of the best calculation method and pre-liminary analysis in appendix A.5. The best calculation method in this case was the thin-film absorption formula 4.34. The main problems that were found are interference effects in all samples, especially in the $1000\,\mathrm{nm}$ samples. Additionally, the absorption of $1000\,\mathrm{nm}$ In_2S_3 is too high to allow for higher energies above the band gap to be measured.

The measured absorption coefficients α of the pure In_2S_3 samples are displayed in figures 7.1 and 7.2. We will work with the spectrum around and below the band gap (0.6 to $2.8\,\mathrm{eV}$), where the influence of doping should occur. The differences between the $60\,\mathrm{nm}$ samples is mainly due to interference, changing the absorption around the band edge. The overall shape around the band edge is similar for all samples. The first shallow onset starts at around $2.1\,\mathrm{eV}$, which is later shown to be from an indirect transition, the second steeper onset starts at about 2.5 to $2.6\,\mathrm{eV}$ from a second, direct transition. This indicates the comparability between the $60\,\mathrm{nm}$ and $1000\,\mathrm{nm}$ samples.
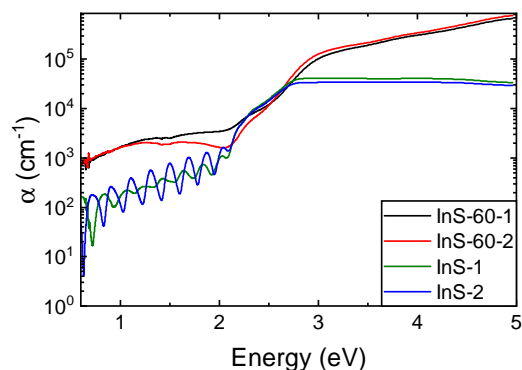
Figure 7.1: *Absorption spectra of all four In_2S_3 samples. The $1000\,\mathrm{nm}$ samples' absorption coefficient plateaus at around $2.8\,\mathrm{eV}$ due to the transmittance reaching $0\,\%$ making it impossible to detect any absorption changes.*
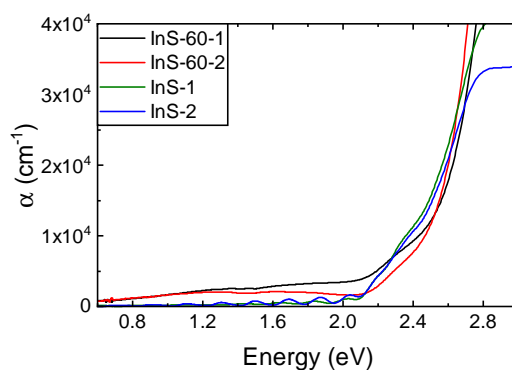
Figure 7.2: *Absorption edge of all four In_2S_3 samples. Interference effects caused by different thicknesses offset the spectra between measurements and samples especially around the band edge around 1.8 to $2.6\,\mathrm{eV}$.*

The absorption spectra of In_2S_3:V samples are shown in figures 7.3 and 7.4. We can see a clear trend of increased absorption below the band gap with increased doping. The onset of this increase is at around 1 to $1.2\,\mathrm{eV}$ for the highly doped samples. For the $60\,\mathrm{nm}$ samples, only the samples **InSV-60-1.2** and **InSV-60-3.0** have a changed spectrum shape. The indirect transition shoulder at about 2.1 to $2.5\,\mathrm{eV}$ is overlapped

by this additional absorption. For the $1000\,\mathrm{nm}$ samples, a clear increase can already be seen for **InSV-0.5**.

In contrast to the literature, there is no clear absorption peak (Lucena, Aguilera, et al. 2008; McCarthy, Weimer, Haasch, et al. 2016) which could be attributed to a discrete defect energy level or band. Instead, we have a continuous rise of the absorption, until the band-band transitions dominate the absorption. Before we analyze this further, we look at the titanium and niobium-doped samples.
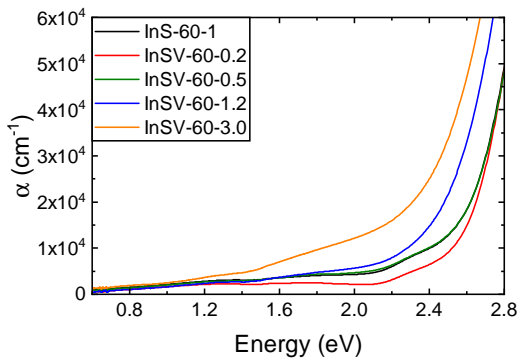
Figure 7.3: *Absorption spectra of* $60\,\mathrm{nm}$ In_2S_3:V *samples.*
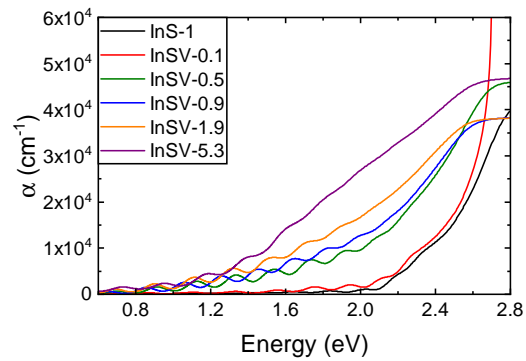
Figure 7.4: *Absorption spectra of* $1000\,\mathrm{nm}$ In_2S_3:V *samples.*

For the $60\,\mathrm{nm}$ In_2S_3:Ti samples (fig. 7.5), the change is not as visible as it is for the vanadium-doped samples. The distinguishable peak of the indirect transition vanishes again for samples **InSTi-60-1.8** and **InSTi-60-2.5**, but the overall increase is lower than for In_2S_3:V. On the other hand, the change in the $1000\,\mathrm{nm}$ samples' absorption (fig. 7.5) is showing increase absorption from about $0.8\,\mathrm{eV}$ onward which is similar to the one we can see in the In_2S_3:V samples, but has a different slope. While the absorption in the highly doped In_2S_3:V samples increase nearly linearly around the band edge, the data for the In_2S_3:Ti samples have a more exponential increase.

The absorption coefficients of the $60\,\mathrm{nm}$ In_2S_3:Nb samples in figure 7.7 look again similar to the In_2S_3:Ti samples. Unfortunately, we only have low doped $1000\,\mathrm{nm}$ samples (fig. 7.8), because of the challenging preparation. Sample **InSNb-0.2** is showing a higher absorption which does not fit the rest of the data set. Most likely a preparation deviation led to a rougher surface with more scattering. The two higher doped samples **InSNb-0.5** and **InSNb-1.5** have a weaker absorption increase compared to the $60\,\mathrm{nm}$ samples and the other dopants.
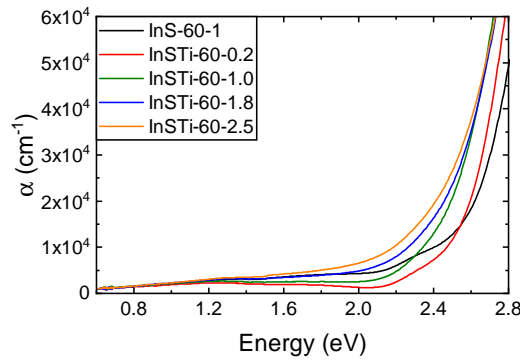
Figure 7.5: *Absorption spectra of* $60\,\text{nm}$ *In$_2$S$_3$:Ti samples.*
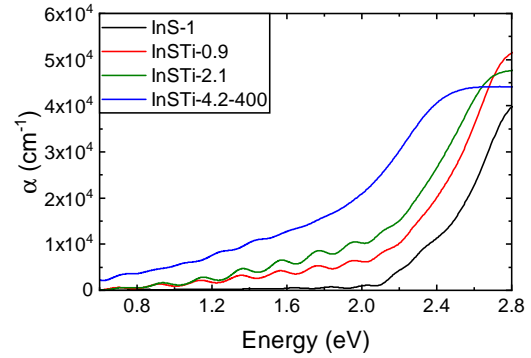
Figure 7.6: *Absorption spectra of* $1000\,\text{nm}$ *In$_2$S$_3$:Ti samples. The highest doped* $4.2\,\text{at.}\%$ *sample was grown at* $400\,°\text{C}$.
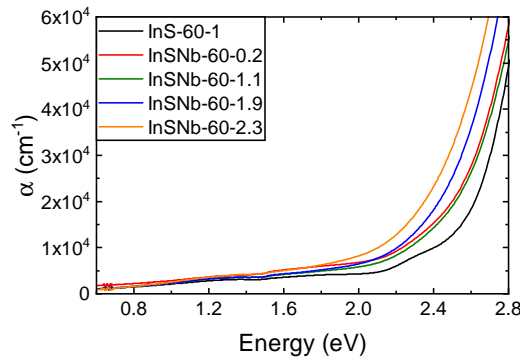
Figure 7.7: *Absorption spectra of* $60\,\text{nm}$ *In$_2$S$_3$:Nb samples.*
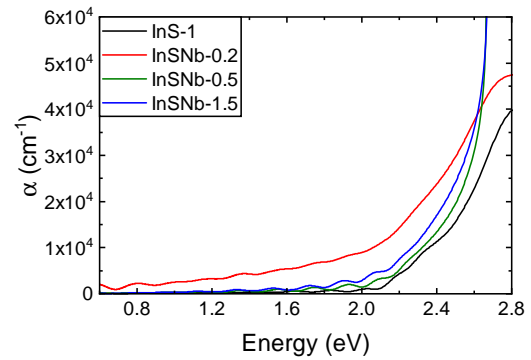
Figure 7.8: *Absorption spectra of* $1000\,\text{nm}$ *In$_2$S$_3$:Nb samples.*

The next figure 7.9 displays the derivative of the highest doped $60\,\text{nm}$ In$_2$S$_3$:TM samples. Data of the $1000\,\text{nm}$ samples are not shown, as the strong interference and detection limit makes it impossible to interpret them. The whole spectrum from 0.6 to $5\,\text{eV}$ is shown, as it allows for the identification of absorption channels. There are four peaks in total, which could be interpreted as 4 different band-band transitions. The first one is at about $2.3\,\text{eV}$, which is the first indirect transition we have looked at until now. The much larger second peak has a maximum at about $2.9\,\text{eV}$. This is where in the literature the direct optical band gap is situated (Barreau 2009). Two more maxima at 3.7 and $4.5\,\text{eV}$ are visible, which might be further band-band transitions. One phenomenon noticeable in the doped samples is the larger $FWHM$ of the peaks, merging some of them together. The peaks at 2.3 and $3.7\,\text{eV}$ are both less distinct

in the doped samples. One possible explanation is the disorder caused by the doping, which has been detected in the structural analysis (see section 5.3.2). The larger energy variation of the disordered atoms can create Urbach tails for each transition. The band edges for In_2S_3:TM are less defined than for the undoped sample, enabling lower and higher energy photons to also contribute to the absorption channels.
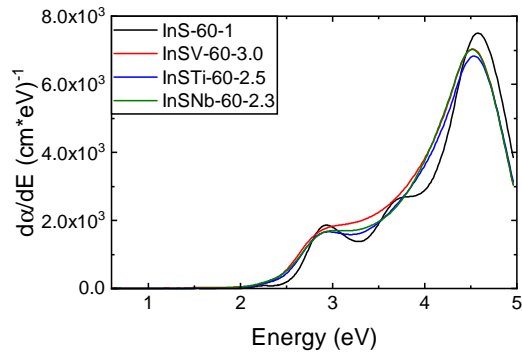
Figure 7.9: *Derivative of the absorption coefficient for the highest doped* 60 nm *samples compared to the undoped reference* **InS-60-1**.
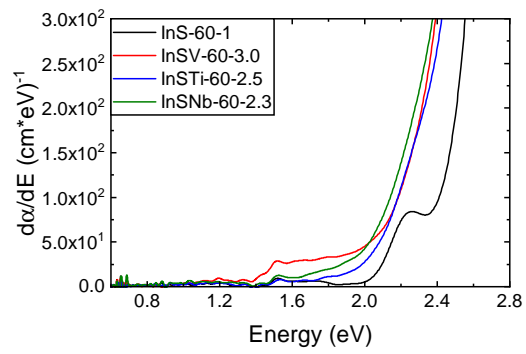
Figure 7.10: *Zoom into the derivative of the absorption coefficient for highest doped* 60 nm *samples.*

Figure 7.10 shows a zoom into the derived absorption edge. Again the disappearance of the indirect peak can be seen. More importantly only the sample containing vanadium increases noticeably below the band gap. The onsets of In_2S_3:Ti and In_2S_3:Nb are around $1.7\,\text{eV}$, most likely due to Urbach tails of the indirect and direct band gaps. For In_2S_3:V it is around $1.4\,\text{eV}$, which cannot be explained by this broadening. The very similar absorption behavior around and above the absorption edge indicates that all three doped samples are comparable in this energy region. Only the vanadium sample has a clear increase of the absorption below the band gap, beyond the Urbach tail. Unfortunately, there are a lot of measurement artifacts in this low absorption region, which make it impossible to determine the exact shape of the increase from the V-doping in this graph. The In_2S_3:Ti sample has a slightly shifted onset compared to the In_2S_3:Nb sample, which could be explained by the different doping concentrations and dopands resulting in different Urbach energies. Differing sample thicknesses and therefore interference patterns can also contribute to this.

By using the dependency of the Urbach tail (equation 4.41) we can check, if disorder is the main increase below the band gap as suspected above. Figure 7.11 displays $\ln(\alpha)$

versus energy for the highest doped $60\,\mathrm{nm}$ samples. For doped samples it is difficult to separate the Urbach tail of the lower energy indirect transition from the one of the direct transition, so only the direct transition Urbach tail is fitted for these. Table 7.1 lists the estimated Urbach energies U_E. As already suspected from the increased microstrain (see section 5.3.2), the Urbach energy of the doped samples is higher than the undoped sample. Interesting to note is that samples **InSNb-60-2.3** and **InSV-60-3.0** have nearly the same Urbach energy, although the Nb doping concentration is lower.

Nb doping seems to induce a higher disorder than Ti and V which we already noticed in figure 7.10.
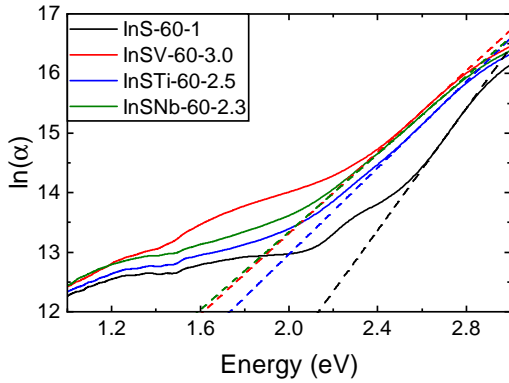
Figure 7.11: *Fit of direct transition Urbach tails for highly doped* $60\,\mathrm{nm}$ *samples. The band edge cannot be fitted due to the overlap of the direct and indirect transition.*
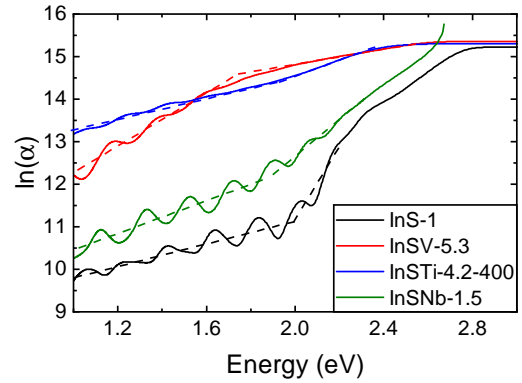
Figure 7.12: *Band edge Urbach tails of* $1000\,\mathrm{nm}$ *samples, with dashed lines as guides for the eye.*

Sample	Doping (at.%)	U_E indirect (meV)	U_E direct (meV)
InS-60-1	none	262	195
InSV-60-3.0	3.0(2)	-	293
InSTi-60-2.5	2.5(2)	-	276
InSNb-60-2.3	2.3(2)	-	305

Table 7.1: *Urbach energies for undoped and highest doped* $60\,\mathrm{nm}$ *samples.*

All of these Urbach energies are in the range of highly disordered materials (Studenyak et al. 2014). The polycrystalline nature of the material with a lot of grain bound-

aries (see section 5.1) and the large amount of intrinsic defects (see section 2.4.1 and Ghorbani and Albe 2018) can create local disturbances of the electronic band structure and increase the Urbach energy.

The data of the $1000\,\mathrm{nm}$ samples are shown in figure 7.12 and show the Urbach tails at the band edge. Because of the overlap of indirect and direct transition as well as strong interference, it is difficult to properly fit these Urbach tails. The dashed lines are mere guides to the eye to visualize the slope of the Urbach tails. One thing that can be noted here is that the Vanadium sample shows a different shape than the other ones. The slope far below the band gap is larger than at the band gap, which is opposite of the other samples, where it is the other way around. The Nb sample is closest to the undoped sample, because of the low doping concentration.

Only the V doped sample has a clear deviation below the band gap for both the $1000\,\mathrm{nm}$ and the $60\,\mathrm{nm}$ samples which supports the theory that in contrast to V samples the increase in sub-gap absorption of Ti and Nb samples comes from Urbach tails and not distinct defect states/bands inside the band gap.

Now we can calculate the absolute values of the optical band gaps of the material via Tauc plots as described with formula 4.40. From literature (Barreau 2009; Nishino et al. 1977) and our own data we know that for pure β-In_2S_3 thin film samples we have a direct transition at around 2.6 to $2.8\,\mathrm{eV}$ and an indirect transition at about 2.0 to $2.2\,\mathrm{eV}$. This means we have to do two Tauc plots for all In_2S_3 samples. Figures 7.13 and 7.14 display the Tauc plots for the indirect transitions of the four samples. Two fits are done on the steepest straight line at the absorption onset and just below the absorption onset. The energy at the intersection equals the lowest indirect optical band gap. By using two fits, the influence of interference and scattering on the result can be minimized.

The direct band gap could only be determined for the $60\,\mathrm{nm}$ samples, as the transmission of the $1000\,\mathrm{nm}$ samples in the relevant range was below the detection limit of the detector (see fig. A.31). The result is shown in figure 7.15, where only one fit is needed on the steepest straight line at the onset of the second part of the absorption to get the lowest direct optical band gap. The undoped samples all have an indirect optical band gap of about $2.1\,\mathrm{eV}$, verifying the comparability of the $60\,\mathrm{nm}$ with the $1000\,\mathrm{nm}$ samples. The direct band gap was measured to be around $2.8\,\mathrm{eV}$. Both values are as expected for PVD-grown In_2S_3 (Barreau 2009).
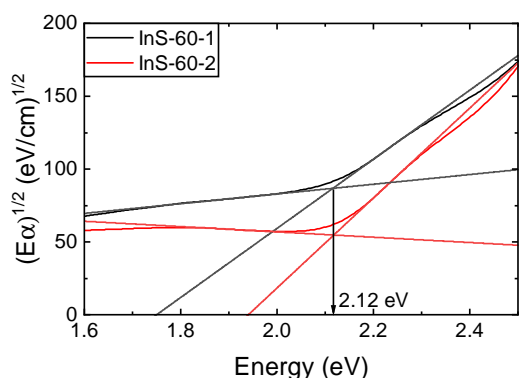
Figure 7.13: *Indirect allowed Tauc plots of the two* 60 nm *In_2S_3 samples.*
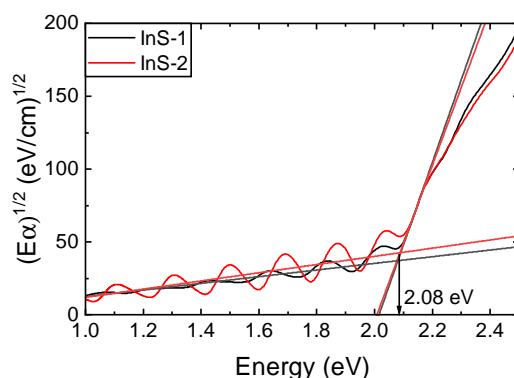
Figure 7.14: *Indirect allowed Tauc plots of the two* 1000 nm *In_2S_3 samples.*
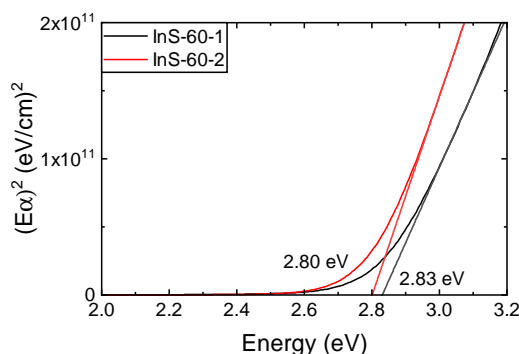
Figure 7.15: *Direct allowed Tauc plots of the two* 60 nm *In_2S_3 samples.*

It was not possible to interpret either Tauc plot for doped samples, as there were no linear parts to fit. As we have shown before, different absorption channels are overlapping at the onset of the absorption in the range 1.8 to $2.6\,\text{eV}$. This overlap can be seen best in the previously shown derivative of the absorption in figure 7.9. The comparison of these derivatives of the absorption between undoped and doped samples indicate that the band gap energies can be expected to be comparable.

7.1.2   Defect analysis

Temperature dependent photoluminescence measurements are conducted on three samples (**InS-3**, **InSV-3.9**, **InSNb-2.9**) to analyze the intrinsic and doping-induced defects. Details on the measurements can be found in chapter 4.10.

The temperature-dependent photoluminescence intensity of sample **InS-3** is shown

in figure 7.16. A broad peak is detected in the range between 600 and 1100 nm. Its intensity increases from 290 to 7 K by two orders of magnitude. A 3.5 ND filter combination reduces the high PL intensity to a manageable level.
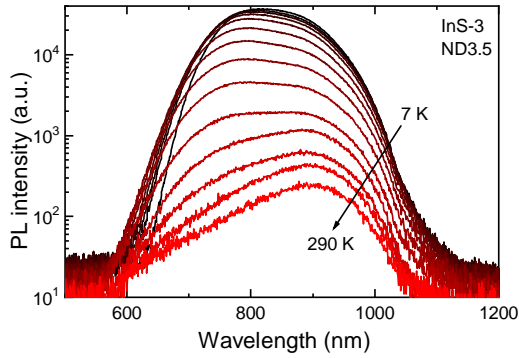
Figure 7.16: *Temperature dependent PL spectrum of the pure In_2S_3 sample **InS-3**. The PL intensity is reduced by a 3.5 ND filter combination.*
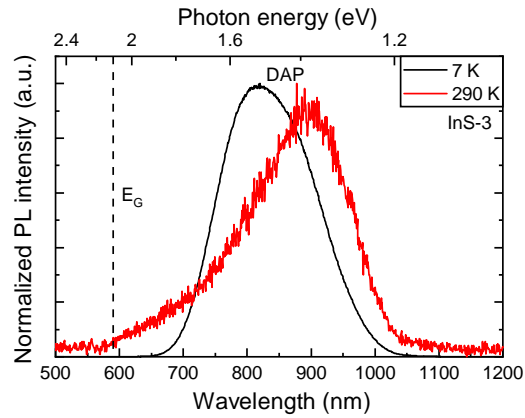
Figure 7.17: *Comparison between PL spectra at 7 and 290 K for the pure In_2S_3 sample **InS-3**. The PL intensity is reduced by a 3.5 ND filter combination.*

A peak from the band-band transition is expected at the band gap energy around 600 nm. In the comparison between the 290 and 7 K spectra (7.17) such an emission from a band-band transition is not visible. The broad peak at room temperature has about three components that, when fitted with three Gaussians, reveal peaks around 918, 830 and 680 nm at 290 K. At 7 K the lower energy peaks shift to 859 and 779 nm, while the third one is not detectable anymore. These stem from multiple donor-acceptor-pairs (DAPs) and could be assigned to $v_{S'}$-$v_{In'}$/$v_{In''}$ transitions following the notation of Ghorbani and Albe (2018). Similar assignments to v_S-v_{In} transitions have been previously made (Czaja et al. 1969; Ho 2010).

The normalized integrated intensity of the whole DAP peak is plotted versus the inverse temperature and fitted using the Arrhenius formula 4.44. The resulting fit using two activation energies is displayed in figure 7.18. More than 99 % of the intensity is depending on the activation energy of $E_{A1} = 100$ meV with a second activation energy of $E_{A2} = 40$ meV for the remaining intensity. Pai et al. (2005) have assigned the activation energy for the indium vacancy v_{In} to 100 meV. Other experiments show the indium vacancies in the same energy region (Czaja et al. 1969; Ho 2010; Jayakrishnan

et al. 2005).
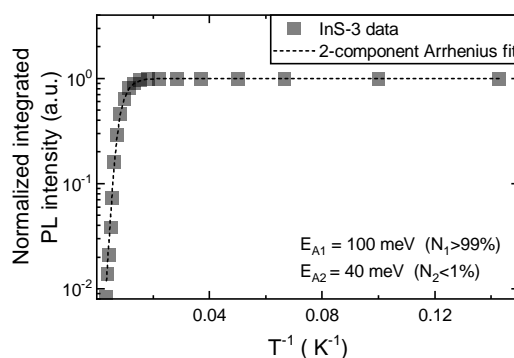
Figure 7.18: *Arrhenius analysis of the temperature dependent PL of sample **InS-3**.*

Figure 7.19 shows the temperature-dependent PL-spectra of sample **InSV-3.9**. The PL-intensity is three orders of magnitude lower than in the undoped In_2S_3 sample, considering the use of no ND filters and the same integration time. Three peaks are discernible in the spectra. The first one from the laser and filter edge at 450 to about $650\,nm$, the second peak between 700 and $900\,nm$ starts to emerge at a temperature of below $100\,K$ and a third peak between 900 and $1100\,nm$. The high intensity DAPs in the range 600 to $900\,nm$ are not visible in the V-doped sample.
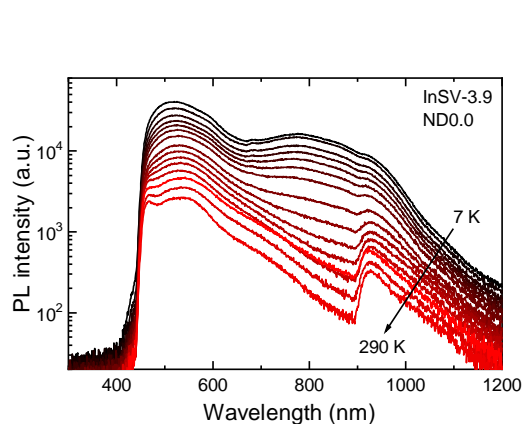
Figure 7.19: *Temperature dependent PL spectrum of sample **InSV-3.9**.*
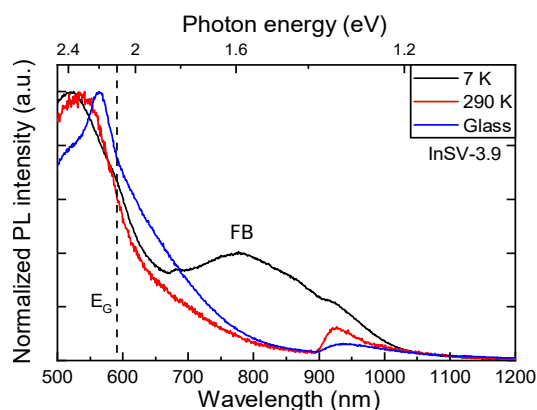
Figure 7.20: *Comparison between PL spectra at 7 and $290\,K$ of sample **InSV-3.9** and the glass substrate measured at room temperature.*

Figure 7.20 displays the spectra at 7 and $290\,K$ and compares them to a measurement of the glass substrate. The two peaks around 550 and $900\,nm$ are detectable

without the sample and seem to originate from the glass substrate, or the laser. The peak between 700 and 900 nm is only visible at lower temperatures, in contrast to the DAPs from sample **InS-3**. There is also a hint of another peak at about 680 nm.

The Arrhenius analysis of the temperature dependency of the PL intensity of the 700 to 900 nm region is shown in figure 7.21. Again two activation energies can be extracted, the dominating one at $E_{A1}^V = 35$ meV, the other at $E_{A2}^V = 10$ meV. The differing activation energy confirms that this PL peak has a different origin than the DAPs. The peak maximum of this peak is around 780 nm (1.59 eV) at 7 K, the broad DAPs in sample **InS-3** are centered around 830 nm (1.49 eV). The difference between these peaks is the activation energy of the indium vacancy v_{In} and indicates that the detected transition in sample **InSV-3.9** is a free-to-bound transition from the v_S to the valence band. Because of the lower intensity than the DAP, this transition was not detectable in the pure In_2S_3 sample. For higher temperatures the non-radiative recombination is likely hindering this transition. The calculated energy position of the v_S is 1.58 eV and fits the measured free-to-bound transition energy very well (Ghorbani and Albe 2018).
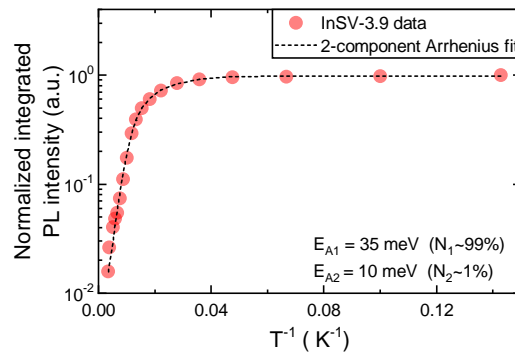
Figure 7.21: *Arrhenius analysis of the temperature dependent PL of sample **InSV-3.9**.*

Figure 7.22 shows the temperature dependency of the PL-intensity of sample **InSNb-2.9**. In this case a 2.0 ND filter is used in front of the monochromator, so the intensity is about two orders of magnitude lower than the reference sample **InS-3**. The spectra show the same DAPs as the reference, but at a much lower intensity. This is more clearly seen in figure 7.23, where the influence of the glass/laser on the spectrum is also visible. The shape of the DAPs is similar to the undoped sample **InS-1**.

The Arrhenius analysis of sample **InSNb-2.9** is shown in figure 7.24. It reveals only
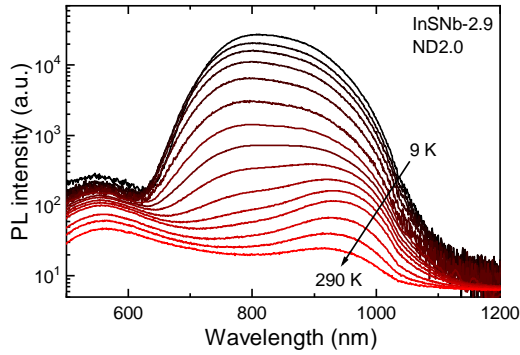
Figure 7.22: *Temperature dependent PL spectrum of sample **InSNb-2.9**. The PL intensity is reduced by a 2.0 ND filter.*
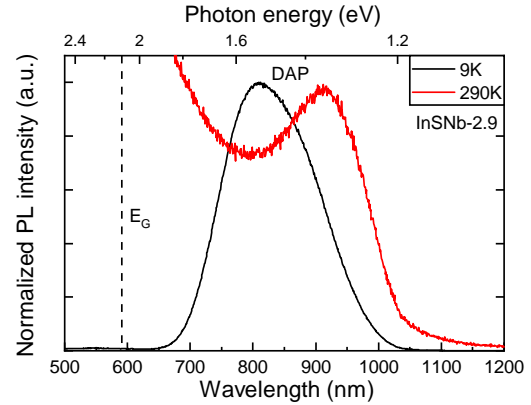
Figure 7.23: *Comparison between PL spectra at 9 and $290\,\mathrm{K}$ of sample **InSNb-2.9**.*

one activation energy of $E_{A1} = 100\,\mathrm{meV}$, which is the same as for sample **InS-3**.
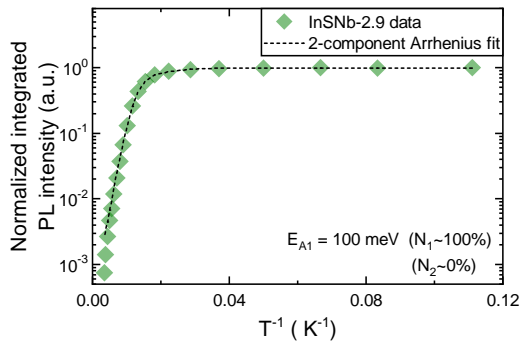
Figure 7.24: *Arrhenius analysis of the temperature dependent PL of sample **InSNb-2.9**.*
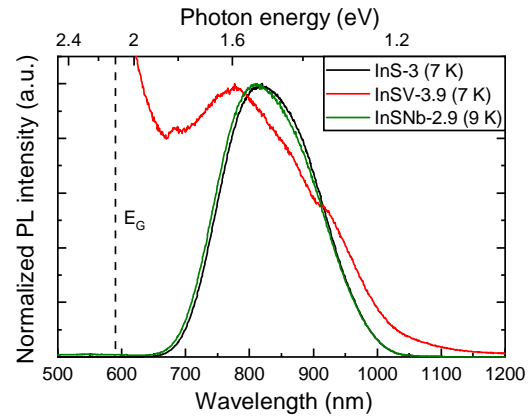
Figure 7.25: *Comparison between low temperature PL spectra of the undoped and doped samples.*

7.1.3   Conclusion

Absorption spectroscopy revealed the co-evaporated In_2S_3 to have an indirect band gap of about $2.1\,\mathrm{eV}$ with a direct transition of around $2.8\,\mathrm{eV}$. Both values are consistent with other PVD-grown In_2S_3 (Barreau 2009). Only In_2S_3:V samples displayed an additional absorption component that could not be explained with an Urbach tail.

The band-band transition of 2.1 is not visible in any of the PL measurements. We know from our experiments as well as literature (Ghorbani and Albe 2018) that a lot of defects can form with energy positions below the conduction band. One hypothesis to explain the missing band-band transition is the fast trapping of free-charge carriers in the defects close to the conduction band. The very high intensity of the DAP transition points in this direction. The electrons seem to transition to the donor defects non-radiatively, from where they recombine with the acceptors radiatively. In case of hyperdoping, these DAP transitions become suppressed. The TM-doping very likely increases the amount of SRH-recombination, so many electrons recombine non-radiatively with holes in the valence band for these samples. This is important to know for the creation of In_2S_3 devices, as the charge carrier separation would have to be very fast to be able to utilize the photo-generated electrons in the conduction band, if this interpretation is correct.

No new radiative recombination channel was detected in the hyperdoped samples that could be attributed to an IB. As such, other methods are needed to confirm the existence and position of the transition metal defect band or states.

7.2 Intermediate band

In this section we use UV-VIS-NIR absorption spectroscopy and two-photon photoluminescence to detect the intermediate band.

7.2.1 Single photon absorption experiment

The analysis of the absorption experiment revealed measurement and sample artifacts in the same spectrum range where the absorption of the higher energy IB transition would be like interference and the Urbach tail. Instead of analyzing one sample, we can look at the absolute and relative change between two samples to reduce said artifacts. As shown in the appendix section A.7, it should be possible to isolate the effect of doping on the absorption coefficient by calculating the absolute or relative difference between a doped and an undoped sample. In our non-ideal case we have to consider the effects on the spectrum mentioned above as well. Since the measurement artifacts occur in all measurements, we need two samples of the same thickness to eliminate in-

terference and a similar doping and Urbach energy to reduce the Urbach tails. All this is true for the highest doped $60\,\text{nm}$ vanadium and niobium samples. The Urbach energies have already been determined to be matching quite well (see figure 7.11 and table 7.1). Figure 7.26 shows the measured reflectance and matching interference extrema for both samples which validates the choice.
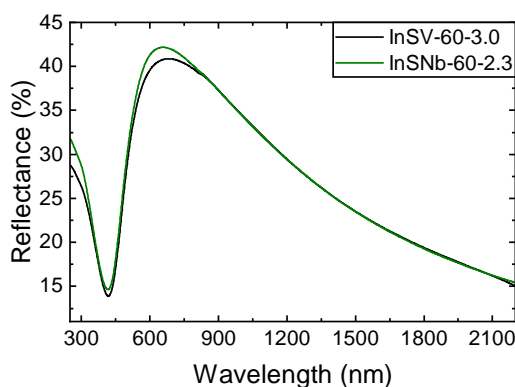
Figure 7.26: *Comparison of the reflectance of the highest doped $60\,\text{nm}$ V and Nb samples showing matching interference patterns.*

The change of the $60\,\text{nm}$ In$_2$S$_3$:V spectrum compared to the In$_2$S$_3$:Nb spectrum is shown in figure 7.27. The relative difference spectrum is slightly shifted, which was predicted by the calculation shown in figure A.37. Both spectra have a distinct peak between about 1.2 to $2.5\,\text{eV}$, where the absorption is more than $50\,\%$ higher than the reference. For higher energies the V-doped sample has an increased absorption of about 5 to $10\,\%$. Below $1\,\text{eV}$ another peak seems to be visible. The problem is that this peak is very small (as seen in the absolute difference), very noisy, and not reproducible in $1\,\text{at.}\%$ samples (see fig. A.38). Additionally, there is no other evidence of another absorption channel in any of the spectra, so this peak is most likely a measurement artifact amplified by the relative difference calculation.

Since we now have the vanadium defect absorption, we can try to extract an energy position of this defect as well. Figures 7.28 and 7.29 show the indirect and direct Tauc-plots of the V-spectrum calculated from both the absolute and relative difference between the V and Nb sample. The shift of the relative difference is again visible here. While the indirect allowed Tauc-plot does not show a clear linear dependency, the direct allowed one does. Fitting the first onset of both spectra results in two values
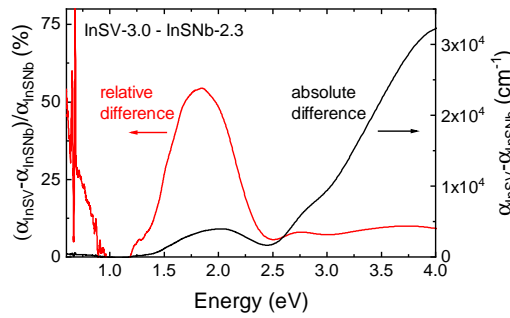
Figure 7.27: *Absolute and relative difference between the absorption spectra of samples **InSV-3.0** and **InSNb-2.3**. The absorption of the V defect is clearly visible with a maximum at about $1.8\,\mathrm{eV}$.*

$1.43\,\mathrm{eV}$ for the relative difference and $1.54\,\mathrm{eV}$ for the absolute difference.
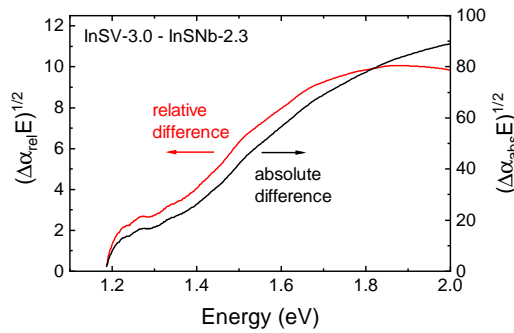
Figure 7.28: *Indirect allowed Tauc plots of the V-defect spectrum obtained from the absolute and relative difference. No clear linear dependency is visible.*
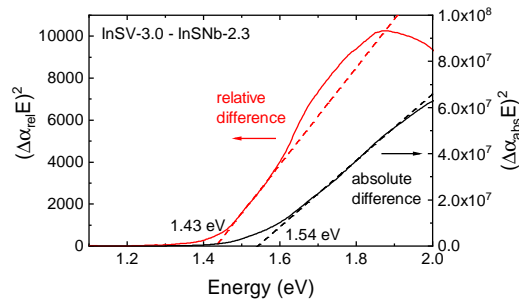
Figure 7.29: *Direct allowed Tauc-plots of the V-defect spectrum obtained from the absolute and relative difference with fits to linear parts of the Tauc-plot.*

7.2.2   Two photon-photoluminescence experiments

To get more information about the vanadium defect band we can extend the photoluminescence experiment by using two lower energy lasers to excite electrons via the defect band. By comparing doped and undoped samples it is possible to confirm the existence of energy states or an energy band inside the band gap and find the most likely position of said band.

In our case we chose a continuous $820\,\mathrm{nm}$ ($1.51\,\mathrm{eV}$) laser diode with $40\,\mathrm{mW}$ power on the sample and a pulsed $1625\,\mathrm{nm}$ ($0.76\,\mathrm{eV}$) laser diode with $80\,\mathrm{mW}$ power ($40\,\mathrm{mW}$

effective). The photoluminescence spectrum is measured around the band gap using a lock-in amplifier tuned to the pulse frequency of the 1625 nm laser. This way the electrons excited solely by the high energy laser will not count towards the detected two photon-photoluminescence (see 7.30). Since the low energy laser can only excite electrons over one of the three band-band transitions, the measured photoluminescence from the E_C-E_V transition has to involve the excitation via intermediate states or a band within the band gap.
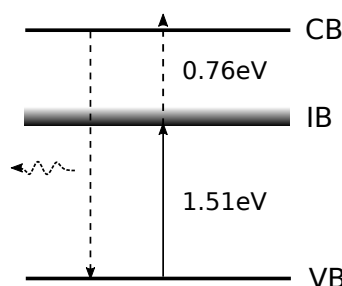
Figure 7.30: Diagram of the two photon PL experiment (displayed with the IB closer to the CB). The lock in amplifier is tuned to the pulse of the 1625 nm *(0.76 eV) laser, so that PL stemming only from the* 820 nm *(1.51 eV) laser is not detected.*

We know from the other experiments that the samples have defects at similar energies where the intermediate band in In$_2$S$_3$:V could be. It is therefore vital to do the same experiment with reference samples to limit the possibility that the electrons are excited via the defects. Measurements were conducted on samples **InS-3**, **InSV-3.9**, **InSV-0.5-2** and **InSNb-2.9**.

Figures 7.31 and 7.32 display the result of the measurements conducted at 10 K. The reference sample **InS-3**, as well as sample **InSNb-2.9** (not shown) do not display any PL involving the low energy laser. Electrons do not seem to be excited into the CB via intrinsic or Nb-induced defects. The V-doped samples **InSV-3.9** and even the low doped **InSV-0.5-2** display clear band-band recombination at the expected positions around and above the band edge. The V incorporation allows for the generation of free charge carriers using photons with energies below the band gap.

This transition via the intermediate states was not possible using just one of the two lasers, both were necessary to get a PL response.

Sample **InSV-3.9** (fig. 7.31) was measured on smooth sample areas due to constraints concerning parallel photoconductivity measurements. As a result strong in-

terference and inhomogenic thickness changes the PL spectrum between the two measured positions. When comparing both spectra it can be assumed that there are about two transitions with one between about 1.8 and $2.3\,\mathrm{eV}$ and one between about 2.3 and $2.8\,\mathrm{eV}$. The expected band-band transitions for undoped In_2S_3 at room temperature obtained from the absorption are at 2.1 and $2.8\,\mathrm{eV}$ (see section 7.1.1). Considering the lower temperature of $10\,\mathrm{K}$ and the Urbach tails also observed in the absorption spectra, it is likely that the two transitions are in fact the indirect and direct band-band transitions.

The lower doped sample **InSV-0.5-2** (fig. 7.32) was measured on the rough part of the sample, so no interference should disturb the shape of the spectrum. The PL response is much lower in intensity, so probably only the highest intensity response could be detected. It is only one distinct peak visible which fits to the indirect band-band transition, again considering the low temperature of $10\,\mathrm{K}$.
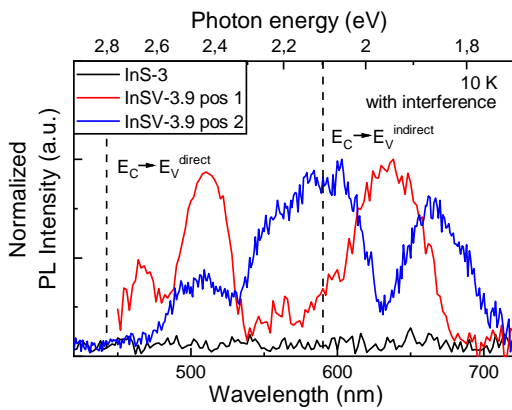
Figure 7.31: *Comparison of PL responses of undoped sample* **InS-3** *and V-doped sample* **InS-3.9** *at* $10\,\mathrm{K}$ *when exciting with two lasers with below band gap energies (*$1.51\,\mathrm{eV}$ *continuous and* $0.76\,\mathrm{eV}$ *chopped/locked-in). Two measurements were done on defferent positions on the smooth parts of sample* **InS-3.9***. The differences come from interference and different thicknesses at both positions. Also displayed are the expected band-band transition energies at room temperature.*
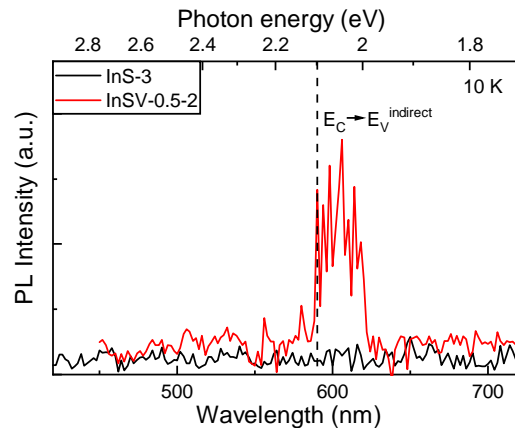
Figure 7.32: *Comparison of PL responses of undoped sample* **InS-3** *and V-doped sample* **InS-0.5-2** *at* $10\,\mathrm{K}$ *when exciting with two lasers with below band gap energies (*$1.51\,\mathrm{eV}$ *continuous and* $0.76\,\mathrm{eV}$ *chopped/locked-in). This measurement was done on the rough part of the sample, so no interference is expected. Also displayed is the expected band-band transition energy at room temperature.*

Initial photoconductivity experiments done at $50\,\mathrm{K}$ on the same setup as the two

photon PL experiments show an increased conductivity of In_2S_3:V samples when illuminated with the $1625\,nm$ ($0.76\,eV$) laser. The same increase was not detected in the undoped sample. This might be an indication that the IB is located in the upper half of the band gap, allowing electrons to be excited into the CB from the IB. More thorough photoconductivity investigations are needed to confirm this first result. Other authors place the IB in both the upper (Lucena, Conesa, et al. 2014) and the lower (Ghorbani, Erhart, et al. 2019; McCarthy, Weimer, Haasch, et al. 2016) part of the band gap.

7.2.3 Conclusion

We already determined the band gap of pure In_2S_3 to be at $2.1\,eV$ and saw no indication that the gap changes a lot with doping, except for the increased Urbach tail. The absorption measurements also showed one IB transition at 1.4 to $1.5\,eV$, placing the second transition at 0.6 to $0.7\,eV$. The lower energy IB transition was not detected which leads to the conclusion that the IB can be expected to be filled (Ghorbani, Erhart, et al. 2019; McCarthy, Weimer, Haasch, et al. 2016) or to be empty (Ghorbani, Schiller, et al. n.d.), but not half-filled, as would be preferred for photovoltaic application (Strandberg and Reenaas 2009).

Table 7.2 displays a comparison of the band gap and IB positions from various publications. These publications are mostly agreeing to a band gap of around $2\,eV$, as measured here. Ghorbani, Erhart, et al. (2019) predict lower band gaps if an octahedral V_{In}^- substitution is the cause for the IB. The position of the IB is slightly changing from one publication to another, but both absorption spectroscopy experiments (Lucena, Aguilera, et al. 2008; McCarthy, Weimer, Haasch, et al. 2016) show it in the range of 0.6 to $0.8\,eV$ above the VBM. The work of Ghorbani, Erhart, et al. (2019) considered several configurations of V ionization and positioning inside the In_2S_3 lattice, which all result in different IB positions, or even no IB at all. This means that it is possible to have more than one defect state contributing to the IB. The results obtained from our measurements lie well within the results of the other experiments.

Table 7.2: *Band gap and IB position for In$_2$S$_3$:V according to various publications.*

Band gap (eV)	VB-IB (eV)	IB-CB (eV)	doping (at.%)	method	source
2.1	1.4-1.5	0.6-0.7	1-3	absorption	this work
$\sim$2.0	$\sim$0.7	$\sim$1.5	3	absorption + DFT	Lucena, Aguilera, et al. 2008
2.1	1.65	0.45	5?	PLE + DFT	Lucena, Conesa, et al. 2014
$\sim$2.1	$\sim$0.8	$\sim$1.3	3-9	absorption	McCarthy, Weimer, Haasch, et al. 2016
1.62	0.28	1.34	1.25	β-In$_2$S$_3$ HSE: V$^-_{\text{In}^{16h}}$	Ghorbani, Erhart, et al. 2019
1.95	0.13	1.82	5	β-In$_2$S$_3$ HSE: V$^-_{\text{In}^{16h}}$	Ghorbani, Erhart, et al. 2019
2.6	1.82	0.34	1.9	α-In$_2$S$_3$ HSE: V$_{\text{In}^{16h}}$	Ghorbani, Schiller, et al. n.d.

Chapter 8

General conclusion and discussion

V, Ti and Nb were successfully incorporated into the In$_2$S$_3$ structure using physical co-evaporation.   Physical co-evaporation of In and V, Ti or Nb in a sulfur rich atmosphere onto glass substrates with temperatures between 300 and 500 °C allowed the growth of highly textured polycrystalline In$_2$S$_3$ thin-films with doping concentrations of up to 6 at.% (section 5.1). Hyperdoping was made possible with a modified electron beam source suited to evaporate low vapor pressure transition metals in a corrosive sulfur environment (section 3.2). The incorporation success was determined by the non-detection of secondary phases in XRD, GIWAXS and Raman measurements (section 5.2.2), the measurable decrease in lattice constants of the In$_2$S$_3$ lattice (section 5.3.1) and the predominant bonding to sulfur (section 6.1). Initial results were published in Wägele et al. (2017) followed up by a more detailed study in Ghorbani, Schiller, et al. (n.d.). This verification of incorporation is necessary to be sure that measurements are not distorted by secondary phases or metal clusters.

The incorporation of V, Ti and Nb into In$_2$S$_3$ was shown to increase defect densities and induce a phase transition from the β- to the α-phase.   We have confirmed that hyperdoping induced structural changes cannot be neglected. Increased FWHM of XRD reflexes could be attributed to a doping induced crystal microstrain (section 5.3.2). The detected Urbach tails in absorption spectra of doped samples were larger than in undoped samples, indicating an increased amount of defect levels near the band edges (sections 7.1.1). The photoluminescence intensity of hyperdoped samples decreased by up to three orders of magnitude which might be attributed to a strong

increase in non-radiative recombination caused by deep defects (section 7.1.2). Initial results were published in Wägele et al. (2017) followed up by a more detailed study in Ghorbani, Schiller, et al. (n.d.).

The stable phase of stoichiometric In_2S_3 at room temperature is β-In_2S_3. This β-phase has also been assumed in experimental and theoretical work (Ghorbani, Erhart, et al. 2019; Lucena, Aguilera, et al. 2008; Lucena, Conesa, et al. 2014; McCarthy, Weimer, Haasch, et al. 2016; Tapia et al. 2016). Using GIWAXS it was possible to properly distinguish the $\alpha-$ from the β-phase and observe an order-disorder transition from β-In_2S_3 to α-In_2S_3 induced by hyperdoping. The samples with doping concentrations of more than $\sim 2\,at.\%$ (likely dependent on the dopant) are present as α-In_2S_3, while lower concentrations lead to a bimorphism of the $\beta-$ and α-phase. This confirms observations done on In_2S_3:Fe by Chen et al. (2013).

New theoretical research shows that doping α-In_2S_3 with $1.9\,at.\%$ V on octahedral sites would still form an IB. But the IB states are empty and it merges with the CB at higher doping concentrations (Ghorbani, Schiller, et al. n.d.).

The position of V in the host lattice was found to likely be on octahedral In. For the first time it was attempted to determine the exact position of V atoms in the In_2S_3:V lattice via EXAFS measurements. The material's properties depend strongly on the position of the dopants in the host lattice as shown by Ghorbani, Erhart, et al. (2019). This knowledge is therefore crucial to compare the experiments to theoretical work. The initial analysis of the amplitude reduction factor yielded an indication of a coordination number of 4 for V-S bonds (section 6.2.2). Just before finalizing this thesis, new measurements and a more thorough analysis of the EXAFS results became available. This did not confirm the tetrahedral coordination, but instead shows that the X-ray absorption shape better fits to an octahedral coordination (Ghorbani, Schiller, et al. n.d.). This validates the DFT calculations that assumed octahedral coordination of the transition metals (Ghorbani, Barragan-Yani, et al. 2020; Ghorbani, Erhart, et al. 2019; Lucena, Conesa, et al. 2014; Palacios et al. 2008).

The existence of intermediate energy levels in physically co-evaporated In_2S_3:V was demonstrated for the first time. Additional absorption was detected in the band gap of In_2S_3:V using optical spectroscopy (section 7.2.1). The absorption energy

was determined to be in the range of about 1.4 to $1.5\,\mathrm{eV}$. Taking the measured band gap of $2.1\,\mathrm{eV}$, the second transition is expected to be around 0.6 to $0.7\,\mathrm{eV}$. This second transition is not detected which could be interpreted as filled intermediate states in the n-type In_2S_3:V in accordance with McCarthy, Weimer, Haasch, et al. (2016). But as shown in Ghorbani, Schiller, et al. (n.d.), α-In_2S_3 hyperdoped with V will probably form an empty IB closer to the CB. This means, that it is more likely that the detected transition is the VB-IB transition into the empty IB.

In a low temperature two photon-photoluminescence experiment it was possible to verify the excitation of electrons into these intermediate states and then out into the conduction band (section 7.2.2). This two photon-transition was only observable in In_2S_3:V samples.

While the detection of intermediate states in transition metal-doped In_2S_3 has already been done (Chen et al. 2013; Ho 2011; Lucena, Conesa, et al. 2014; McCarthy, Weimer, Haasch, et al. 2016; Tapia et al. 2016), it is the first time that co-evaporation has been used to fabricate very pure In_2S_3:V samples and to correlate the structural properties to the existence of intermediate states. While no IB was detected in In_2S_3:Ti and In_2S_3:Nb, it was difficult to achieve the same doping concentrations as with vanadium. To form an IB the doping concentration needs to exceed a certain concentration, depending on dopant and lattice position (Ghorbani, Barragan-Yani, et al. 2020). It is possible that higher concentrations on the correct lattice positions are needed to form IBs in In_2S_3:Ti and In_2S_3:Nb.

Bibliography

Abou-Ras, D. et al. (Apr. 2005). "Microstructural and chemical studies of interfaces between $Cu(In,Ga)Se_2$ and In_2S_3 layers". In: *Journal of Applied Physics* 97.8, p. 084908. DOI: 10.1063/1.1863454.

Allmann, R. et al. (1964). "Die Kristallstruktur des Patronits $V(S_2)_2$". In: *Die Naturwissenschaften* 51.11, pp. 263–264. DOI: 10.1007/BF00638454.

Anderson, P. W. (Mar. 1958). "Absence of Diffusion in Certain Random Lattices". In: *Physical Review* 109.5, pp. 1492–1505. DOI: 10.1103/PhysRev.109.1492.

Asikainen, T., M. Ritala, and M. Leskelä (1994). "Growth of In_2S_3 thin films by atomic layer epitaxy". In: *Applied Surface Science* 82-83, pp. 122–125. ISSN: 0169-4332. DOI: 10.1016/0169-4332(94)90206-2.

Balzar, D. and S. Popović (Feb. 1996). "Reliability of the Simplified Integral-Breadth Methods in Diffraction Line-Broadening Analysis". In: *Journal of Applied Crystallography* 29.1, pp. 16–23. DOI: 10.1107/S0021889895008478.

Bark, Hunyoung et al. (2018). "Large-area niobium disulfide thin films as transparent electrodes for devices based on two-dimensional materials". In: *Nanoscale* 10.3, pp. 1056–1062. DOI: 10.1039/C7NR07593F.

Barreau, N. (2009). "Indium sulfide and relatives in the world of photovoltaics". In: *Solar Energy* 83.3, pp. 363–371. DOI: 10.1016/j.solener.2008.08.008.

Barreau, N., J. C. Bernède, C. Deudon, et al. (2002). "Study of the new β-In_2S_3 containing Na thin films Part I: Synthesis and structural characterization of the material". In: *Journal of Crystal Growth* 241.1-2, pp. 4–14. DOI: 10.1016/S0022-0248(02)01242-3.

Barreau, N., J. C. Bernède, and S. Marsillac (2002). "Study of the new β-In_2S_3 containing Na thin films. Part II: Optical and electrical characterization of thin films". In: *Jour-*

nal of Crystal Growth 241.1-2, pp. 51–56. DOI: 10.1016/S0022-0248(02)01243-5.

Barreau, N., S. Marsillac, J. C. Bernède, and L. Assmann (2003). "Evolution of the band structure of β-In$_2$S$_{3-3x}$O$_{3x}$ buffer layer with its oxygen content". In: *Journal of Applied Physics* 93.9, p. 5456. ISSN: 0021-8979. DOI: 10.1063/1.1565823.

Barreau, N., S. Marsillac, J. C. Bernède, T. Ben Nasrallah, et al. (2001). "Optical Properties of Wide Band Gap Indium Sulphide Thin Films Obtained by Physical Vapor Deposition". In: *Physica Status Solidi (a)* 184.1, pp. 179–186. ISSN: 0031-8965. DOI: 10.1002/1521-396X(200103)184:1{\textless}179::AID-PSSA179{\textgreater}3.0.CO;2-6.

Barreau, N., A. Mokrani, et al. (2009). "Bandgap properties of the indium sulfide thin-films grown by co-evaporation". In: *Thin Solid Films* 517.7, pp. 2316–2319. ISSN: 0040-6090. DOI: 10.1016/j.tsf.2008.11.001.

Beaucarne, G. and M. A. Green (Apr. 2003). "A modified Shockley–Read–Hall theory including radiative transitions". In: *Solid-State Electronics* 47.4, pp. 685–689. DOI: 10.1016/S0038-1101(02)00316-7.

Bensch, W. and J. Koy (June 1993). "Structure of hexagonal V$_3$S$_4$ determined at three different temperatures". In: *Acta Crystallographica Section C Crystal Structure Communications* 49.6, pp. 1133–1135. DOI: 10.1107/S0108270192012368.

Bodnar, I. V. and V. A. Polubok (2014). "Optical Properties of In$_2$S$_3$ Thin Films". In: *Journal of Applied Spectroscopy* 81.5, pp. 881–884. ISSN: 0021-9037. DOI: 10.1007/s10812-014-0022-7.

Bremner, Stephen P., Michael Y. Levy, and Christiana B. Honsberg (Apr. 2008). "Limiting efficiency of an intermediate band solar cell under a terrestrial spectrum". In: *Applied Physics Letters* 92.17, p. 171110. DOI: 10.1063/1.2907493.

Byrnes, Steven J. (2016). *Multilayer optical calculations*. URL: http://arxiv.org/pdf/1603.02720v3.

Caglioti, G., A. Paoletti, and F. P. Ricci (Oct. 1958). "Choice of collimators for a crystal spectrometer for neutron diffraction". In: *Nuclear Instruments* 3.4, pp. 223–228. DOI: 10.1016/0369-643X(58)90029-X.

Chen, Ping et al. (2013). "Fe-substituted indium thiospinels: New intermediate band semiconductors with better absorption of solar energy". In: *Journal of Applied Physics* 113.21, p. 213509. ISSN: 0021-8979. DOI: 10.1063/1.4808352.

Chong, Laiyuan et al. (Mar. 2019). "Raman Study of Strain Relaxation from Grain Boundaries in Epitaxial Graphene Grown by Chemical Vapor Deposition on SiC". In: *Nanomaterials* 9.3, p. 372. DOI: 10.3390/nano9030372.

Coyle, G. J. et al. (Jan. 1980). "XPS studies of ion-bombardment damage of transition metal sulfides". In: *Journal of Electron Spectroscopy and Related Phenomena* 20.2, pp. 169–182. DOI: 10.1016/0368-2048(80)85014-6.

Czaja, W. and L. Krausbauer (1969). "Photoluminescence of $CdIn_2S_4$ and Mixed Crystals with In_2S_3 as Related to Their Structural Properties". In: *physica status solidi (b)* 33.1, pp. 191–199. ISSN: 0370-1972. DOI: 10.1002/pssb.19690330116.

Dash, Jatis K. et al. (Aug. 2015). "A Method Toward Fabricating Semiconducting 3R-NbS_2 Ultrathin Films". In: *The Journal of Physical Chemistry C* 119.34, pp. 19763–19771. DOI: 10.1021/acs.jpcc.5b04057.

Deslattes, R. D. et al. (2005). *X-ray Transition Energies (version 1.2)*. Online, Accessed: 2021/05/19. Originally published as: R.D. Deslattes, E.G. Kessler, Jr., P. Indelicato, L. de Billy, E. Lindroth, and J. Anton, "X-ray transition energies: new approach to a comprehensive evaluation," Rev. Mod. Phys. 75, 35-99 (2003). DOI: 10.18434/T4859Z. URL: http://physics.nist.gov/XrayTrans.

Diehl, R., C. D. Carpentier, and R. Nitsche (1976). "The crystal structure of γ-In_2S_3 stabilized by As or Sb". In: *Acta Crystallographica Section B Structural Crystallography and Crystal Chemistry* 32.4, pp. 1257–1260. ISSN: 0567-7408. DOI: 10.1107/S0567740876005062.

Ekins-Daukes, N. J. and T. W. Schmidt (Aug. 2008). "A molecular approach to the intermediate band solar cell: The symmetric case". In: *Applied Physics Letters* 93.6, p. 063507. DOI: 10.1063/1.2970157.

England, W. B., S. H. Liu, and H. W. Myron (May 1974). "Electronic structure of VS". In: *The Journal of Chemical Physics* 60.10, pp. 3760–3766. DOI: 10.1063/1.1680816.

Ettema, A. R. H. F. and C. Haas (June 1993). "An X-ray photoemission spectroscopy study of interlayer charge transfer in some misfit layer compounds". In: *Journal of Physics: Condensed Matter* 5.23, pp. 3817–3826. DOI: 10.1088/0953-8984/5/23/008.

Fang, Yutao et al. (July 2015). "Investigation of temperature-dependent photoluminescence in multi-quantum wells". In: *Scientific Reports* 5.1. DOI: 10.1038/srep12718.

Feng, Xiaoyang et al. (June 2017). "Hydrothermal synthesis of pyramid-like In_2S_3 film for efficient photoelectrochemical hydrogen generation". In: *International Journal of Hydrogen Energy* 42.22, pp. 15085–15095. DOI: 10.1016/j.ijhydene.2017.04.283.

Fermin, José R., Carlos Durante Rincón, and Jaime A. Castro (2019). "Microstructural Analysis of $AgIn_5VI_8$ (VI: S, Se, Te) Ternary Semiconductors by X-Ray Diffraction". In: *Materials Research* 22.5. DOI: 10.1590/1980-5373-MR-2019-0752.

Ghorbani, Elaheh and Karsten Albe (2018). "Intrinsic point defects in β-In_2S_3 studied by means of hybrid density-functional theory". In: *Journal of Applied Physics* 123.10, p. 103103. DOI: 10.1063/1.5020376.

Ghorbani, Elaheh, Daniel Barragan-Yani, and Karsten Albe (Aug. 2020). "Towards intermediate-band photovoltaic absorbers: theoretical insights on the incorporation of Ti and Nb in In_2S_3". In: *npj Computational Materials* 6.1. DOI: 10.1038/s41524-020-00350-2.

Ghorbani, Elaheh, Paul Erhart, and Karsten Albe (2019). "New insights on the nature of impurity levels in V-doped In_2S_3: why is it impossible to obtain a metallic intermediate band?" In: *Journal of Materials Chemistry A* 7.13, pp. 7745–7751. ISSN: 2050-7488. DOI: 10.1039/C9TA01629E.

Ghorbani, Elaheh, Martin Schiller, et al. (n.d.). "Elucidating the local structure of V substitutes in In_2S_3 as potential intermediate band material by X-ray absorption spectroscopy and first principles calculations". In: *Submitted* ().

Glatzel, Pieter, Grigory Smolentsev, and Grant Bunker (Nov. 2009). "The electronic structure in 3d transition metal complexes: Can we measure oxidation states?" In: *Journal of Physics: Conference Series* 190, p. 012046. DOI: 10.1088/1742-6596/190/1/012046.

Goedecke, T. and K. Schubert (1985). "On the phase diagram InS_M". In: *Zeitschrift fuer Metallkunde* 76.5, pp. 358–364. ISSN: 0044-3093. URL: https://inis.iaea.org/search/searchsinglerecord.aspx?recordsFor=SingleRecord&RN=17001868.

Gubanov, V. A. et al. (Feb. 1988). *Raman scattering in $CdIn_2S_4$ monocrystals and phonon modes in some $A^2B_2^3C_4^6$ spinel semiconductors.*

Hall, R. N. (1951). "Germanium rectifier characteristics". In: *Physical Review* 83.1, p. 228.

Harris, G. B. (Jan. 1952). "X. Quantitative measurement of preferred orientation in rolled uranium bars". In: *The London, Edinburgh, and Dublin Philosophical Magazine and Journal of Science* 43.336, pp. 113–123. DOI: 10.1080/14786440108520972.

He, Sheng-Gui et al. (May 2007). "Formation, detection, and stability studies of neutral vanadium sulfide clusters". In: *The Journal of Chemical Physics* 126.19, p. 194315. DOI: 10.1063/1.2730828.

Ho, Ching-Hwa (2010). "Growth and characterization of near-band-edge transitions in β-In$_2$S$_3$ single crystals". In: *Journal of Crystal Growth* 312.19, pp. 2718–2723. DOI: 10.1016/j.jcrysgro.2010.06.018.

— (2011). "Enhanced photoelectric-conversion yield in niobium-incorporated In$_2$S$_3$ with intermediate band". In: *Journal of Materials Chemistry* 21.28, p. 10518. ISSN: 0959-9428. DOI: 10.1039/c1jm10731c.

— (2012). "The study of below and above band-edge imperfection states in In$_2$S$_3$ solar energy materials". In: *Physica B: Condensed Matter* 407.15, pp. 3052–3055. ISSN: 0921-4526. DOI: 10.1016/j.physb.2011.08.046.

Huang, Wenjuan et al. (2017). "Controlled Synthesis of Ultrathin 2D β-In$_2$S$_3$ with Broadband Photoresponse by Chemical Vapor Deposition". In: *Advanced Functional Materials* 27.36, p. 1702448. ISSN: 1616-301X. DOI: 10.1002/adfm.201702448.

Izadneshan, H. and V. F. Gremenok (2014). "Influence of Annealing on the Optical Parameters of In$_2$S$_3$ Thin Films Produced by Thermal Evaporation". In: *Journal of Applied Spectroscopy* 81.2, pp. 293–296. ISSN: 0021-9037. DOI: 10.1007/s10812-014-9924-7.

Jawinski, Tanja et al. (Mar. 2018). "Properties of In$_2$S$_3$-Based pin-Heterojunctions". In: *physica status solidi (a)* 215.11, p. 1700827. DOI: 10.1002/pssa.201700827.

Jayakrishnan, R. et al. (2005). "Defect analysis of sprayed β-In$_2$S$_3$ thin films using photoluminescence studies". In: *Semiconductor Science and Technology* 20.12, pp. 1162–1167. ISSN: 0268-1242. DOI: 10.1088/0268-1242/20/12/003.

Kambas, K., J. Spyridelis, and M. Balkanski (1981). "Far Infrared and Raman Optical Study of α- and β-In$_2$S$_3$ Compounds". In: *Physica Status Solidi (b)* 105, p. 291. DOI: 10.1002/pssb.2221050132.

Kasperkiewicz, J., J. A. Kovacich, and D. Lichtman (Jan. 1983). "XPS studies of vanadium and vanadium oxides". In: *Journal of Electron Spectroscopy and Related Phenomena* 32.2, pp. 123–132. DOI: 10.1016/0368-2048(83)85090-7.

Kawada, Isao et al. (Nov. 1975). "Crystal structures of V_3S_4 and V_5S_8". In: *Journal of Solid State Chemistry* 15.3, pp. 246–252. DOI: 10.1016/0022-4596(75)90209-1.

Kelly, S. D., D. Hesterberg, and B. Ravel (Oct. 2015). "Analysis of Soils and Minerals Using X-ray Absorption Spectroscopy". In: *Methods of Soil Analysis Part 5-Mineralogical Methods.* American Society of Agronomy and Soil Science Society of America, pp. 387–463. DOI: 10.2136/sssabookser5.5.c14.

King, H. W. and E. A. Payzant (Jan. 2001). "Error Corrections For X-RAY Powder Diffractometry". In: *Canadian Metallurgical Quarterly* 40.3, pp. 385–394. DOI: 10.1179/cmq.2001.40.3.385.

Kittel, C. (2006). *Einführung in die Festkörperphysik.* 14th ed. Oldenbourg Wissenschaftsverlag. ISBN: 978-3-486-57723-5.

Kopitzki, Konrad (1993). *Einführung in die Festkörperphysik.* Stuttgart: Teubner. ISBN: 3-519-23083-6.

Kunzl, V. (1932). "A linear dependence of energy levels on the valency of elements". In: *Collection of Czechoslovak Chemical Communications* 4, pp. 213–224. DOI: 10.1135/cccc19320213.

Lang, D. V. and C. H. Henry (Dec. 1975). "Nonradiative Recombination at Deep Levels in GaAs and GaP by Lattice-Relaxation Multiphonon Emission". In: *Physical Review Letters* 35.22, pp. 1525–1528. DOI: 10.1103/PhysRevLett.35.1525.

Li, G. G., F. Bridges, and C. H. Booth (Sept. 1995). "X-ray-absorption fine-structure standards: A comparison of experiment and theory". In: *Physical Review B* 52.9, pp. 6332–6348. DOI: 10.1103/PhysRevB.52.6332.

Lin, Albert S., Jamie D. Phillips, and Wyatt K. Metzger (Dec. 2009). "Generation and recombination rates at ZnTe:O intermediate band states". In: *Applied Physics Letters* 95.26, p. 261107. DOI: 10.1063/1.3274131.

Lu, Jianting, Aixiang Wei, et al. (Nov. 2018). "Graphene/In_2S_3 van der Waals Heterostructure for Ultrasensitive Photodetection". In: *ACS Photonics* 5.12, pp. 4912–4919. DOI: 10.1021/acsphotonics.8b01070.

Lu, Jianting, Zhaoqiang Zheng, et al. (2019). "Epitaxial growth of large-scale In_2S_3 nanoflakes and the construction of a high performance In_2S_3/Si photodetector". In: *Journal of Materials Chemistry C* 7.39, pp. 12104–12113. ISSN: 2050-7526. DOI: 10.1039/C9TC03795K.

Lucena, Raquel, Irene Aguilera, et al. (2008). "Synthesis and Spectral Properties of Nanocrystalline V-Substituted In_2S_3, a Novel Material for More Efficient Use of Solar Radiation". In: *Chemistry of Materials* 20.16, pp. 5125–5127. ISSN: 0897-4756. DOI: `10.1021/cm801128b`.

Lucena, Raquel, José C. Conesa, et al. (2014). "V-substituted In_2S_3: an intermediate band material with photocatalytic activity in the whole visible light range". In: *Journal of Materials Chemistry A* 2.22, p. 8236. ISSN: 2050-7488. DOI: `10.1039/c4ta00513a`.

Luque, A. et al. (July 2004). "General equivalent circuit for intermediate band devices: Potentials, currents and electroluminescence". In: *Journal of Applied Physics* 96.1, pp. 903–909. DOI: `10.1063/1.1760836`.

Luque, Antonio and Antonio Martí (1997). "Increasing the Efficiency of Ideal Solar Cells by Photon Induced Transitions at Intermediate Levels". In: *Physical Review Letters* 78.26, pp. 5014–5017. ISSN: 0031-9007. DOI: `10.1103/PhysRevLett.78.5014`.

— (2001). "A metallic intermediate band high efficiency solar cell". In: *Progress in Photovoltaics: Research and Applications* 9.2, pp. 73–86. ISSN: 1062-7995. DOI: `10.1002/pip.354`.

Lutz, H. D. (1969). "Gitterschwingungsspektren. III. Mitteilung". In: *Zeitschrift für Naturforschung A* 24.9, pp. 1417–1419. ISSN: 0932-0784. DOI: `10.1515/zna-1969-0929`.

Lutz, H. D., W. Becker, et al. (Feb. 1989). "Raman single crystal studies of spinel type MCr_2S_4(M = Mn, Fe, Co, Zn, Cd), MIn_2S_4(M = Mn, Fe, Co, Ni), $MnCr_{2-2x}In_{2x}S_4$ and Co_{1-x}-$Cd_xCr_2S_4$". In: *Journal of Raman Spectroscopy* 20.2, pp. 99–103. DOI: `10.1002/jrs.1250200207`.

Lutz, H. D. and H. Haeuseler (1971). "Gitterschwingungsspektren. VII. 1. Spinelldefektstruktur. FIR-Spektren und Normalkoordinatenanalyse von β-In_2S_3". In: *Zeitschrift für Naturforschung A* 26.2, pp. 323–325. ISSN: 0932-0784. DOI: `10.1515/zna-1971-0225`.

Malerba, Claudia et al. (Oct. 2011). "Absorption coefficient of bulk and thin film Cu_2O". In: *Solar Energy Materials and Solar Cells* 95.10, pp. 2848–2854. DOI: `10.1016/j.solmat.2011.05.047`.

Mansouri, Ali and Natalia Semagina (July 2018). "Promotion of Niobium Oxide Sulfidation by Copper and Its Effects on Hydrodesulfurization Catalysis". In: *ACS Catalysis* 8.8, pp. 7621–7632. DOI: `10.1021/acscatal.8b01869`.

Marsen, Björn et al. (2012). "Investigation of the Sub-Bandgap Photoresponse in CuGaS$_2$: Fe for Intermediate Band Solar Cells". In: *Progress in Photovoltaics: Research and Applications* 20.6, pp. 625–629. ISSN: 1062-7995. DOI: 10.1002/pip.1197.

Marti, A., L. Cuadra, and A. Luque (2000). "Quantum dot intermediate band solar cell". In: *Conference Record of the Twenty-Eighth IEEE Photovoltaic Specialists Conference - 2000 (Cat. No.00CH37036)*. IEEE, pp. 940–943. DOI: 10.1109/PVSC.2000.916039.

Martí, Antonio et al. (2013). "Six not-so-easy pieces in intermediate band solar cell research". In: *Journal of Photonics for Energy* 3.1, p. 31299. ISSN: 1947-7988. DOI: 10.1117/1.JPE.3.031299.

Mathew, Meril et al. (2006). "Anomalous behavior of silver doped indium sulfide thin films". In: *Journal of Applied Physics* 100.3, p. 033504. ISSN: 0021-8979. DOI: 10.1063/1.2221531.

McCarthy, Robert F., Matthew S. Weimer, Jonathan D. Emery, et al. (2014). "Oxygen-free atomic layer deposition of indium sulfide". In: *ACS Applied Materials & Interfaces* 6.15, pp. 12137–12145. ISSN: 1944-8244. DOI: 10.1021/am501331w.

McCarthy, Robert F., Matthew S. Weimer, Richard T. Haasch, et al. (2016). "V$_x$In$_{(2-x)}$S$_3$ Intermediate Band Absorbers Deposited by Atomic Layer Deposition". In: *Chemistry of Materials* 28.7, pp. 2033–2040. ISSN: 0897-4756. DOI: 10.1021/acs.chemmater.5b04402.

Moretti, Giuliano (Oct. 1998). "Auger parameter and Wagner plot in the characterization of chemical states by X-ray photoelectron spectroscopy: a review". In: *Journal of Electron Spectroscopy and Related Phenomena* 95.2-3, pp. 95–144. DOI: 10.1016/S0368-2048(98)00249-7.

Mott, N. F. (July 1949). "The Basis of the Electron Theory of Metals, with Special Reference to the Transition Metals". In: *Proceedings of the Physical Society. Section A* 62.7, pp. 416–422. DOI: 10.1088/0370-1298/62/7/303.

— (1968). "Metal-Insulator Transition". In: *Reviews of Modern Physics* 40.4, pp. 677–683. ISSN: 0034-6861. DOI: 10.1103/RevModPhys.40.677.

Naghavi, N. et al. (Aug. 2010). "Buffer layers and transparent conducting oxides for chalcopyrite Cu(In,Ga)(S,Se)$_2$ based thin film photovoltaics: present status and current developments". In: *Progress in Photovoltaics: Research and Applications* 18.6, pp. 411–433. DOI: 10.1002/pip.955.

Nishino, Taneo and Yoshihiro Hamakawa (Aug. 1977). "Preparation and Properties of InS Single Crystals". In: *Japanese Journal of Applied Physics* 16.8, pp. 1291–1300. DOI: 10.1143/JJAP.16.1291.

Okada, Y. et al. (2015). "Intermediate band solar cells: Recent progress and future directions". In: *Applied Physics Reviews* 2.2, p. 021302. ISSN: 1931-9401. DOI: 10.1063/1.4916561.

Pai, R. R. et al. (2005). "Defect characterization of spray pyrolised β-In_2S_3 thin film using Thermally Stimulated Current measurements". In: *Journal of Materials Science* 40.3, pp. 741–746. ISSN: 0022-2461. DOI: 10.1007/s10853-005-6315-8.

Palacios, P. et al. (2008). "Transition-Metal-Substituted Indium Thiospinels as Novel Intermediate-Band Materials: Prediction and Understanding of Their Electronic Properties". In: *Physical Review Letters* 101.4. ISSN: 0031-9007. DOI: 10.1103/PhysRevLett.101.046403.

Pedersen, B. and F. Grønvold (Dec. 1959). "The crystal structures of α-V_3S and β-V_3S". In: *Acta Crystallographica* 12.12, pp. 1022–1027. DOI: 10.1107/S0365110X59002869.

Pistor, Paul et al. (2016). "Structure reinvestigation of α-, β- and γ-In_2S_3". In: *Acta Crystallographica Section B Structural Science, Crystal Engineering and Materials* 72.3, pp. 410–415. ISSN: 2052-5206. DOI: 10.1107/S2052520616007058.

Powell, Cedric (1989). "X-ray Photoelectron Spectroscopy Database XPS,Version 4.1, NIST Standard Reference Database 20". en. In: DOI: 10.18434/T4T88K.

Ramiro, I. and A. Martí (Oct. 2020). "Intermediate band solar cells: Present and future". In: *Progress in Photovoltaics: Research and Applications*. DOI: 10.1002/pip.3351.

Ravel, B. and M. Newville (June 2005). "ATHENA, ARTEMIS, HEPHAESTUS: Data analysis for X-ray absorption spectroscopy using IFEFFIT". In: *Journal of Synchrotron Radiation* 12.4, pp. 537–541. DOI: 10.1107/S0909049505012719.

Ravel, Bruce (Mar. 2001). "ATOMS: crystallography for the X-ray absorption spectroscopist". In: *Journal of Synchrotron Radiation* 8.2, pp. 314–316. DOI: 10.1107/S090904950001493X.

Rehr, John J. et al. (2010). "Parameter-free calculations of X-ray spectra with FEFF9". In: *Physical Chemistry Chemical Physics* 12.21, p. 5503. DOI: 10.1039/B926434E.

Rehwald, W. and G. Harbeke (1965). "On the conduction mechanism in single crystal β-indium sulfide In_2S_3". In: *Journal of Physics and Chemistry of Solids* 26.8, pp. 1309–1324. ISSN: 0022-3697. DOI: 10.1016/0022-3697(65)90114-9.

Rühle, Sven (June 2016). "Tabulated values of the Shockley–Queisser limit for single junction solar cells". In: *Solar Energy* 130, pp. 139–147. DOI: `10.1016/j.solener.2016.02.015`.

Schnohr, C. S. (2021). *Private communication.*

Schnohr, Claudia S. and Mark C. Ridgway (Nov. 2014). "Introduction to X-Ray Absorption Spectroscopy". In: *Springer Series in Optical Sciences.* Springer Berlin Heidelberg, pp. 1–26. DOI: `10.1007/978-3-662-44362-0_1`.

Shimoda, Keiji et al. (2019). "Structural characterization of an amorphous VS4 and its lithiation/delithiation behavior studied by solid-state NMR spectroscopy". In: *RSC Advances* 9.41, pp. 23979–23985. DOI: `10.1039/c9ra04338a`.

Shockley, W. and H. J. Queisser (1961). "Detailed balance limit of efficiency of p-n junction solar cells". In: *Journal of Applied Physics* 32.3, p. 510.

Shockley, W. and W. T. Read (Sept. 1952). "Statistics of the Recombinations of Holes and Electrons". In: *Physical Review* 87.5, pp. 835–842. DOI: `10.1103/PhysRev.87.835`.

Simpson, Catherine et al. (2015). "An intermediate band dye-sensitised solar cell using triplet–triplet annihilation". In: *Physical Chemistry Chemical Physics* 17.38, pp. 24826–24830. DOI: `10.1039/C5CP04825G`.

Spasevska, Hristina et al. (2012). "Optimised In_2S_3 Thin Films Deposited by Spray Pyrolysis". In: *International Journal of Photoenergy* 2012.6346, pp. 1–7. DOI: `10.1155/2012/637943`.

Steigmann, G. A., H. H. Sutherland, and J. Goodyear (1965). "The crystal structure of β-In_2S_3". In: *Acta Crystallographica* 19.6, pp. 967–971. ISSN: 0365-110X. DOI: `10.1107/S0365110X65004735`.

Strandberg, Rune and Irene Aguilera (2012). "Evaluation of vanadium substituted In_2S_3 as a material for intermediate band solar cells". In: *Solar Energy Materials and Solar Cells* 98, pp. 88–93. ISSN: 0927-0248. DOI: `10.1016/j.solmat.2011.10.008`.

Strandberg, Rune and Turid Worren Reenaas (2009). "Photofilling of intermediate bands". In: *Journal of Applied Physics* 105.12, p. 124512. ISSN: 0021-8979. DOI: `10.1063/1.3153141`.

Studenyak, Ihor, Mladen Kranjec, and Mykhailo Kurik (Dec. 2014). "Urbach Rule in Solid State Physics". In: *International Journal of Optics and Applications* 4.3, pp. 76–83. DOI: `10.5923/j.optics.20140403.02`.

Tao, Haizheng et al. (2008). "Raman and infrared spectroscopic study of defect spinel $In_{21.333}S_{32}$". In: *Optoelectron. Adv. Mater.* 2.6, pp. 356–359.

Tapia, Cristina et al. (2016). "Synthesis and Characterization of V-doped β-In_2S_3 Thin Films on FTO Substrates". In: *The Journal of Physical Chemistry C*. ISSN: 1932-7447. DOI: 10.1021/acs.jpcc.6b09601.

Tauc, J., R. Grigorovici, and A. Vancu (1966). "Optical Properties and Electronic Structure of Amorphous Germanium". In: *physica status solidi (b)* 15.2, pp. 627–637. DOI: 10.1002/pssb.19660150224.

Urbach, Franz (Dec. 1953). "The Long-Wavelength Edge of Photographic Sensitivity and of the Electronic Absorption of Solids". In: *Physical Review* 92.5, pp. 1324–1324. DOI: 10.1103/PhysRev.92.1324.

Ursaki, V. V. et al. (2002). "Raman scattering study of pressure-induced phase transitions in MIn_2S_4 spinels". In: *Journal of the Physical Society of Japan* 14.27, pp. 6801–6813. ISSN: 0031-9015. DOI: 10.1088/0953-8984/14/27/304.

Valvoda, V. and M. Järvinen (1990). "On The Harris Texture Index". In: *Powder Diffraction* 5.4, pp. 200–203. DOI: 10.1017/S0885715600015797.

Verma, Rajneesh et al. (2010). "Optical, structural, and chemical properties of flash evaporated In_2S_3 buffer layer for $Cu(In,Ga)Se_2$ solar cells". In: *Journal of Applied Physics* 108.7, p. 074904. ISSN: 0021-8979. DOI: 10.1063/1.3490624.

Wägele, Leonard A. et al. (2017). "Structural analysis of co-evaporated In_2S_3 and In_2S_3:V for solar cell absorber applications". In: *physica status solidi c* 14.6, p. 1600204. DOI: https://doi.org/10.1002/pssc.201600204. URL: https://onlinelibrary.wiley.com/doi/abs/10.1002/pssc.201600204.

Wang, Maoxu et al. (2018). "Electrochemically active separators with excellent catalytic ability toward high-performance Li–S batteries". In: *Journal of Materials Chemistry A* 6.25, pp. 11694–11699. DOI: 10.1039/c8ta02757a.

Weimer, Matthew S. et al. (Mar. 2017). "Template-Free Vapor-Phase Growth of Patrónite by Atomic Layer Deposition". In: *Chemistry of Materials* 29.7, pp. 2864–2873. DOI: 10.1021/acs.chemmater.6b05084.

Wong, J. et al. (Nov. 1984). "K-edge absorption spectra of selected vanadium compounds". In: *Physical Review B* 30.10, pp. 5596–5610. DOI: 10.1103/PhysRevB.30.5596.

Wyżga, Paweł et al. (2020). "Crystal structure, phase transition and properties of indium(iii) sulfide". In: *Dalton Transactions* 49.44, pp. 15903–15913. DOI: 10.1039/D0DT03302B.

York, Derek et al. (Mar. 2004). "Unified equations for the slope, intercept, and standard errors of the best straight line". In: *American Journal of Physics* 72.3, pp. 367–375. DOI: 10.1119/1.1632486.

Yu, K. M. et al. (Dec. 2003). "Diluted II-VI Oxide Semiconductors with Multiple Band Gaps". In: *Physical Review Letters* 91.24, p. 246403. DOI: 10.1103/PhysRevLett.91.246403.

Zhao, Zongyan, Juan Yi, and Dacheng Zhou (2013). "Density functional theory study the effects of point defects in β-In$_2$S$_3$". In: *Computational Materials Science* 73, pp. 139–145. ISSN: 0927-0256. DOI: 10.1016/j.commatsci.2013.02.027.

Zhou, Yanli et al. (July 2017). "Vanadium sulfide sub-microspheres: A new near-infrared-driven photocatalyst". In: *Journal of Colloid and Interface Science* 498, pp. 442–448. DOI: 10.1016/j.jcis.2017.03.081.

Appendix A

Appendix

A.1   Validation of doping concentrations

The main method for determining the doping concentration of samples is standardless EDX. This method can result in large errors, so it has to be confirmed that the sample concentrations are correct. This is done with other standardless methods, like RBS or XPS in combination with XRD. The latter allows the comparison of samples with different concentrations and therefore help validate the error estimation.

For small doping concentrations we can expect a linear change of the lattice constants following Vegard's law. It states that the lattice constant of a mixture of materials changes linearly between the lattice constants of the two materials. In our case this would be In_2S_3 and a fictive V_2S_3 with the same crystal structure as the In_2S_3. We can use this expected linear behavior to validate the doping concentration measurements as well as the chosen errors.

Figures A.1 to A.3 display the lattice constants for each of the three transition metals. The linear fits together with the 95% confidence bands are plotted as well. The York method (York et al. 2004) integrated into *OriginPro* was used to fit the data with x- and y-errors. For the undoped samples, the x-error had to be set to $0.1\,at.\%$ to get reasonable results.

For all three datasets reasonable linear behavior is visible and the confidence band includes nearly all samples. The y-error obtained from the fit of the XRD diffractograms is too small to include the variance of different samples at one concentration.
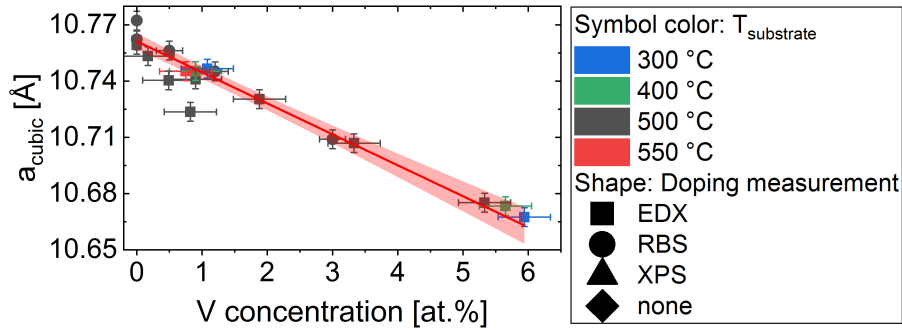
Figure A.1: *Fit and 95 % confidence band of the In_2S_3:V lattice constants versus the doping concentration.*
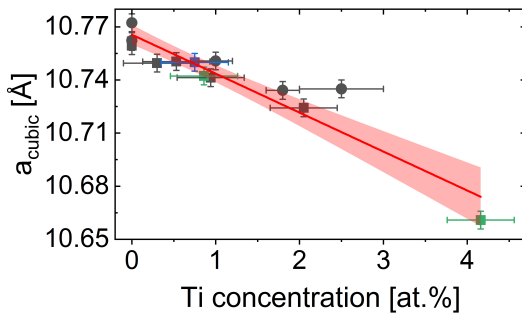
Figure A.2: *Fit and 95 % confidence band of the In_2S_3:Ti lattice constants versus the doping concentration.*
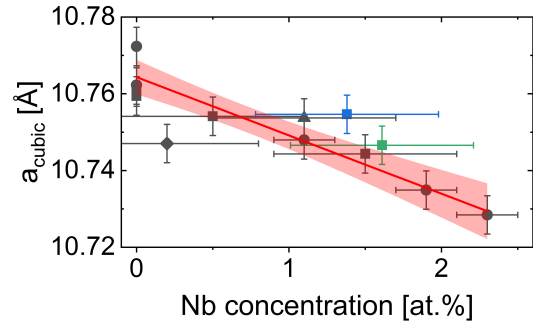
Figure A.3: *Fit and 95 % confidence band of the In_2S_3:Nb lattice constants versus the doping concentration.*

It has to be noted that some samples are grown at different temperatures, which can affect the lattice constants as well.

It would be possible to recalculate the concentrations based on the lattice constants, especially the niobium-doped samples, but, because of the named variance, this is not feasable. RBS, EDX and XPS measurements fall on the same line, which is why large unknown systematic EDX errors can be excluded.

In conclusion the best practice for determining the doping concentrations will be to use the most accurately measured concentration for a sample. This means RBS for thin 60 nm samples and EDX for thick 1 μm samples. The niobium samples were planned to be remeasured with XPS, to avoid the large errors from EDX, but, because of time and experimental constraints, the samples could not be remeasured in time. XPS also includes the problem that it is a very surface sensitive technique which is not very reliable for older samples as is the case here.

A.2 The uncertainty of XRD peak positions

The main systematic error of peak positions in XRD comes from errors in the positioning of the sample within the goniometer. That is the reason why, as stated in section 4.3, a parallel beam setup was used to properly calibrate the sample position.

Despite this extra effort there is a visible shift of the peak position, when looking at the calculated lattice constants for every peak of a well crystallized sample (see figure A.4). Excluding the lower intensity peaks, it becomes visible that the lattice constant rises systematically with the peak angle. For a badly crystallized sample this systematic peak shift is not visible (see figure A.5).
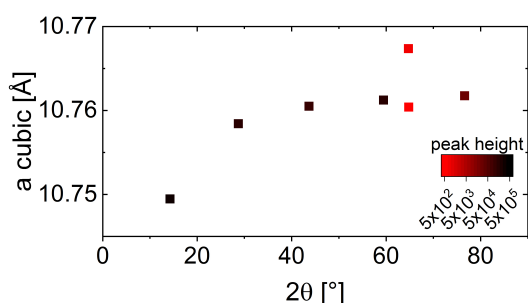
Figure A.4: *Lattice constants calculated from different peaks of a well crystallized pure In_2S_3 sample* **InS-1**. *The color shows the peak height on a logarithmic scale painting low intense peaks red and high intense peaks black.*
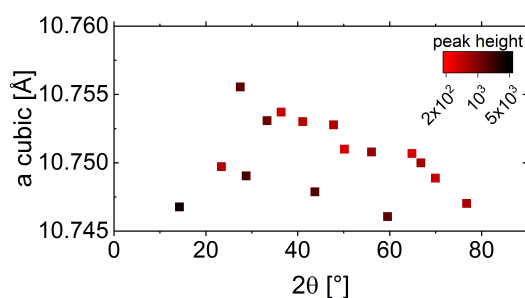
Figure A.5: *Lattice constants calculated from different peaks of a badly crystallized In_2S_3:Nb sample* **InSNb-0.2**. *The color shows the peak height on a logarithmic scale painting low intense peaks red and high intense peaks black.*

To verify the XRD measurements conducted with the *PANalytical Empyrean*, a few samples were remeasured with a *D8 Discover* from *Bruker*, using a monochromated $CuK_{\alpha 1}$ X-ray source. The results are shown in figures A.6 and A.7. There are slight shifts between the measurements, but the overall diffractogram looks very similar (minus the $K_{\alpha 2}$ peaks, bremsstrahlung background and detector misfiring).

Figure A.8 displays the cubic lattice constants obtained from the diffractograms of the *Empyrean* and the *Discover*. The diffractograms were also fitted with different profiles to compare the results. The shift in the lattice constants are even larger when measured with the *Discover*, while the fit profiles give similar results. For the highest angle peak the splitting of the profile slightly increases the lattice constant by about 1×10^{-3} Å. The result from the *Discover* is about 3×10^{-3} Å above the non-split Pear-
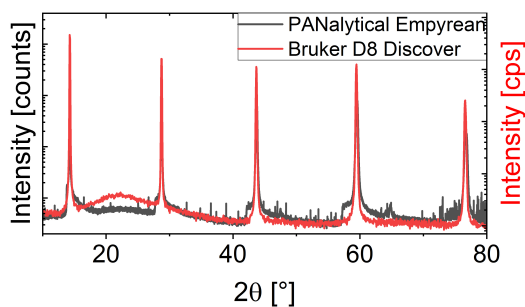
Figure A.6: *Comparison between diffrac-tograms of a pure In$_2$S$_3$ sample* **InS-1** *taken with the* PANalytical Empyrean *and the* Bruker D8 Discover.
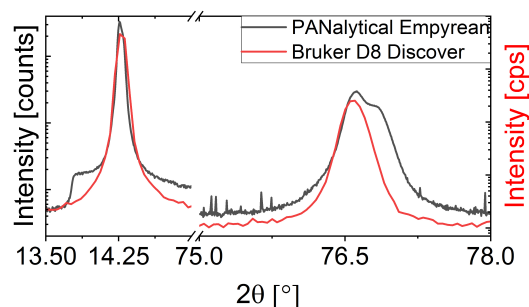
Figure A.7: *Zoom in the comparison between diffractograms of a pure In$_2$S$_3$ sample* **InS-1** *taken with the* PANalytical Empyrean *and the* Bruker D8 Discover.

son fit from the *Empyrean*. As stated in section 4.3, the samples with these high intense peaks are fitted with symmetric Pearson IV profiles for the analysis.
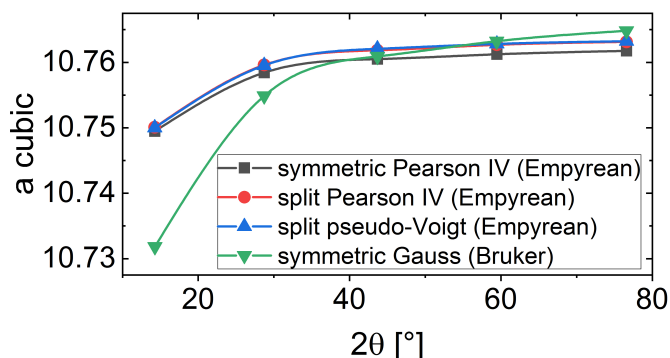
Figure A.8: *Comparison between the cubic lattice constants obtained for a pure In$_2$S$_3$ sample from the* Empyrean *using different fit profiles and the* Discover. *The lines are only guides to the eye.*

There are a few different possible causes for such a peak displacement, which cannot be completely eliminated.

As an example we look at a non-perfect height calibration. Like other systematic errors it can be calculated using the geometry of the XRD goniometer. Figure A.9 sketches the effect of a height error on the geometry of the X-ray path in the Bragg-Brentano setup.

The path difference to the sample Δp is calculated from the height error Δh and
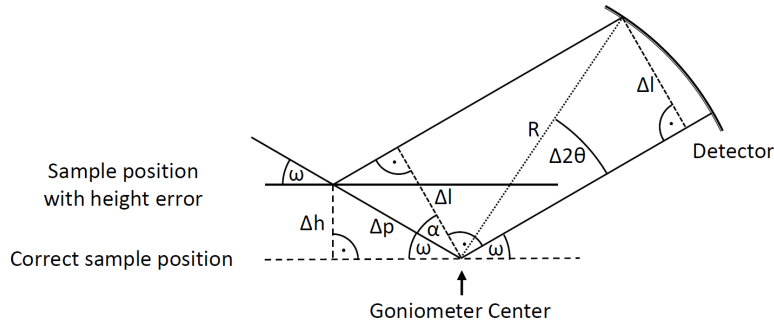
Figure A.9: *Geometry of the X-ray path in the case of a wrong calibration of the sample position in the Goniometer.*

the incident angle ω by

$$\Delta p = \frac{\Delta h}{\sin\left(\omega\right)} \tag{A.1}$$

The shift of the outgoing X-ray path Δl is then given by

$$\Delta l = \Delta p \cos\left(\alpha\right) \tag{A.2}$$

with

$$\alpha = 90° - 2\omega \tag{A.3}$$

Using the known goniometer radius R, the error of the peak position $\Delta 2\theta$ is given by

$$\Delta 2\theta = \arcsin\left(\frac{\Delta l}{R}\right) = \arcsin\left(\frac{\Delta h \cos\left(90° - 2\omega\right)}{R \sin\left(\omega\right)}\right) \approx \frac{2\Delta h \cos\left(\omega\right)}{R} \tag{A.4}$$

with the goniometer radius R. The incident angle can be estimated to be $\omega \approx \theta$, if the height error is small enough.

King et al. (2001) compiled a list of different errors and their effect on the peak position.

One of the problems that cannot be eliminated when working with diverging beams is the flatness of the samples. The parafocusing circle of the beam is curved. As a result, the divergent beam is focused on a too low angle in the goniometer circle. The higher the incident angle, the smaller this error gets (King et al. 2001):

$$\Delta 2\theta = -\frac{\cot\left(\theta\right)\gamma^2}{12} \tag{A.5}$$

with the angular width of the divergence slit γ.

Figure A.10 shows height position and flat sample errors with example values compared to the measured error for sample InS-1. The measured error is obtained by calculating the expected peak positions from the lattice constants of the highest angle peak at 76.6° and comparing them to the actual peak position. This of course ignores any peak shift the 76.6° peak might have, but should be sufficient for this qualitative assessment of the error's source.

The flat sample error very well describes the peak shift seen in the measurements. It does not fit perfectly, but considering the use of the variable divergence slit and a likely combination with other errors, this is a good qualitative explanation of the shift in peak positions.
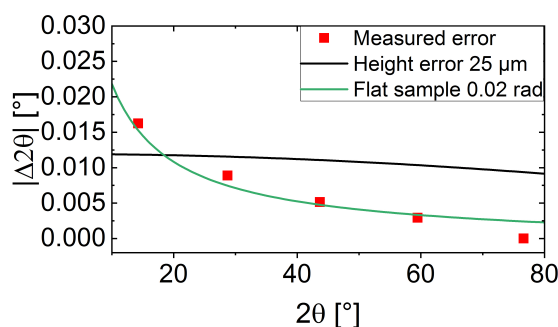
Figure A.10: *Comparison between the measurement's systematic peak position error and calculated examples for a height positioning and source shifting error.*

The usual approach to obtain the lattice constants from a diffractogram is to calculate them from the highest angle peaks, if no more elaborate analysis technique like Rietveld refinement is used. Considering the above error analysis we will do just that, as the highest angle peak should be the most accurate. To additionally verify this choice we can compare the lattice constants to literature values.

Pistor et al. (2016) (PDF#00-067-0787) refined the diffractograms from the high temperature α-In$_2$S$_3$ at various temperatures and found a linear expansion following:

$$a = 10.7480 \, \text{Å} + 1.121 \times T \times 10^{-4} \, \text{Å} \text{K}^{-1} \tag{A.6}$$

At room temperature (300 K) this gives us $a = 10.7816$ Å. They also measured β-In$_2$S$_3$ at room temperature from which cubic equivalent lattice constants can be calculated

(PDF#00-067-0786). Using the $3\,1\,1/1\,0\,9$ reflex from their data results in $a = 10.7832\,\text{Å}$, which is very close to the cubic α-In$_2$S$_3$ at room temperature, considering that the latter was originally measured at $475\,\text{°C}$.

These literature values are above the measured values for a pure In$_2$S$_3$ sample, with the high angle peaks being the closest. The most accurate lattice constant should therefore be the one calculated from the high intensitiy peak with the highest angle, which is the $5\,5\,5$ cubic or $5\,0\,15$ tetragonal peak located at about $76.6°$ for a pure sample. For the calculation of the tetragonal lattice constants a second peak is needed. The second highest high intensity peak is the $4\,4\,4$ cubic or $4\,0\,12$ tetragonal peak located at about $59.5°$. The problem is that this peak combination cannot be used to calculate the tetragonal β-In$_2$S$_3$ lattice constants. As such the $\beta 4\,2\,12$ reflex is used as the second reflex. The often used fitting error, which is in the range of $1 \times 10^{-4}\,\text{Å}$ to $1 \times 10^{-5}\,\text{Å}$ for the high crystallized samples, is too small to correctly describe the accuracy of the lattice constant measurement. When considering all the above, a more reasonable estimated upper error should be in the range of $\Delta a_{cubic} = 5 \times 10^{-3}\,\text{Å}$. This error also better represents the large spread of values obtained for low crystallized samples like in figure A.5.

The lattice constants for the tetragonal lattice are calculated from the same peaks and therefore contain the same errors. As an approximation we can assume that the c/a-ratio does not change much and simply convert the error from cubic to tetragonal by multiplying it with the factors of $\frac{1}{\sqrt{2}}$ and 3, for $a_{cubic} \rightarrow a_{tet}$ and $a_{cubic} \rightarrow c_{tet}$ respectively, to obtain $\Delta a_{tet} = 3.5 \times 10^{-3}\,\text{Å}$, $\Delta c_{tet} = 1.5 \times 10^{-2}\,\text{Å}$. The resulting cubic lattice constants for $1\,\mu\text{m}$ thick samples grown at $500\,\text{°C}$ are $a = 10.762 \pm 0.005\,\text{Å}$ for sample **InS-1** and $a = 10.759 \pm 0.005\,\text{Å}$ for sample **InS-2**. Both samples lie well within the error bars of each other. These values are lower than the literature values, the fact that we have poly-crystalline thin films can be the explanation.

A.3   XRD instrument broadening

For the analysis of the FWHM of the diffraction peaks, it is necessary to know the broadening due to the X-ray diffractometer. This broadening is dependent on the diffraction angle and is usually best eliminated by a deconvolution. An easier approach is the use of a profile-dependent function, the Caglioti formula (Caglioti et al. 1958).

We have only two measurements on $1\,0\,0$ and $1\,1\,1$ Si-wafers available, which is not enough data to fit the Caglioti formula. Instead, we simplify this further and estimate the broadening to be linear and use the two FWHM values to determine the instrument broadening $\beta_{inst}(\theta)$. The fit on the peak of the $1\,1\,1$ wafer resulted in $2\theta = 28.457°$ and $FWHM = 0.0235°$ which is in radians $\beta_{inst}(14.228°) = 4.102 \times 10^{-4}$. The fit on the peak of the $1\,0\,0$ wafer resulted in $2\theta = 69.145°$ and $FWHM = 0.0393°$ which is in radians $\beta_{inst}(34.573°) = 6.859 \times 10^{-4}$. Combining these data results in the approximated instrument broadening function

$$\beta_{inst}(\theta) = 1.355 \times 10^{-5}\theta + 2.173 \times 10^{-4} \tag{A.7}$$

This estimation is enough for the comparison of different samples measured with the same instrument which is the main focus here.

A.4   Preparation of Raman data

Three Raman spectra were measured at different positions for each sample. The spectra of sample **InS-1** are displayed in figure A.11. They all show the same peaks with similar intensities, which confirms the homogeneity in the region of the three measurements. For all samples the three spectra are averaged, and the resulting spectrum normalized to the Rayleigh background at $20\,\text{cm}^{-1}$.
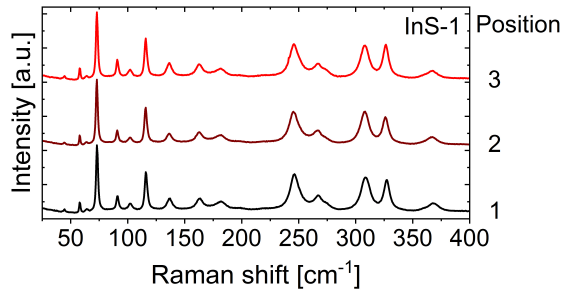
Figure A.11: *Raman spectra of the three measured positions of sample **InS-1**. The spectra are identical and can therefore be averaged to create one spectrum.*

Figure A.12 shows a comparison between the samples **InS-1** and **InS-2**. The shape of the spectrum is identical, only the intensity of the peaks from the second sample is slightly higher.
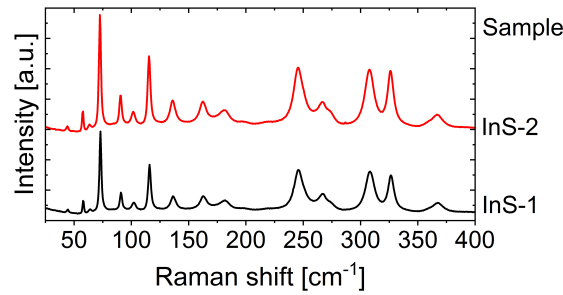
Figure A.12: *Averaged Raman spectra of the two 1000 nm β-In$_2$S$_3$ samples grown at 500 °C. The spectra show the same peaks at the same positions, but with slightly higher intensities for the second sample.*

Because of the large amount of peaks from the β-In$_2$S$_3$ structure, it is difficult to fit all of them. Group theory predicts 36 Raman active modes (Lutz and Haeuseler 1971). The measurements on β-In$_2$S$_3$ reveal 15 clearly distinguishable peaks, with at least 6-8 smaller ones, which are on flanks or the background.

A.5 Absorption coefficient determination

The results of the raw data processing for the Borofloat glass substrate and two different In$_2$S$_3$ layer thicknesses are shown in figures A.13 to A.15. It can be seen that the reflectance R of the samples is stronger impacted by the corrections than the transmittance T. The main reason is the imperfect mirror used for the spectrometer calibration.

As shown in the experiment section, we have different ways to calculate the absorption coefficient. First the Lambert-Beer equation 4.29, second the approximation for internal reflections 4.31, third the complete formula including internal reflections 4.34, and last the transfer matrix method (TMM) using formulas A.8 to A.16. Since TMM is the most complicated method, its usefulness should be considered first. To do this, the resulting values for n and k of the substrate glass and pure In$_2$S$_3$ are looked at in more detail. This is best done by displaying the minimization function A.15, as the residuum of the fit to the experimental data is the best indicator, if something goes awry. Because we have two parameters that are fitted, the following graphs were made by using the one parameter with the lowest residuum and looping over the other parameter. For the residuum of n, k was fix for each wavelength and vice versa.

The 0.7 mm Borofloat glass substrate, which is a three layer air/glass/air setup,
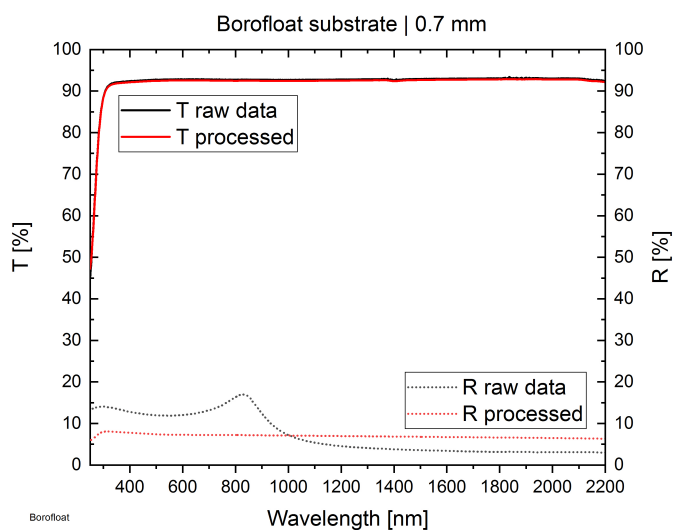
Figure A.13: *Transmittance and reflectance of a* 0.7 mm *Borofloat glass substrates. The black lines show the raw data, the red lines the processed data including corrections and smoothing.*
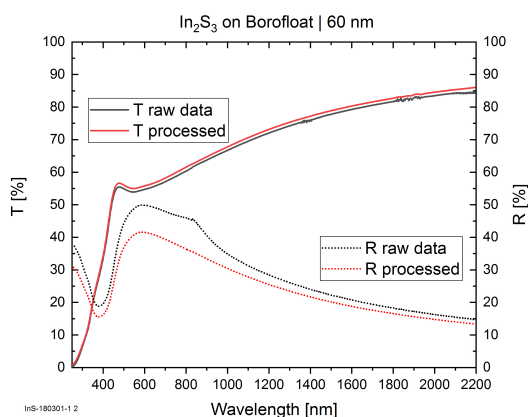
Figure A.14: *Transmittance and reflectance of a* 60 nm *In_2S_3 sample. The black lines show the raw data, the red lines the processed data including corrections and smoothing.*
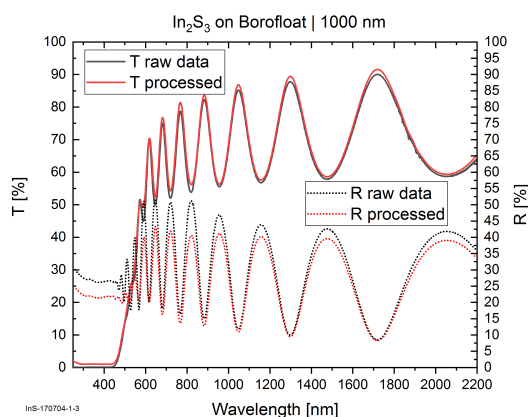
Figure A.15: *Transmittance and reflectance of a* 1000 nm *In_2S_3 sample. The black lines show the raw data, the red lines the processed data including corrections and smoothing.*

works very well with the TMM. Figure A.16 displays the residuum for various refractive indices n. Only one solution is viable, where the residuum is at its minimum and which is therefore chosen by the algorithm. The attenuation coefficient k in figure A.17 does not look as clean, but for every wavelength, there is still only one k with a distinct minimal residuum.
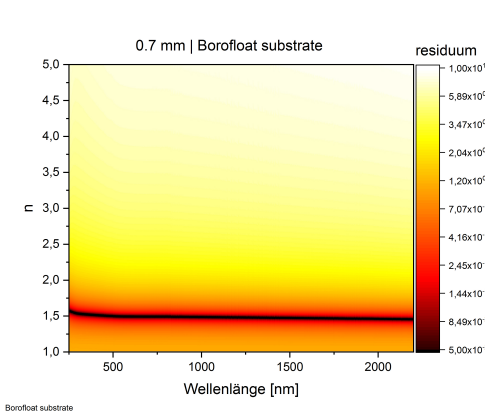
Figure A.16: *Residuum of various n for the fitted k for the Borofloat glass substrate. The algorithm chooses the n with the lowest residuum within the boundary condition. The residuum is shown logarithmically.*
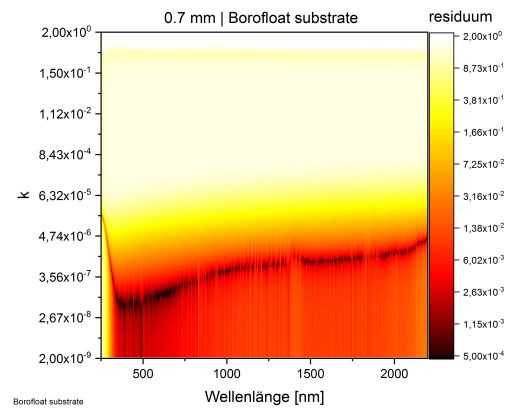
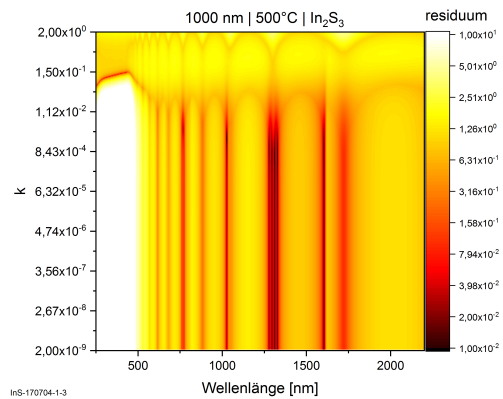**Figure A.17:** *Residuum of various k for the fitted n for the Borofloat glass substrate. The algorithm chooses the k with the lowest residuum within the boundary condition. Both k and the residuum are shown logarithmically.*

The In_2S_3 samples have one more layer resulting in an air/In_2S_3/glass/air stack. The $n(\lambda)$ and $k(\lambda)$ from the glass are fed into this stack, to increase the accuracy of the calculation. The following figures A.18 and A.19 show the calculated residuum for a $60\,nm$ In_2S_3 layer inside the stack. While k still has only one solution for the whole energy range, the solution for n is now disturbed by a second solution around the band gap of the material. This disturbs the correct value of n in this region, making the values for k equally unreliable. This means that for the $60\,nm$ samples TMM can only be used from $2200\,nm$ to about $750\,nm$, excluding the area around and above the band gap energy. It is later shown in figure A.33, that the first interference maximum is in this region.

This problem occurs for all $60\,nm$ In_2S_3 samples, including the doped ones. Figures A.20 to A.23 display the results for $60\,nm$ In_2S_3:V samples with 1.2 and $3\,at.\%$ of V-doping. The second solution around the band gap changes to higher n, but still strongly affects the primary solution.

The next figures A.24 and A.25 display the $1000\,nm$ In_2S_3 samples, which show a multitude of solutions over the whole spectrum. Since interference is a periodic phenomenon, multiple n are solutions for each wavelength. It is therefore impossible for the algorithm to correctly interpret the data. Nonetheless, with the information
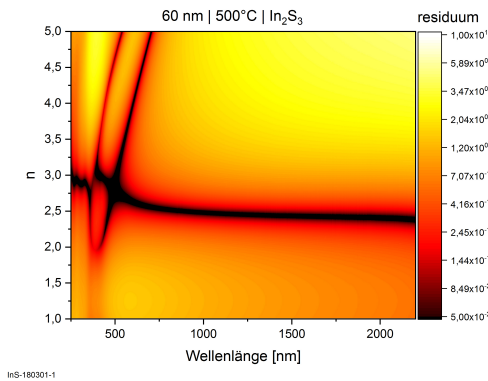
Figure A.18: *Residuum of various n for the fitted k for a $60\,\mathrm{nm}$ In_2S_3 layer. The algorithm chooses the n with the lowest residuum within the boundary condition. The residuum is shown logarithmically.*
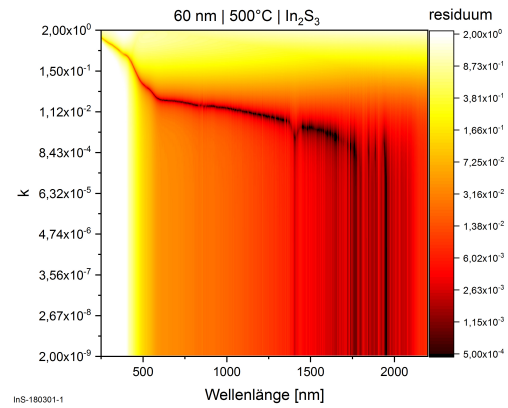
Figure A.19: *Residuum of various k for the fitted n for a $60\,\mathrm{nm}$ In_2S_3 layer. The algorithm chooses the k with the lowest residuum within the boundary condition. Both k and the residuum are shown logarithmically.*
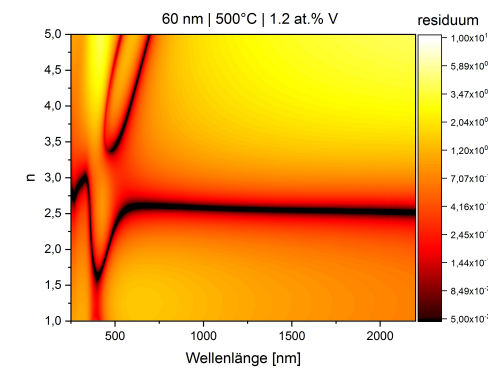
Figure A.20: *Residuum of various n for the fitted k for a $60\,\mathrm{nm}$ In_2S_3:V layer with about $1.2\,\mathrm{at.}\%$ V concentration. The algorithm chooses the n with the lowest residuum within the boundary condition. The residuum is shown logarithmically.*
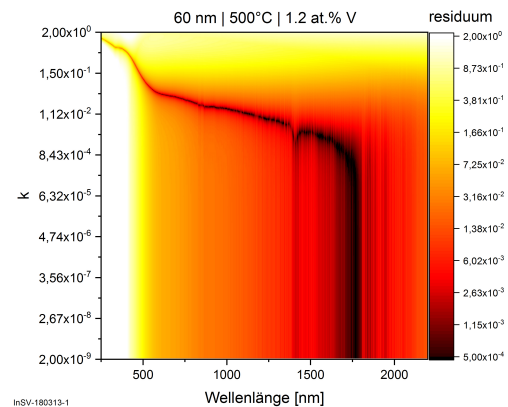
Figure A.21: *Residuum of various k for the fitted n for a $60\,\mathrm{nm}$ In_2S_3:V layer with about $1.2\,\mathrm{at.}\%$ V concentration. The algorithm chooses the k with the lowest residuum within the boundary condition. Both k and the residuum are shown with a logarithmic scale.*

gained from the $60\,\mathrm{nm}$ samples and following the most probable primary solution with the minimum residuum, one can manually determine the n values from 1750 to about $500\,\mathrm{nm}$.

Despite these problems, we can still use n and k to compare them to the literature and the other calculation methods. Figure A.26 shows a comparison between the n
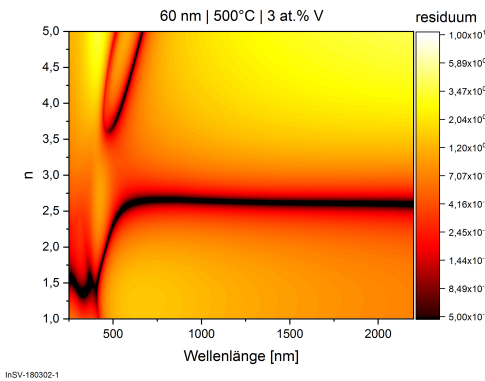
Figure A.22: *Residuum of various n for the fitted k for a $60\,\text{nm}$ In$_2$S$_3$:V layer with about $3\,\text{at.\%}$ V concentration. The algorithm chooses the n with the lowest residuum within the boundary condition. The residuum is shown with a logarithmic scale.*
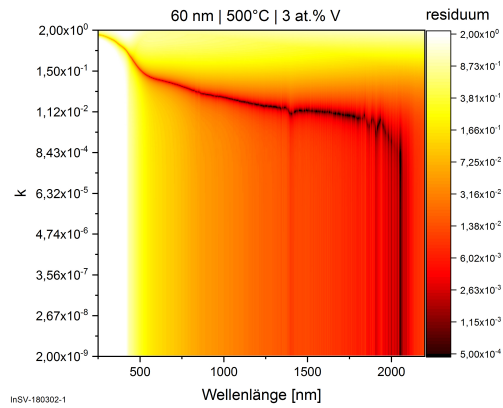
Figure A.23: *Residuum of various k for the fitted n for a $60\,\text{nm}$ In$_2$S$_3$:V layer with about $3\,\text{at.\%}$ V concentration. The algorithm chooses the k with the lowest residuum within the boundary condition. Both k and the residuum are shown with a logarithmic scale.*
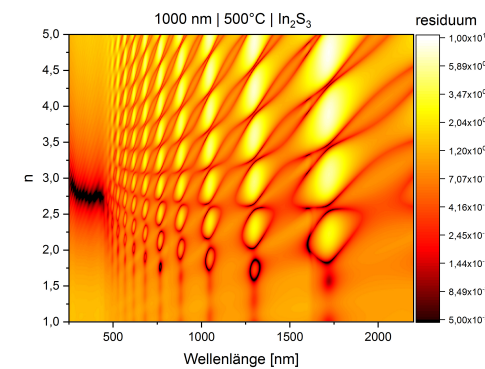
Figure A.24: *Residuum of various n for the fitted k for a $1000\,\text{nm}$ In$_2$S$_3$ layer. The algorithm chooses the n with the lowest residuum, within the boundary condition. The residuum is shown logarithmically.*

Figure A.25: *Residuum of various k for the fitted n for a $1000\,\text{nm}$ In$_2$S$_3$ layer. The algorithm chooses the k with the lowest residuum, within the boundary condition. Both k and the residuum are shown logarithmically.*

values calculated with TMM, one sample additionally with formula 4.38 and two literature values. While the two $1000\,\text{nm}$ samples have the same refractive index, the $60\,\text{nm}$ samples differ by 0.1. This variance in the $60\,\text{nm}$ samples is also observed for doped samples (see figure A.27), which vary in the same range. The error of n is therefore assumed to be in the range of 0.1 to 0.2 and probably comes from the thickness

inhomogeneity of the samples. The position where the thickness was measured can divert from the position of where T and R were measured. The n values calculated from the interference is lower by 0.1 than that from TMM, which is in the assumed error range.

Far below the band gap, n can therefore be said to be in the range of 2.5 ± 0.1, which is in good agreement with literature values for similar thin films (Verma et al. 2010). Due to the large error, a change due to doping is not measurable (see figures A.27 to A.29).
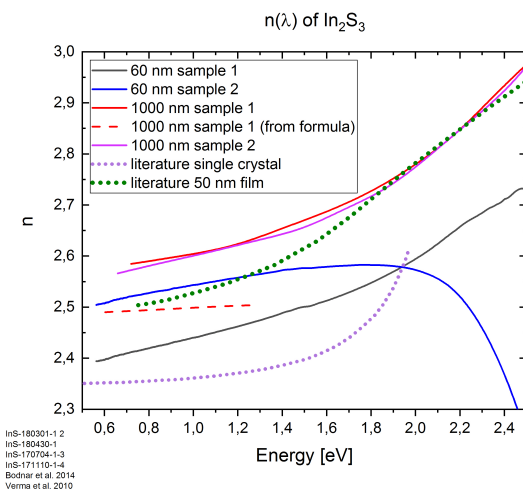
Figure A.26: *Comparison of In_2S_3 refractive indices from TMM, formula 4.38 and two references (Bodnar et al. 2014; Verma et al. 2010).*
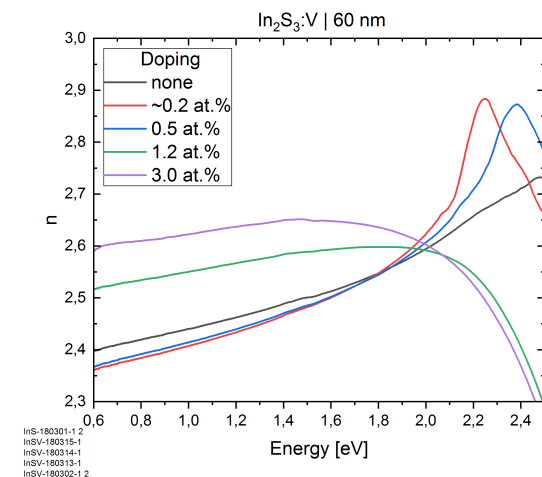
Figure A.27: *With TMM calculated n values for $60\,nm$ In_2S_3:V samples.*

Figures A.30 and A.31 display a comparison between the four tested calculations of the absorption coefficient α for a $60\,nm$ and $1000\,nm$ In_2S_3 layer.

For the $60\,nm$ layer, all methods, except the approximation 4.31 give qualitatively the same result, with the TMM slightly deviating below the band edge, probably due to the better elimination of the substrate glass influence. Above the band gap it deviates more strongly, where the multiple solutions for n are present. In this case the thin-film-formula 4.34 seems to be the best way to calculate α, as it is way easier than TMM and gives the same qualitative result.

For the $1000\,nm$ layer the same can be said, as the TMM results are useless. Additionally, the $1000\,nm$ samples display the detection limit of the measurement setup,
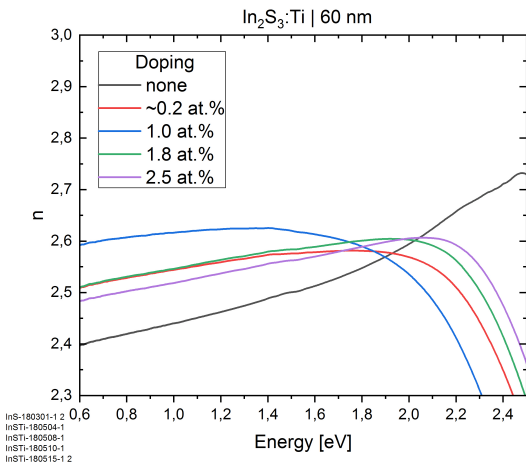
Figure A.28: *With TMM calculated n values for 60 nm In₂S₃:Ti samples.*
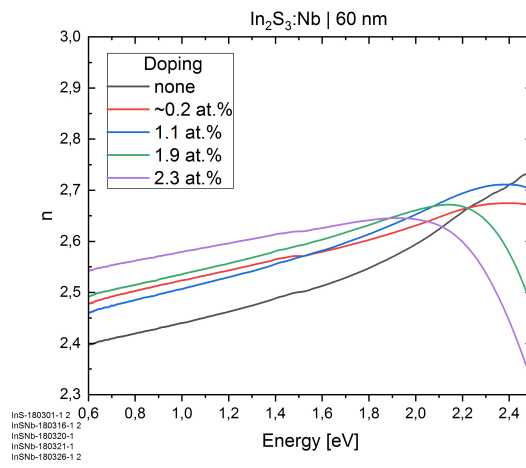
Figure A.29: *With TMM calculated n values for 60 nm In₂S₃:Nb samples.*

where α reaches a plateau. The transmission of the sample was too low for the detector, so the 1000 nm samples are only usable up to about 2.8 eV.
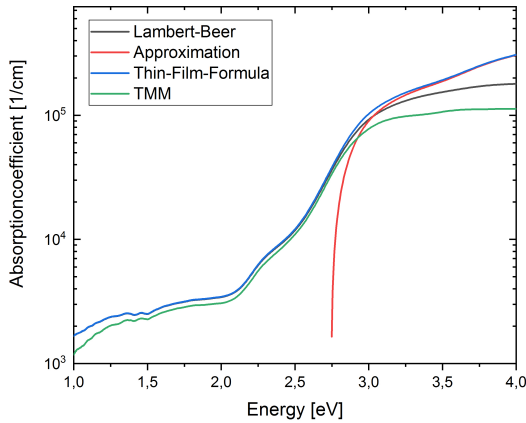
Figure A.30: *Comparison of different methods to calculate the absorption coefficient for a 60 nm In₂S₃ sample.*
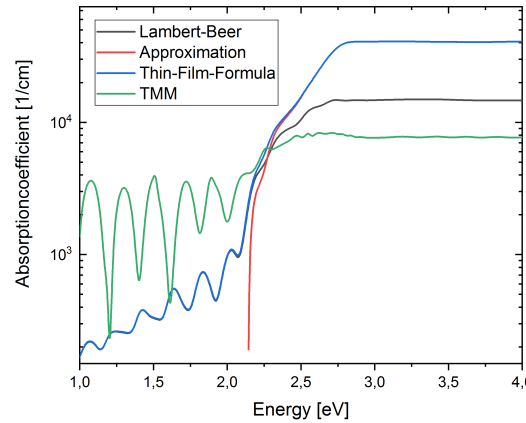
Figure A.31: *Comparison of different methods to calculate the absorption coefficient for a 1000 nm In₂S₃ sample.*

Some samples have been measured twice to check for consistency between measurements (figure A.32). It was aimed to measure the same spot on every T and R measurement, but this was not perfectly possible. There are therefore small changes, which are likely to stem from different amounts of scattering and/or interference. This has to be taken into account during further analysis.
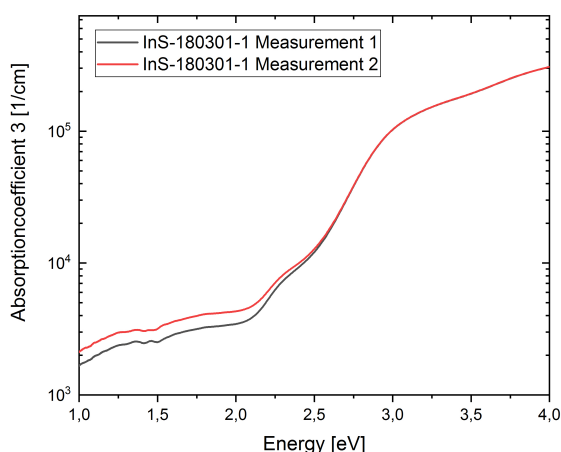
Figure A.32: *Comparison of two measurements of the same sample.*

Figure A.33 displays the calculated reflection interference maxima for two measurements of two $60\,\text{nm}$ samples as dots (using equation 4.37) and compares them with the measured reflectance. The interference calculation was done with various parameters including the measured thickness d and from TMM estimated refractive index n. To explain the interference shift between the two samples the thickness difference must be around $10\,\text{nm}$, or the refractive index difference must be around 0.4. Such a large difference of n is unlikely. But, since the samples are inhomogeneous it is possible that the thickness at the measured position deviates from the XRR measurement, which additionally has an uncertainty of 1 to $3\,\text{nm}$. This interference has to be taken into account, as it is unfortunately directly below the band gap.

A.6   Transfer matrix method

The transfer matrix method is a numerical approach to calculate the absorption coefficient. By fitting the T and R data simultaneously with a model including the thicknesses of all sample layers, the refractive index n and attenuation coefficient k for each wavelength can be derived. The numeric calculation was done with the *tmm*-package for *Python*, which can simulate the light propagation in a planar multilayer film setup using the Fresnel equations and transfer matrix method. The complete derivation of the equations and formalism used can be found in the publication of Byrnes (2016). The important equations are the Fresnel equations, which describe the reflection and
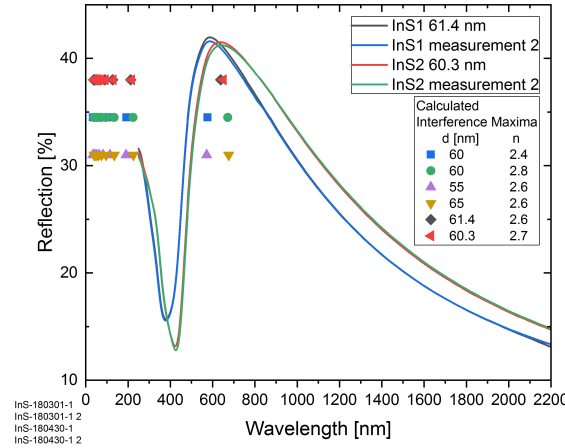
Figure A.33: *Comparison of measured reflectance and calculations of interference maximum positions for various thicknesses and refractive indices. The change of the interference maximum is larger than expected from the measured sample thickness and estimated refractive index.*

transmission coefficients of a planar wave hitting an interface of two materials with different refraction indices:

$$r_s = \frac{n_1 \cos\theta_1 - n_2 \cos\theta_2}{n_1 \cos\theta_1 + n_2 \cos\theta_2} \qquad r_p = \frac{n_2 \cos\theta_1 - n_1 \cos\theta_2}{n_2 \cos\theta_1 + n_1 \cos\theta_2} \tag{A.8}$$

$$t_s = \frac{2n_1 \cos\theta_1}{n_1 \cos\theta_1 + n_2 \cos\theta_2} \qquad t_p = \frac{n_1 \cos\theta_1}{n_2 \cos\theta_1 + n_1 \cos\theta_2} \tag{A.9}$$

with r_s and r_p being the reflection coefficient for s- and p-polarized waves, t_s and t_p the corresponding transmission coefficients, n_1 as the first material's refraction indices and n_2 of the second material, as well as the incident angle θ_1 and exiting angle θ_2.

These equations alone would not help in our case, as we have more than one interface. In fact, we have four material planes, with three interfaces in the case of our sample on top of the substrate glass.

The incident wave has an amplitude of 1, while the amplitude in the opposite direction is per definition the reflection coefficient r. The exiting wave has, also per definition, an amplitude of the transmission coefficient, while there is no incoming wave from that side of the layer stack, that amplitude is therefore 0. In between we have different transmissions and reflections at each interface, but only t and r are measurable. This wave propagation can be formalized with a transition matrix, which describes the transmission and reflection of the whole layer stack. The transition matrix between

layer n and layer $n + 1$ can be expressed by

$$M_n = \begin{pmatrix} \mathrm{e}^{-id_n k_z} & 0 \\ 0 & \mathrm{e}^{id_n k_z} \end{pmatrix} \begin{pmatrix} 1 & r_{n,n+1} \\ r_{n,n+1} & 1 \end{pmatrix} \frac{1}{t_{n,n+1}} \tag{A.10}$$

where the first matrix includes the phase of the wave and the absorption of layer n via the thickness d_n of layer n and the z-component of the incoming wave vector k_z, while $r_{n,n+1}$ and $t_{n,n+1}$ are the reflection and transmission coefficients of the $n/n + 1$-interface. The complete transfer matrix for the whole stack with N layers is then:

$$M = M_0 M_1 M_2 \cdots M_{N-1} \tag{A.11}$$

Now r and t can be calculated for the whole stack from the matrix elements of the complete transfer matrix:

$$\begin{pmatrix} 1 \\ r \end{pmatrix} = M \begin{pmatrix} t \\ 0 \end{pmatrix} = \begin{pmatrix} m_{00} & m_{01} \\ m_{10} & m_{11} \end{pmatrix} \begin{pmatrix} t \\ 0 \end{pmatrix} \tag{A.12}$$

$$\Rightarrow \quad t = \frac{1}{m_{00}} \qquad r = \frac{m_{10}}{m_{00}} \tag{A.13}$$

Transmittance T and reflectance R are then obtained from the coefficients

$$T = \frac{n_2 \cos \theta_2}{n_1 \cos \theta_1} |t|^2 \qquad R = |r|^2 \tag{A.14}$$

In addition, the *tmm*-package is able to differentiate between coherent and incoherent waves in respect to the layer. While the thin sample can be treated with the coherent approach to simulate interference, this is not needed for the relatively thick glass substrate.

To utilize this formalization for the determination of the complex refractive index, a minimization function $f_{min}(n, k)$ has to be defined. In our case it has to determine the difference between the measured R and T and the simulated $T_{calc}(n, k)$ and $R_{calc}(n, k)$ from a certain starting point of n and k.

$$f_{min}(n, k) = \left| \frac{T_{calc}(n, k)}{T} - 1 \right| + \left| \frac{R_{calc}(n, k)}{R} - 1 \right| \tag{A.15}$$

n and k are then varied until the minimization function is below a threshold, or the maximum number of iterations is reached. This is achieved with the *minimization* function from the *scipy.optimize* package using the *L-BFGS-B* method with bounds of $n \pm 0.1$ and $k \pm 0.2$ and the following options:

gtol: 1×10^{-6}, *ftol*: 1×10^{-8}, *eps*: 1×10^{-8}, *maxls*: 20, *maxfun*: 15 000, *maxiter*: 15 000

These parameters yield good results, but shall not be explained in detail (the interested reader is referred to the *SciPy* documentation for more information). Air is approximated with an infinite thickness, $n = 1$ and $k = 0$. The starting parameters for the glass substrate are $n = 1.5$ and $k = 10^{-8}$, for In_2S_3 $n = 2$ and $k = 10^{-3}$ with a starting point at the highest wavelength, where n should be found most reliably. While glass is thick enough to treat light as incoherent, the thickness of the In_2S_3 layers is in the range of the wavelength of the incident light so that the calculations have to be done for coherent light.

After obtaining the refractive index n and attenuation coefficient k the absorption coefficient can be calculated via

$$\alpha = \frac{2k\omega}{c} \tag{A.16}$$

with the speed of light c and the angular frequency of the light ω.

A.7 Lorentz oscillator defect absorption simulation

The difference between absorption spectra used in section 7.2.1 in graph 7.27 to better determine the shape of the defect absorption has to be explained in more detail. One classical way to describe frequency dependent absorption channels is by the use of independent Lorentz oscillators, each representing one electron energy state transition. In this model the electrons are bound to the atoms, behaving as if attached to springs. The resonance frequency describes the energy needed for a transition to another energy state to occur, if the system is diluted and not damped. The dielectric function describing the oscillation of the electrons which we need to calculate the attenuation coefficient is given for one oscillator as

$$\varepsilon(\omega) = 1 + \frac{Ne^2}{\epsilon_0 m_e} \times \frac{1}{\omega_1^2 - \omega^2 - i\beta\omega} \tag{A.17}$$

with N as the lattice atoms per volume, e the electron charge, m_e the electron mass, ϵ_0 the vacuum dielectric constant, ω the angular frequency of the interacting electromagnetic field, β the damping factor of the oscillator and ω_1 the shifted resonance frequency for a high density system calculated from the resonance frequency ω_0 by

$$\omega_1^2 = \omega_0^2 - \frac{1}{3}N\frac{e^2}{\epsilon_0 m_e} \tag{A.18}$$

The whole material can then be described by a sum over all oscillators

$$\varepsilon(\omega) = 1 + \sum_j \frac{N_j e^2}{\epsilon_0 m_e} \times \frac{1}{\omega_{1j}^2 - \omega^2 - \mathrm{i}\beta_j\omega} \tag{A.19}$$

The complex refractive index $\tilde{n}$ can be calculated from the dielectric function via $\tilde{n}^2 = \varepsilon$. Since $\tilde{n} = n + \mathrm{i}k$ it follows that the dielectric function can be split into the real part $\epsilon_1 = n^2 - k^2$ and the imaginary part $\epsilon_2 = 2nk$ with $\varepsilon = \epsilon_1 + \mathrm{i}\epsilon_2$. In combination one gets the attenuation coefficient k in dependence from the dielectric function:

$$k(\omega) = \sqrt{\frac{1}{2}\left(-\epsilon_1(\omega) + \sqrt{\epsilon_1^2(\omega) + \epsilon_2^2(\omega)}\right)} \tag{A.20}$$

(Kopitzki 1993)

For the sake of simplicity we assume to have two oscillators, one for the host material ε_1, one for the defect ε_2 and that they move independently from each other. Table A.1 displays the (mostly arbitrary) parameters used. The resonance frequency ω_0 was calculated from the resonance energy E_0 via the Planck constant h: $\omega_0 = \frac{2\pi E_0}{h}$.

Parameter	Oscillator 1 (ε_1)	Oscillator 2 (ε_2)
N	$4 \times 10^{22}\,\mathrm{m}^{-3}$	$1 \times 10^{21}\,\mathrm{m}^{-3}$
E_0	$2.1\,\mathrm{eV}$	$1.3\,\mathrm{eV}$
β	5×10^{14}	3×10^{14}

Table A.1: *Lorentz oscillator parameters used for the attenuation coefficient simulation.*

The dielectric functions of both oscillators are displayed in figures A.34 and A.35.

Figure A.36 depicts the calculated attenuation coefficients for the two oscillators (using equation A.17 and A.20) and their combination (using equation A.19 and A.20).
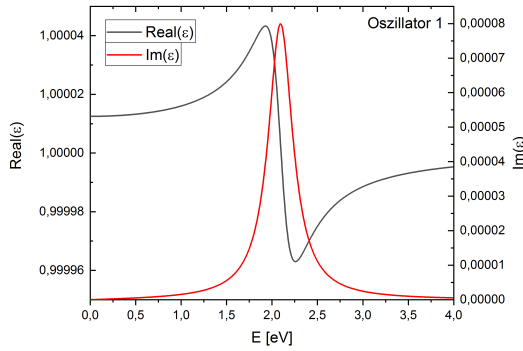
Figure A.34: *Real and imaginary part of the dielectric function of oscillator 1.*
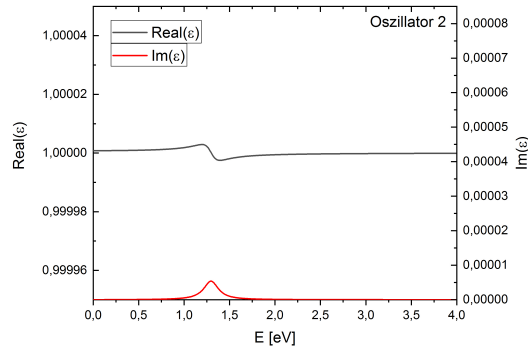
Figure A.35: *Real and imaginary part of the dielectric function of oscillator 2.*
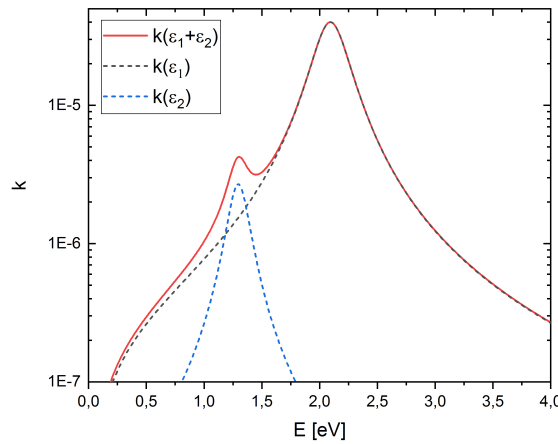
Figure A.36: *Calculated attenuation coefficients for the two oscillators as well as the combination of the two.*

The goal is now to get the shape of the attenuation coefficient of oscillator 2 $k(\varepsilon_2)$ only from oscillator 1 $k(\varepsilon_1)$ and the combination $k(\varepsilon_1 + \varepsilon_2)$. For this we can calculate the difference $k(\varepsilon_1 + \varepsilon_2) - k(\varepsilon_1)$ and the relative difference $\frac{k(\varepsilon_1+\varepsilon_2)-k(\varepsilon_1)}{k(\varepsilon_1)}$. As can be seen in figure A.37, the difference is nearly perfectly aligned with the original k of oscillator 2. The relative difference does have shape changes above and below the resonance energy $E_0 = 1.3\,\text{eV}$, but at around the peak maximum the shape is very similar. The peak position is slightly shifted by about $0.013\,\text{eV}$ or $1\,\%$.

The reverse calculation of the shape of a defect absorption should therefore be possible by using the difference or relative difference between the spectrum of the doped material and the host material. For this to work, the shape of the spectrum of the host material should not change, or be considered during calculation.
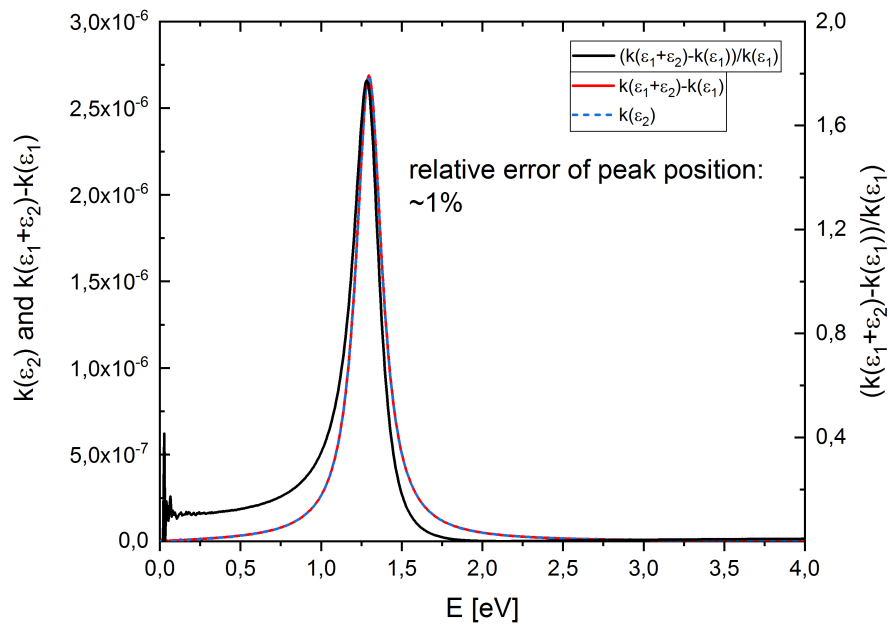
Figure A.37: *Depicted are the original $k(\varepsilon_2)$ of oscillator 2 as a blue dashed line, the difference between the combined $k(\varepsilon_1 + \varepsilon_2)$ and oscillator 1 $k(\varepsilon_1)$ spectrum in red as well as the relative difference between them in black. The relative difference results in a relative peak position error of about 1 %.*
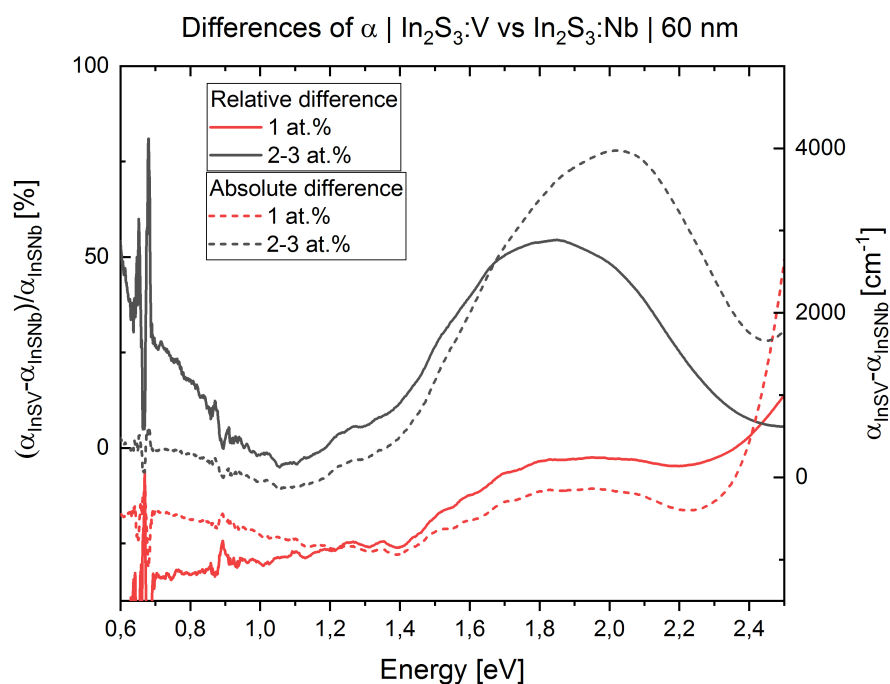
Figure A.38: *Absolute and relative difference between* $60\,\mathrm{nm}$ $1\,\mathrm{at.\%}$ *and* $2\text{-}3\,\mathrm{at.\%}$ *In_2S_3:V and In_2S_3:Nb samples. While the higher doped sample shows an increased absorption below $1\,\mathrm{eV}$ in the relative difference, this is not the case for the lower doped sample. The absolute difference spectrum below $1\,\mathrm{eV}$ looks nearly the same for both doping concentrations, which should not be the case, if it was resulting from the V defect. The rise in absorption below $1\,\mathrm{eV}$ is therefore likely to be an artifact from the measurement.*

Appendix B

Acknowledgments

No experimental scientific work can be achieved alone. Many people have helped me with technical, scientific and motivational guidance. I hope I manage to list everyone who contributed in part to the project and if someone feels I left them out, I probably owe them a beer or two. First of all I want to thank Prof. Dr. Roland Scheer for entrusting me with the topic of intermediate band solar cells and the establishment of this new research field in his group. His open door policy allowed me to develop my research skills independently, while receiving new technological and scientific inspiration from him.

Next I have to thank my supportive wife, who enabled me to work the occasional evening and weekend. She always listened to my problems and gave helpful advice, especially when I was frustrated because the vacuum chamber broke down for the hundredth time. I also thank my curious daughters who are an inspiration as they explore this fascinating world and are very understanding if dad has to got to work once again. Many thanks go to my parents for teaching me a worldview build on logic and kind respect and making it possible for me to follow my dreams.

My colleagues in the photovoltaics group were the foundation I could build my knowledge and experiments on. I especially have to thank Dr. Stefan Hartnauer for paving the way to the custom vacuum chamber and showing me the ropes of physical co-evaporation. I thank Thomas Schneider and Torsten Hölscher for the many many fruitful discussions and just as many laughs. Thanks to Dr. Wolfgang Fränzel and Dr. Heiko Kempa for their general help with organizing and discussions, as well as Ulli

Eidesstattliche Erklärung

Hiermit versichere ich, Leonard Wägele, die vorliegende Arbeit, *Preparation and analysis of transition metal-doped In$_2$S$_3$ for intermediate band solar cell application*, selbstständig und unter ausschließlicher Verwendung der angegebenen Literatur und Hilfsmittel erstellt zu haben. Wörtlich oder inhaltlich entnommene Stellen aus verwendeten Werken sind als solche kenntlich gemacht.

Ich versichere, dass von mir noch keine anderen Promotionsversuche unternommen wurden und die vorliegende Arbeit weder in der gleichen, noch in einer anderen Fassung einer anderen Fakultät vorgelegt worden ist.

Hiermit versichere ich außerdem, dass gegen mich keine Vorstrafen vorliegen und es keine eingeleiteten Ermittlungsverfahren gibt.

Halle (Saale), den 22. Februar 2022

Leonard Wägele